Lifetime Difference in the B_s^0 System from Untagged $B_s^0 \to J/\psi\phi$ Decay at $\sqrt{s} = 1.96$ TeV, at DØ detector

A Thesis

Submitted to the

Tata Institute of fundamental Research, Mumbai

for the degree of Doctor of Philosophy

in Physics

by

Avdhesh Chandra

Department of High Energy Physics

School of Natural Sciences

Tata Institute of fundamental Research

Mumbai

January, 2006

DECLARATION

This dissertation is a presentation of my original work. Wherever contributions of others are involved, every effort is made to indicate this clearly, with due reference to the literature, and acknowledegment of collaborative research and discussions.
This work was done under the guidance of Professor Shashikant Dugad, at the Tata Institute of Fundamental Research, Mumbai.

Signature of the Candidate

(Avdhesh Chandra)

In my capacity as supervisor of the candidate's thesis, I certify that the above statements are true to the best of my knowledge.

Date:

Signature of the Supervisor

(Professor Shashikant Dugad)

To my parents and brother Mahesh.

Acknowledgements

At the outset, I would like to express my deep sense of gratitude to my thesis advisor Professor Shashi Dugad, for his guidance, constant support and encouragement all through my research career at TIFR. Academic interactions with him have always been very thought provoking and beneficial in more ways than one, and I thank him for everything I learnt from him.

I am deeply indebted to my collaborator at DØ Dr. Daria Zieminska, for her help and guidance during data analysis and thesis writing. She always lent a very patient ear during the many useful discussions we had, and came out with very convincing explanations. I would also like to thank Professor Andrzej Zieminski for his help and lively support. My heartfelt thanks to the couple for everything I received from them.

I would like to thank the Chairperson of our group Professor N. K. Mondal for his constant support and encouragement. His interest in our research work ensured smooth running of all our academic activities. His excellent talk on accelerators and our mutual discussions, were deciding factors in my joining this group.

I would like to thank Professor B. S. Acharya for his simple yet elegant explanations to the physics problems. He ensured a very congenial work atmosphere for students. I would also like to thank Professor Sudeshna Banerjee and Professor V. S. Narsimham for their help.

Working with a big collaboration is never possible without help of many people. Sincere thanks to all DØ people for their help during my work and stay at Fermilab. B-physics group

conveners Brendan Casey, Rick Van Kooten, Vivek Jain, Guennadi Borissov, Brad Abbott and other members specially Daniela Bauer, Rick Jesik, Christos Leonidopoulos, Ronald Lipton, Abid Patwa, Ariel Schwartzman, Wendy Taylor, Kin Yip and Jianming Qian are also gratefully acknowledged. My special thanks are to my friends and collaborators Juan Estrada, Suyong Choi, and Michael Weber for their help and friendly nature, and at the same time I would like to acknowledge Dr. Gaston Gutierrez for his help in initiating beam width measurement work.

Back in TIFR, it is a pleasure to thank all my friends and the TIFR staff, specially our group members B. Satyanarayana, P. Nagaraj, Suresh Kalmani and L.V. Reddy. I would also like to thank all members of Department of High Energy Physics and our graduate course teachers. I thank Prolay, Subhendu, Jyothsna, Piyali, Debanjan and Suryanarayan for their help and for making our work place, "HECR Hall" a cheerful one.

I am happy to acknowledge Dr. Amol Dighe, M. Sriram and Anindya Mukherjee for teaching me the theoretical aspect of this analysis, Jyothsna Rani for all her kind help, specially in writing scripts for computational work and to G. K. Padmashree for her critical comments on this thesis.

My friends are invaluable for me, and I cherish every moment of my interaction with them. Dishant and Lalit offered moral support and help, without which I may not have come this far. Amritanshu, Ashish, Vivek, Pratap, Satendra, Rajeev, Mradul and Neeti, also mean a lot to me. Last but not the least I would like to thank my parents and my family for their co-operation, wishes and blessings. Good teaching and words of motivation from my school teachers, Mr. B. S. Yadav and Mr. Pawan Sharama has been instrumental in my reaching this stage, and my sincere thanks to them.

Abstract

In this dissertation, we present a study of the untagged decay of $B_s^0 \to J/\psi\phi$, the final state of which is a superposition of the CP-even and CP-odd states. Within the framework of the standard model (SM), to a good approximation, the two CP eigenstates of the (B_s^0, $\overline{B}_s^0$) system are equivalent to mass eigenstates. The data collected by the DØ detector between June 2002 to August 2004 (an integrated luminosity of approximately 450 pb^{-1}) has been used for the analysis presented in this thesis. From a simultaneous fit to the B_s^0 candidate mass, lifetime, and the angular distribution of the decay products, we obtain the CP-odd fraction in the final state at production time to be 0.16 ± 0.10 (stat) $\pm$ 0.02 (syst). The average lifetime of the (B_s^0, $\overline{B}_s^0$) system is measured to be $1.39^{+0.13}_{-0.16}$ (stat) $^{+0.01}_{-0.02}$ (syst) ps, with the relative width difference between the heavy and light mass eigenstates, $\Delta\Gamma/\overline{\Gamma} \equiv (\Gamma^L - \Gamma^H)/\overline{\Gamma} = 0.24^{+0.28}_{-0.38}$ (stat) $^{+0.03}_{-0.04}$ (syst). With the additional constraint from the world average of the B_s^0 lifetime measurements using semileptonic decays, we find average lifetime of the (B_s^0, $\overline{B}_s^0$) system 1.39 ± 0.06 ps with $\Delta\Gamma/\overline{\Gamma} = 0.25^{+0.14}_{-0.15}$. We have also done B^0 lifetime measurement for its analogous decay mode to $J/\psi K^*$. With this measurement we get B^0 lifetime 1.530 ± 0.043 (stat) $\pm$ 0.023 (syst) ps. Using above results, we get 0.91 ± 0.09 (stat) $\pm$ 0.003 (syst), for the ratio of the B_s^0 and B^0 lifetimes ($\frac{\overline{\tau}(B_s^0)}{\tau(B^0)}$). These measurements are consistent with the predictions of SM within the measurement uncertainty.

Contents

List of Tables

List of Figures

Chapter 1

Introduction

The work presented in this thesis was carried out within the DØ collaboration at the Fermilab Tevatron collider. Our current understanding of elementary particles and their interactions, within the framework of standard model (SM), states that strongly interacting particles are made of fundamental constituents called quarks. Mesons are composed of a quark and anti-quark pair. If one of the quark is a b (or $\overline{b}$) quark the particle is named a B meson. The B_s^0 meson is made of a $\overline{b}$ quark and an s quark (a b quark and an $\overline{s}$ quark in the case of the charge conjugate meson $\overline{B_s^0}$)[1]. The binding between quarks in a B meson is governed by the strong force, while the decay of a B meson is governed by the weak force.

Quantum mechanical treatment of the time evolution of the B_s^0 meson comes out with two physical eigenstates (B_s^L and B_s^H), also known as "Light" and "Heavy" mass eigenstates. To a good approximation, the mass eigenstates are CP eigenstates in the SM. B_s^L corresponds to the CP-even state, while B_s^H corresponds to the CP-odd state. (CP denotes the product of the charge-conjugation and the parity-transformation operations).

The mass eigenstates propagate with distinct lifetimes. The mass and decay width differences between the mass eigenstates, $\Delta M \equiv M_H - M_L$ and $\Delta\Gamma \equiv \Gamma_L - \Gamma_H$, are expected to be sizeable. Their precise measurement is very important to test SM predictions. If the measured magnitude of $\Delta\Gamma$ is greater than predicted, it indicates a deficiency in the calculation of the decay rate. Conversely, a value significantly lower than the SM prediction, would be an unambiguous indication of new physics beyond the SM.

[1]Whenever it is written B_s^0 it includes both B_s^0 and $\overline{B_s^0}$

The decay $B_s^0 \to J/\psi\phi$ exhibits an interesting feature in that it makes it possible to separate the CP-even and CP-odd states. It is an example of a decay of a pseudo-scalar meson(B_s^0) to two vector mesons (J/ψ and ϕ). The vector mesons, in analogy with light waves, have linear polarization states. There are three such states, the parallel and perpendicular orientations of the transverse polarization and the longitudinal polarization, with respect to the decay axis.

The decay $B_s^0 \to J/\psi\phi$ can be described by the time evolution of the linear polarization states of the vector mesons. The angular distribution of the decay products in the process $B_s^0 \to J/\psi(\to \mu^+\mu^-)\phi(\to K^+K^-)$ was first written in the helicity basis, but it can be written in other coordinate systems as well. One of the most convenient bases is the "transversity" basis, in which the cosine of the transversity polar angle (also known as the "transversity" variable), is particularly sensitive to separating the CP states.

We use the information on mass, lifetime, and transversity of the B_s^0 candidate events to measure the lifetime difference between two mass eigenstates and other useful physical parameters of (B_s^0, $\overline{B}_s^0$) system. DØ started collecting data in April 2002 and is expected to operate for at least two more years (upto 2008). For this analysis we have used approximately 450 pb^{-1} of data collected during the period 20^{th} April, 2002 to 22^{nd} August 2004.

A brief overview of the thesis is as follows. The physics issues relevant for this analysis are discussed in chapter 2. A brief introduction and characteristics of the Tevatron and DØ detector are discussed in chapter 3. We discuss and present brief introduction of software and tools relevant for this analysis in chapter 4, while chapter 5, has detail description of analysis of data, starting with dimuon data sample to fit results and ensemble test. Finally, in the last chapter, we summarize the main results and future projection of this analysis.

Chapter 2

Physics Topics

2.1 Standard Model

Understanding of today's particle physics is based on the standard model (SM)[1], which explains almost all physical processes of fundamental particles with good precision. In the SM, fundamental particles are classified in two groups based on their spin: particles of half integer spin (fermions) and particles of integer spin (bosons). Quarks and leptons are fermions, and forces between these elementary particles are mediated by the gauge vector bosons.

Particle Name	Symbol	Charge	Generation
electron	e^-	-1	1
electron neutrino	ν_e	0	
muon	μ^-	-1	2
muon neutrino	ν_μ	0	
tau	τ^-	-1	3
tau neutrino	ν_τ	0	

Table 2.1: List of fundamental leptons.

Each fermion is characterized by specific $flavor$. There are three families (generations), of doublets of quarks and leptons. Each quark doublet has one up-type quark (charge $+\frac{2}{3}$e) and one down-type quark (charge -$\frac{1}{3}$e), each with an internal degree of freedom called *color*.

[1]This introduction to the Standard Model is based on [1] [2]

Particle Name	Symbol	Charge	Generation
up	u	2/3	1
down	d	$-1/3$	
charm	c	2/3	2
strange	s	$-1/3$	
top	t	2/3	3
bottom	b	$-1/3$	

Table 2.2: List of fundamental quarks.

There are three possible colors. Each lepton doublet has one charged lepton and a charge less neutrino. Tables 2.1 and 2.2 list three generations of quarks and leptons.

In the SM, there are four fundamental forces namely, gravitational force, weak force, electromagnetic force, and strong force (in an increasing order of strength), believed to be mediated by different type of gauge vector bosons. Properties of these forces are listed in Table 2.3. All these forces are believed to be derived from the same origin, i.e. at high energy scale all forces behave in same way. A successful theory of electromagnetic and weak force unification exists to which strong force is believed to be unified at the so called grand unification energy scale ($\sim 10^{15}$ GeV). However, a unified theory for all four forces has not yet been achieved. Since the gravitational force is of negligible strength compared to the other forces, its effect on high energy experiments can be neglected.

Force	Carrier	Range (cm)	Strength	Mass (GeV)	Charge	Spin
Gravity	graviton	infinite	10^{-40}	0	0	2
Weak	W^+	10^{-16}	10^{-6}	80.4	1	1
	W^-			80.4	-1	1
	Z^o			91.2	0	1
EM	photon	infinite	10^{-2}	0	0	1
Strong	gluons	10^{-13}	1	0	0	1

Table 2.3: Properties of the four fundamental forces.

Electromagnetic interactions are described in the SM by Quantum Electrodynamics

(QED) [3]. According to QED, charged particles interact via photon exchange. The strength of the interaction is given by the "fine structure constant" $\alpha = \frac{e^2}{4\pi\epsilon_0\hbar c} \sim \frac{1}{137}$. QED is used to compute electromagnetic cross-sections in quantum field theory. There are also self energy corrections involving photon and e^+e- pair loops, leading to infinite mass and charge. Using the principle of renormalization, we redefine mass and charge to their physics values, by canceling infinities. The QED theory has been established succesfully due to the excellent agreement of its predictions with observations [4].

Quantum chromo dynamics (QCD [5]) is the field theory of strong interaction between quarks and gluons, where gluons are carriers of strong force and are a set of eight massless vector particles characterized by a combination of "color charges". The "color charge" in the strong interaction is an equivalent of "electric charge" in the electromagnetic interaction. In contrast to the electromagnetic interaction where photon does not have an electric charge, gluons carry the color anti-color charge and obey the SU(3) symmetry. Also since gluons have color charges they can interact with each other, and as a consequence the strength of the strong interaction (α_s), decreases with energy and increases with distance. At short distance, like inside the hadron, α_s is small and quarks appear to be free. But if one tries to pull any quark from hadron by pumping energy, α_s increases, and finally quark anti-quark pair is produced that combine to create a meson. This process continues until all available energy is not absorbed. That is why in high energy experiments we do not see free quarks but "jets" of hadrons.

All quarks and leptons also experience the weak force, while neutrinos experience only the weak force. The typical lifetime for decay of particles involving weak interactions is comparatively large, of the order of 10^{-8} second, while for electromagnetic and strong forces it is of order of 10^{-16} and 10^{-23} seconds respectively. According to the Fermi theory of weak interactions, it is a point-like interaction of strength G_F ($1.17 \times 10^{-5} GeV^{-2}$), also known as Fermi coupling constant. In the SM, weak interaction is due to $W^{\pm}/Z$ bosons, but due to the large mass of $W^{\pm}/Z$, the weak interaction appears to be point interaction.

The gauge theory that unites the weak and electromagnetic interactions, is known as

electroweak theory purposed by Glashow, Weinberg, and Salam in late 1960s [6]. The gauge symmetry group $SU(2)_L \times U(1)_Y$ requires $(2^2-1)+(1^2)=4$ massless gauge vector bosons. $SU(2)_L$ contains left-handed weak iso-spin doublets (like e_L^- and ν_e) while $U(1)_Y$ contains right handed iso-spin singlets(like e_R^-). To describe the weak interaction phenomenology at low energies, it is required that the vector bosons mediating this force acquire a non-zero mass. This is accomplished through the process of spontaneous symmetry breaking [7], which is implemented via the so-called Higgs Mechanism [8]. The Higgs Mechanism requires the introduction of complex scalar fields. By allowing the scalar field to acquire a non-zero vacuum expectation value, 3 of the 4 gauge vector bosons acquire a mass and these are identified with the $W^{\pm}$ (mediating charged-current weak interactions), and the Z° (mediating the neutral-current interactions). The remaining massless gauge vector boson is identified with the photon, γ (mediating the electromagnetic interactions). There remains one neutral scalar field which is called the Higgs field, associated with the Higgs boson. Higgs bosons are yet to be observed experimentally.

2.2 CP Violation and Unitary CKM Matrix

In the SM, the weak charged current between the up-type-quarks (u, c and t) and down-type-quarks (d, s and b) takes the following form:

$$J_{\mu}^{\mathrm{CC}} = (\ \overline{u},\ \ \overline{c},\ \ \overline{t}\ ) V_{\mathrm{CKM}} \begin{pmatrix} d \\ s \\ b \end{pmatrix} \tag{2.1}$$

where the coupling constant and the space-time structure operator $\gamma_{\mu}(1+\gamma_5)$ have been omitted. V_{CKM} is a 3×3 unitary matrix known as Cabibbo-Kobayashi-Maskawa (CKM) mixing matrix in flavor space. The CKM matrix [2] rotates the electroweak eigenstates(d', s', b')

[2]This overview of CKM matrix is based on [9]

into the mass eigenstates(d, s, b).

$$\begin{pmatrix} d' \\ s' \\ b' \end{pmatrix} = \begin{pmatrix} V_{ud} & V_{us} & V_{ub} \\ V_{cd} & V_{cs} & V_{cb} \\ V_{td} & V_{ts} & V_{tb} \end{pmatrix} \cdot \begin{pmatrix} d \\ s \\ b \end{pmatrix} \equiv V_{\mathrm{CKM}} \cdot \begin{pmatrix} d \\ s \\ b \end{pmatrix} \tag{2.2}$$

The elements in V_{CKM} matrix are complex numbers and represents the coupling strength between up-type quarks (charge $\frac{2}{3}$e) with down-type quarks (charge $-\frac{1}{3}$e). Matrix elements represent the interaction amplitude of decay vertex, in the decay of down-type quarks to up-type quarks, for example, the vertex at which a b quark decays to a W^- boson and u(or c) quark is proportional to V_{ub} (or V_{cb}). The complex conjugate of matrix elements represents interaction amplitude of up-type quarks decay vertex to down-type quarks; for example the vertex at which a t quark decays to a W^+ boson and b (or s) quark is proportional to V_{tb}^* (or V_{ts}^*). As CKM matrix elements are complex numbers, CKM matrix (in its general form) contains 9 complex numbers, and hence 18 free parameters. Because CKM matrix is a unitary matrix by construction, this constraint of nine equations reduces the free parameters to nine (three angles and six phases). One phase can be absorbed into each quark field. An overall common phase is unobservable, and this reduces the total number of free parameters further from nine to four. Of these four parameters, three are rotation angles called quark mixing angles. The remaining one is a complex phase and causes CP violation in the SM.

Interactions between quarks from the same family are strongly favored, while interaction between quarks of different family are suppressed. CKM matrix elements along the diagonal of the matrix are therefore almost equal to one, while off diagonal elements of the matrix are small, and elements further away from the diagonal are smallest. A convenient representation of the CKM matrix in which above stated structure is clearly visible is due to Wolfenstein, also known as Wolfenstein parametrization [10]. In this representation, the matrix is expanded in powers of four independent parameters known as λ, A, ρ, and η.

From experiments, we know that $\lambda \approx 0.22$, $A \approx 0.8$, and $\sqrt{\rho^2+\eta^2} \approx 0.4$. The CKM matrix can be written in higher powers of λ as,

$$V = \begin{pmatrix} 1-\frac{1}{2}\lambda^2 & \lambda & A\lambda^3(\rho - i\eta) \\ -\lambda & 1-\frac{1}{2}\lambda^2 & A\lambda^2 \\ A\lambda^3(1-\rho-i\eta) & -A\lambda^2 & 1 \end{pmatrix} + \mathcal{O}(\lambda^4)\,. \tag{2.3}$$

The parameters ρ and η occur only in terms with λ^3 and higher power of λ. From Eq. 2.3, it is clear that the non-zero value of η is actually a source of CP violation.

The unitary condition for CKM matrix ($V_{\rm CKM} \cdot V^{\dagger}_{\rm CKM} = \hat{1} = V^{\dagger}_{\rm CKM} \cdot V_{\rm CKM}$) provides interesting avenues for testing the CKM picture of CP violation. Unitary condition results in a total of 12 equations, consisting of 6 normalization and 6 orthogonality relations. The orthogonal relations can be represented as 6 triangles in the complex plane, all having the same area [11]. However, all three sides are of comparable magnitude $\mathcal{O}(\lambda^3)$ only for two of them, and the remaining ones are squeezed triangles relative to the others(for example, triangle related to B^0_s meson has sides λ^2, λ^2 and $A\lambda^4$). One of the non-squeezed triangle equation is given below:

$$V_{ud}\,V^*_{ub} + V_{cd}\,V^*_{cb} + V_{td}\,V^*_{tb} \;=\; 0 \tag{2.4}$$

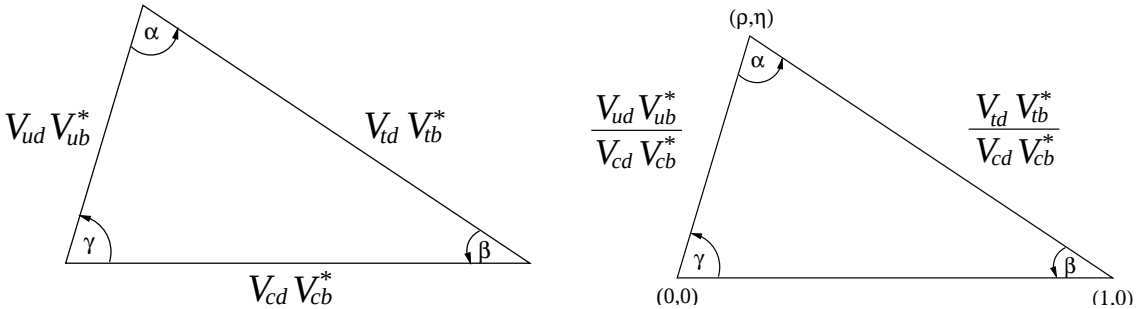

Figure 2.1: The unitarity triangle. The version on the left directly expresses Eq. (2.4). The rescaled version shows the same triangle with unit length on real axis in complex (ρ, η) plane.

The aim of today's experimental high energy physics is to verify the SM picture of CP violation, by "over constraining" one or more triangles with all its sides and angles measured, and then search for new physics beyond the SM. For measuring all sides and angles of a triangle it is easier to deal with a normalized unitary triangle i.e. dividing Eq. 2.4 by $V_{cd}V_{cb}^*$ so that one arm of the unitary triangle becomes unity, and lies on real axis in the complex (ρ, η) plane. If coordinates of the three points of the normalized unitary triangle are (0,0) (1,0) and apex (ρ, η) in the complex plane[3], as shown in Fig. 2.1, where ρ and η are defined as: $\rho + i\eta \equiv -\frac{V_{ud}V_{ub}^*}{V_{cd}V_{cb}^*}$, then the three interior angles of this triangle, can be expressed as

$$\alpha = \tan^{-1}\left(\frac{\eta}{\eta^2 + \rho(\rho-1)}\right), \quad \beta = \tan^{-1}\left(\frac{\eta}{1-\rho}\right), \quad \gamma = \tan^{-1}\left(\frac{\eta}{\rho}\right), \tag{2.5}$$

Since in complex plane, ρ, η and $1-\rho$, could easily be of comparable size, the angles given in Eq. 2.5 and the corresponding CP asymmetries, could be large. Measurement of these angles, for all possible unitary triangles is important to test the predictions of CP violation related with b quark decay in the SM framework.

2.3 B_s^0 Lifetime

A B meson is made of a heavy b (or $\overline{b}$) quark bound to a light quark by the strong interaction. Its decay proceeds through the weak interaction. Because the b quark is massive as compared to other quarks, the lifetime of a B meson can be described by "free" b quark decay and neglecting the presence of other quark. This model is known as the "Spectator Model" of B mesons lifetime. In the spectator model, the partner of b quark in a B meson plays only the role of spectator quark, and is assumed not to affect the B meson decay.

In the SM, a free b quark decays in a way analogous to a muon decay. The decay width amplitude of muon decay to electron and associated neutrino is given by $\Gamma(\mu \to e\nu_e\overline{\nu_\mu}) =$

[3] ρ and η used here are different from what is given in Eq. 2.3

$\frac{G_F^2 m_\mu^5}{192\pi^3}$. A free b quark decays to a c (or u) quark with a virtual W boson, as shown in figure 2.2. The b quark decay vertex associated with W boson corresponds to CKM matrix elements. Decay of $b \to uW$ is suppressed compared to $b \to cW$ as matrix element V_{ub} (associated with $b \to uW$) is diagonally away from V_{cb} (associated with $b \to cW$). Virtual W boson associated with $b \to cW$ (or $b \to uW$) can decay to lighter quark pairs $(\overline{u}, d)$ or $(\overline{c}, s)$ or lepton pair $(l, \overline{\nu_l})$, because of large phase space available in b quark decay.

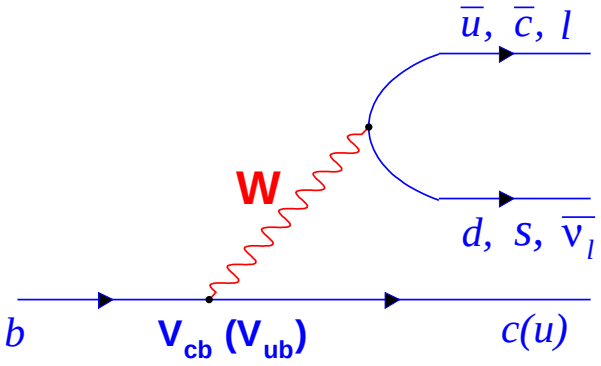

Figure 2.2: b quark decay.

In the spectator model, decay width amplitude of $b \to cW$ is given by

$$\Gamma(b \to cW^-) = \frac{G_F^2 m_b^5}{192\pi^3} \; f_{cb} \; |V_{cb}|^2 \quad \sum \left(3|V_{q_i q_j}|^2 . f_{q_i q_j} + f_{l\nu_l}\right) \tag{2.6}$$

where summation is over all the possible final state in the W decay. The factor f_{cb}, $f_{q_i q_j}$ and $f_{l\nu_l}$ are phase space correction factors. Multiplication factor of 3 is because of the color freedom in decays to quark pairs. Using Eq. 2.6, determination of the CKM matrix element V_{cb}, was done by measurement of the average b lifetime. The typical B hadron lifetime is of the order of pico seconds. As a matter of fact this was the first evidence for the small coupling between the b quark to 2^{nd} generation quarks. This is the simplest way of calculating matrix elements using spectator model. However to get precise values of matrix elements, QCD effects have to be taken into account while calculating the B hadron lifetimes. According to Spectator Model, all B hadrons should have same lifetime, but

experimentally we see that they are significantly different as given in table 2.4 (from Heavy Flavor Averaging Group (HFAG) [12]). The lifetimes of B hadrons are found to follow the following pattern:
$\tau(B_c^+) < \tau(\Lambda_b^0) < \tau(B_s^0) < \tau(B_d^0) < \tau(B_u^+)$. This clearly shows that Spectator Model calculations are not enough to explain the behavior of B hadrons. It is necessary to include other QCD effects in Spectator Model to explain B hadron's behavior. The theory which includes QCD effects and describes the decay of hadrons containing a heavy quark, is known as Heavy Quark Effective Theory(HQET) [13] [14].

B hadron	Average lifetime (in pico second)
B^+	1.653 ± 0.014
B^0	1.534 ± 0.013
B_s^0 ($\rightarrow$ flavor specific)	1.442 ± 0.066
B_s^0 ($\rightarrow J/\psi\phi$)	1.404 ± 0.066
B_s^0 ($1/\overline{\Gamma}$)	$1.405^{+0.043}_{-0.047}$
B_c^+	0.45 ± 0.12
λ_b^0	1.232 ± 0.072

Table 2.4: Summary of B hadrons lifetimes, as given by HFAG [12].

In the HQET calculations, many corrections to the spectator model are done to take into account the non-perturbative effects. This theory is valid in the limit of heavy quark mass $m_Q >> \Lambda_{QCD} \sim 200MeV$ i.e. mass of the heavy quark is much greater than the momentum exchange between strongly bound quarks inside a hadron. Under HQET, heavy quark mass is irrelevant, heavy quark is characterized by its flavor and color SU(3) quantum numbers. The effective Lagrangian is written in terms of $1/m_Q$, and corrections are applied to each term. To calculate decay rate matrix elements, the operator product expansion (OPE) has been used by expanding the tensor in inverse power of heavy quark mass. Using OPE if we compute the rate for inclusive semileptonic B decay, by neglecting higher order terms in $1/m_b$, we obtain the same result of decay rate, as that for free b quark decay! The deviation from free b quark decay first appear in the $1/m_b^3$ term for B mesons decays, and $1/m_b^2$ for Λ_b^0 decay.

Ratios	HQET prediction	HFAG value
$\tau(\Lambda_b^0)/\tau(B_d^0)$	0.90 ± 0.05	0.796 ± 0.054
$\tau(B_u^+)/\tau(B_d^0)$	1.053 ± 0.023	1.074 ± 0.014
$\tau(B_s^0)/\tau(B_d^0)$	1.00 ± 0.01	0.948 ± 0.038
$\Delta\Gamma_d/\Gamma_d$	0.0030 ± 0.0012	-0.008 ± 0.037
$\Delta\Gamma_s/\Gamma_s$	0.12 ± 0.05	< 0.29 (95% C.L.)

Table 2.5: Summary of theoretical predictions of the B hadron lifetime ratios from HQET and their experimental values.

HQET predictions for the lifetime ratios and relative width difference are given in table 2.5 with experimental values. Except for Λ_b^0, all other values are in good agreement with the SM. In this thesis we have measured average lifetime for B_d^0 and B_s^0 mesons as well as relative lifetime difference $(\Delta\Gamma/\overline{\Gamma})$ for $(B_s^0, \overline{B}_s^0)$ system, and finally average lifetime ratio between B_d^0 and B_s^0 mesons $(\frac{\overline{\tau}(B_s^0)}{\tau(B^0)})$. These are important tests for HQET predictions and for any possible new physics beyond the SM.

2.4 B_s^0 Mixing

Because of the non-diagonality of the CKM matrix, the neutral B_q meson[4] exhibits an interesting phenomenon known as neutral B meson mixing. In experiments, neutral B mesons are produced with definite flavour at the time of collision. Consider an arbitrary neutral b flavoured meson state[5] at time t:
$|f(t)\rangle = f_1(t)|B_q\rangle + f_2(t)|\overline{B_q}\rangle$. As in the neutral kaon system, particle-antiparticle mixing also exist in the neutral $(B_s^0, \overline{B}_s^0)$ systems, and initial flavour state evolves into a time-dependent superposition of the two flavour eigenstates, as shown in Fig. 2.3.

Time evolution of state $|f(t)\rangle$, will be governed by the time dependent Schrödinger

[4] q stands for s or d quark, quantum mechanically both B_s and B_d follow same pattern
[5] For mixing discussion, we omitted superscript 0, i.e. $B_q \equiv B_q^0$ and $\overline{B_q} \equiv \overline{B_q^0}$

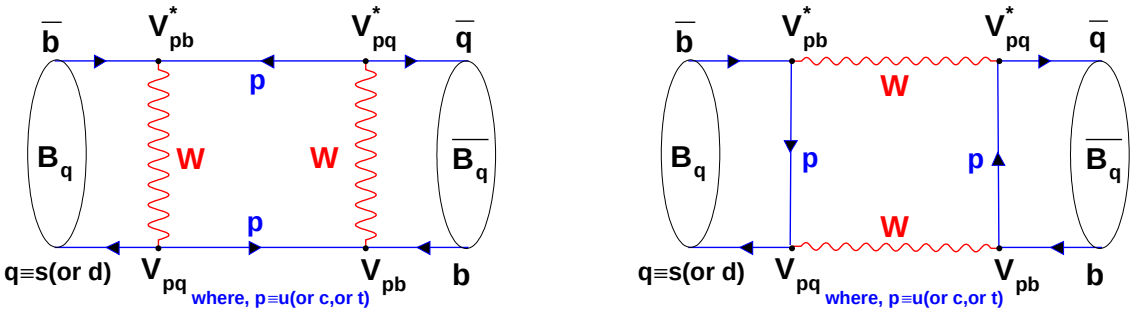

Figure 2.3: General box diagram showing lowest order B_q–$\overline{B}_q$ mixing.

equation, as a 2×2 Hamiltonian matrix in the $B_q - \overline{B_q}$ basis:

$$i \frac{\partial}{\partial t} |f(t)\rangle = \mathbf{H} \, |f(t)\rangle \tag{2.7}$$

with matrix elements:

$$H_{11} = \langle B_q|\mathbf{H}|B_q\rangle \qquad H_{12} = \langle B_q|\mathbf{H}|\overline{B_q}\rangle$$
$$H_{21} = \langle \overline{B_q}|\mathbf{H}|B_q\rangle \qquad H_{22} = \langle \overline{B_q}|\mathbf{H}|\overline{B_q}\rangle$$

The Hamiltonian matrix $\mathbf{H}$ can be decomposed into the mass matrix $\mathbf{M}$ and decay matrix $\mathbf{\Gamma}$, both are 2×2 Hermitian matrices. The mass matrix $\mathbf{M}$ is due to processes with virtual intermediate states which do not lead to decay of the B meson. The decay matrix $\mathbf{\Gamma}$ is due to processes with real intermediate states which can lead to the decay of B meson.

$$i \frac{\partial}{\partial t} \begin{pmatrix} f_1(t) \\ f_2(t) \end{pmatrix} = \mathbf{H} \begin{pmatrix} f_1(t) \\ f_2(t) \end{pmatrix} \equiv \left(\mathbf{M} - \frac{i}{2}\mathbf{\Gamma}\right) \begin{pmatrix} f_1(t) \\ f_2(t) \end{pmatrix} \tag{2.8}$$

$$\mathbf{H} \begin{pmatrix} B_q \\ \overline{B_q} \end{pmatrix} = \begin{pmatrix} M_{11} - \frac{i}{2}\Gamma_{11} & M_{12} - \frac{i}{2}\Gamma_{12} \\ M_{21} - \frac{i}{2}\Gamma_{21} & M_{22} - \frac{i}{2}\Gamma_{22} \end{pmatrix} \begin{pmatrix} B_q \\ \overline{B_q} \end{pmatrix}$$

As both $\mathbf{M}$ and $\mathbf{\Gamma}$ are hermitian matrix, $M_{21} = M_{12}^*$ and $\Gamma_{21} = \Gamma_{12}^*$.

B_q and $\overline{B_q}$ being particle and anti-particle, CPT invariance require, $H_{11} = H_{22}$ or $M_{11} =$

$M_{22} = M$ and $\Gamma_{11} = \Gamma_{22} = \Gamma$.

Diagonal elements of matrix **M** arise from quark masses and binding force, while for **Γ** matrix arise from decay like $B_q \to X$ or $\overline{B_q} \to \overline{X}$, where X is a real state. Off-diagonal elements of **M** are due to $B_q \Longleftrightarrow \overline{B_q}$ transitions with virtual intermediate states, dominated by top quark exchange in the SM. This comes in the real part of the box diagram (see Fig. 2.4a). Off-diagonal elements of **Γ** arise from decays like $B_q \to X \to \overline{B_q}$, and are expected to be small since they belong to absorptive part of the box diagram dominated by internal $(c, \overline{c})$ pairs, hence are highly cabbibo suppressed(see Fig 2.4b). The mixing is due to off-diagonal elements, and corresponds to 3 physical quantities, $|M_{12}|$, $|\Gamma_{12}|$, and $\phi = arg(-\frac{M_{12}}{\Gamma_{12}})$.

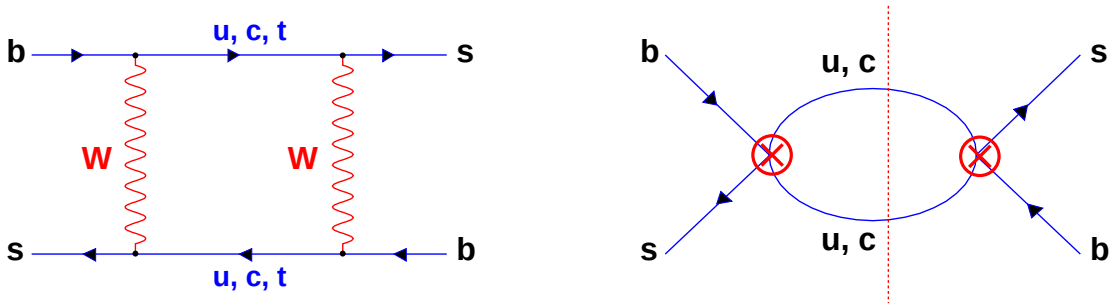

Figure 2.4: (a): General box diagram, real part determines M_{12} (b): Special case of diagram (a) with internal u and c, absorptive part determines Γ_{12}.

The diagonalization of **H** matrix gives two physically observed mass eigenstates denoted by $|B_L\rangle$ and $|B_H\rangle$, also known as "light" and "heavy" mass eigenstates given by:

$$\begin{aligned} |B_L\rangle &= \frac{1}{\sqrt{p^2+q^2}}\left(p|B_q\rangle + q|\overline{B_q}\rangle\right) \\ |B_H\rangle &= \frac{1}{\sqrt{p^2+q^2}}\left(p|B_q\rangle - q|\overline{B_q}\rangle\right) \end{aligned} \tag{2.9}$$

with $|p^2| + |q^2| = 1$, while eigenvalues are given by:

$$\begin{aligned} |F_L\rangle &= \left(M - \tfrac{i}{2}\Gamma\right) + \left(M_{12} - \tfrac{i}{2}\Gamma_{12}\right) \\ |F_H\rangle &= \left(M - \tfrac{i}{2}\Gamma\right) - \left(M_{12} - \tfrac{i}{2}\Gamma_{12}\right) \end{aligned} \tag{2.10}$$

with

$$\frac{q}{p} = \sqrt{\frac{M_{12}^* - \frac{i}{2}\Gamma_{12}^*}{M_{12} - \frac{i}{2}\Gamma_{12}}}$$

Time evolution of state $|f(t)\rangle$, can be rewritten in terms of mass eigenstates $|f(t)\rangle = F_L(t)|B_L\rangle + F_H(t)|B_H\rangle$, where $F_L(t)$ and $F_H(t)$ are given by:

$$\begin{aligned} |F_L(t)\rangle &= F_L(0)\, e^-(\tfrac{\Gamma_L}{2} + iM_L) \\ |F_H(t)\rangle &= F_H(0)\, e^-(\tfrac{\Gamma_H}{2} + iM_H) \end{aligned} \tag{2.11}$$

where, $M_{L,H} = Re(F_{L,H})$ and $\Gamma_{L,H} = -2Im(F_{L,H})$.
At production, the particles are produced in a pure B_q or $\overline{B_q}$ state. So at time t=0, the amplitude must be:

$$\begin{aligned} F_L(0) &= F_H(0) = \tfrac{1}{2p} \qquad \text{for } |f(0)\rangle = |B_q\rangle \\ F_L(0) &= -F_H(0) = \tfrac{1}{2q} \qquad \text{for } |f(0)\rangle = |\overline{B_q}\rangle \end{aligned} \tag{2.12}$$

Using Eqs.2.9, 2.11 and 2.12 time evolution state can be written as:

$$\begin{aligned} |f(t)\rangle &= \tfrac{1}{2\sqrt{p^2+q^2}} \Big(g_+(t)\,|B_q\rangle \;+\; \tfrac{q}{p}\, g_-(t)\,|\overline{B_q}\rangle \Big) \\ |f(t)\rangle &= \tfrac{1}{2\sqrt{p^2+q^2}} \Big(\tfrac{p}{q}\, g_-(t)\,|B_q\rangle \;+\; g_+(t)\,|\overline{B_q}\rangle \Big) \end{aligned} \tag{2.13}$$

Where,

$$\begin{aligned} g_+(t) &= e^-(\tfrac{\Gamma_L}{2} + iM_L) \;+\; e^-(\tfrac{\Gamma_H}{2} + iM_H) \\ g_-(t) &= e^-(\tfrac{\Gamma_L}{2} + iM_L) \;-\; e^-(\tfrac{\Gamma_H}{2} + iM_H) \end{aligned} \tag{2.14}$$

Now one can find the probability of a pure state $|B_q\rangle$ at time t=0, to be $|B_q\rangle$ or to be $|\overline{B_q}\rangle$ at time t. Probabilities can be written in terms of $\Delta M (= M_H - M_L)$ and $\Delta\Gamma (= \Gamma_L - \Gamma_H)$. One can also use these results to relate the observed CP asymmetry with $\Delta\Gamma$ and ΔM. One can obtain the value of ΔM, by measuring CP asymmetry as was done for B_d^0 decay [15].

In case of B_s^0 decay, the observed oscillations are too fast to be resolved with current measurement techniques. Hence ΔM determination for B_s^0 mesons is not yet possible, although limit on its value has been set.

CP operation on neutral B mesons can be written as:

$$\begin{aligned} CP|B_q\rangle &= \lambda_{CP}|\overline{B_q}\rangle \\ CP|\overline{B_q}\rangle &= \lambda_{CP}|B_q\rangle \end{aligned} \tag{2.15}$$

choosing phase $\lambda_{CP} = 1$, the eigenstates of the CP operator will be:

$$\begin{aligned} CP|B_{CPeven}\rangle &= \tfrac{1}{\sqrt{2}}\left(|B_q\rangle - |\overline{B_q}\rangle\right) \\ CP|B_{CPodd}\rangle &= \tfrac{1}{\sqrt{2}}\left(|B_q\rangle + |\overline{B_q}\rangle\right) \end{aligned} \tag{2.16}$$

For B_s^0 mesons, up to a good approximation $\frac{q}{p} = -1$, and this leads to the interesting result that mass eigenstates are nearly CP eigenstates [16]. This result will be used as an important theory tool to separate CP even and CP odd state, while writing the angular distribution for B_s^0 decay.

2.5 Angular Distribution in $B_s^0 \to J/\psi(\to \mu^+\mu^-)\phi(\to K^+K^-)$

The decay $B_s^0 \to J/\psi\phi$, proceeds through the quark sub-process $\overline{b} \to \overline{c}c\overline{s}$ as shown in Fig. 2.5. In decay of $B_s^0 \to J/\psi\phi$, because final states are common to B_s^0 and its charge conjugate $\overline{B_s^0}$, the two meson states are expected to mix in such a way that the two physical eigenstates (mass or CP eigenstates) have a relatively large lifetime difference. Angular analysis of "untagged"[6] $B_s^0 \to J/\psi(\to \mu^+\mu^-)\phi(\to K^+K^-)$ provides an elegant way to separate the two CP components of $B_s^0 \to J/\psi\phi$ and thus to measure the lifetime difference in the $(B_s^0, \overline{B}_s^0)$ system. In addition to extracting lifetime difference and other useful parameters, we may also probe the weak mixing phase $\delta\phi_{\rm CKM}$, which represents a sensitive probe for CP-violating contributions from physics beyond the SM [17, 18].

[6] Unknown B_s^0 flavour at production or decay.

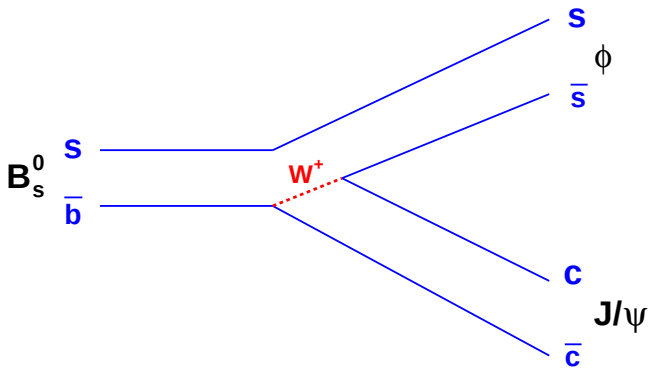

Figure 2.5: Tree level diagram for the decay $B_s^0 \to J/\psi\ \phi$.

The B_s^0 decay is a spin 0 particle decaying to two vector mesons (J/ψ, ϕ). This implies an orbital angular momentum of L=0, 1, 2 between the vector mesons, and the final state will be a mixture between CP-even and CP-odd states with L=0, 2 being CP-even and L=1 corresponding to CP-odd state. The angular distributions of the final state were originally described in terms of helicity [19], which is defined as the sign of the projection of a particle's spin $\vec{s}$ along the direction of its momentum $\vec{p}$:

$$H = \frac{\vec{s} \cdot \vec{p}}{|\vec{s}|\ |\vec{p}\,|} \tag{2.17}$$

However, to separate the CP-even and CP-odd contributions in the final state, it is more convenient to use the so-called *transversity* basis [20] which describes the decay in terms of polarizations analogous to light polarizations. The three amplitudes A_0, $A_\parallel$ and $A_\perp$ refer to longitudinal, parallel and perpendicular polarized states. They are related [21] to the three helicity amplitudes H_0, H_+, and H_- through

$$A_0 = H_0 \qquad A_\parallel = \frac{1}{\sqrt{2}}(H_+ + H_-) \qquad A_\perp = \frac{1}{\sqrt{2}}(H_+ - H_-) \tag{2.18}$$

and are normalized so that

$$\frac{d\mathcal{A}}{dt}(B_s^0(t) \to J/\psi\,\phi) = |A_0|^2 + |A_{||}|^2 + |A_\perp|^2, \tag{2.19}$$

where, $\mathcal{A}$ is the time-dependent rate for $B_s^0 \to J/\psi\phi$ decay. $A_\perp$ measures contribution from CP-odd state, while A_0 and $A_\parallel$ from CP-even states.

The decay amplitude for pure B_s^0 decay (an unmixed B_s^0 meson present in the initial state, i.e. B_s^0 or $\overline{B_s^0}$ identified by tagged B_s^0 decay) can be expressed [22] in terms of linear polarization states as:

$$A(B_s^0(t) \to J/\psi\,\phi) = \frac{A_0(t)}{x}\,\epsilon^{*L}_{J/\psi}\,\epsilon^{*L}_{\phi} - A_\parallel(t)\,\epsilon^{*T}_{J/\psi}\cdot\epsilon^{*T}_{\phi}/\sqrt{2} - iA_\perp(t)\,\epsilon^{*}_{J/\psi}\times\epsilon^{*}_{\phi}\cdot\hat{\mathbf{p}}_\phi/\sqrt{2} \quad (2.20)$$

where $x \equiv p_{J/\psi}\cdot p_\phi/(m_{J/\psi}m_\phi)$ and $\hat{\mathbf{p}}_\phi$ is the unit vector along the direction of motion of ϕ in the rest frame of J/ψ. Here the time dependences originates from B_s^0– $\overline{B}_s^0$mixing. In this notation, an unmixed B_s^0 meson is present at $t = 0$. Since the CP-even and CP-odd components differ in both time evolution and angular correlations, the angular distribution can be used to separate them and their time evolution can be studied individually.

The full angular distribution of the 4-body final state can be expressed in terms of three angles under transversity basis [22]. For $B_s^0 \to J/\psi(\to \mu^+\mu^-)\phi(\to K^+K^-)$, the three-angle distribution of decay amplitude, for the decay of an initially present (B_s^0 or $\overline{B_s^0}$ i.e. tagged) B_s^0 meson is given below:

$$\frac{d^4\mathcal{A}[B_s^0(t) \to J/\psi(\to \mu^+\mu^-)\phi(\to K^+K^-)]}{d\cos\theta\; d\varphi\; d\cos\Psi\; dt} = \frac{9}{32\pi}\Big[\; 2|A_0(t)|^2\cos^2\Psi(1-\sin^2\theta\cos^2\varphi)$$

$$+\sin^2\Psi\{|A_\parallel(t)|^2(1-\sin^2\theta\sin^2\varphi) + |A_\perp(t)|^2\sin^2\theta - \;\mathrm{Im}\;(A^*_\parallel(t)A_\perp(t))\sin 2\theta\sin\varphi\}$$

$$+\frac{1}{\sqrt{2}}\sin 2\Psi\{\;\mathrm{Re}\;(A_0^*(t)A_\parallel(t))\sin^2\theta\sin 2\varphi + \;\mathrm{Im}\;(A_0^*(t)A_\perp(t))\sin 2\theta\cos\varphi\;\}\;\Big], \quad (2.21)$$

The angles in transversity basis are defined in following way: particle ϕ moves in x direction in the J/ψ rest frame. The decay plane of $\phi \to K^+K^-$ makes x-y plane with $p_y(K^+) \geq 0$. The z axis is perpendicular to the x-y plane. The coordinates (θ, φ) describe the decay direction of μ^+ in the J/ψ rest frame. And Ψ is the angle made by $\vec{p}(K^+)$ with the x axis in the ϕ rest frame (these are illustrated in Fig. 2.6). With this convention,

$$\mathbf{x} = \mathbf{p}_\phi, \quad \mathbf{y} = \frac{\mathbf{p}_{K^+} - \mathbf{p}_\phi(\mathbf{p}_\phi\cdot\mathbf{p}_{K^+})}{|\mathbf{p}_{K^+} - \mathbf{p}_\phi(\mathbf{p}_\phi\cdot\mathbf{p}_{K^+})|}, \quad \mathbf{z} = \mathbf{x}\times\mathbf{y}$$

$$\sin\theta\ \cos\varphi = \mathbf{p}_{\ell^+}\cdot\mathbf{x}, \quad \sin\theta\ \sin\varphi = \mathbf{p}_{\ell^+}\cdot\mathbf{y}, \quad \cos\theta = \mathbf{p}_{\ell^+}\cdot\mathbf{z} \tag{2.22}$$
$$\cos\Psi = -\mathbf{p}'_{K^+}\cdot\mathbf{p}'_{J/\psi}$$

The bold-face characters represent unit 3-vectors and everything is measured in the rest frame of J/ψ, while the primed quantities are *unit vectors* measured in the rest frame of ϕ.

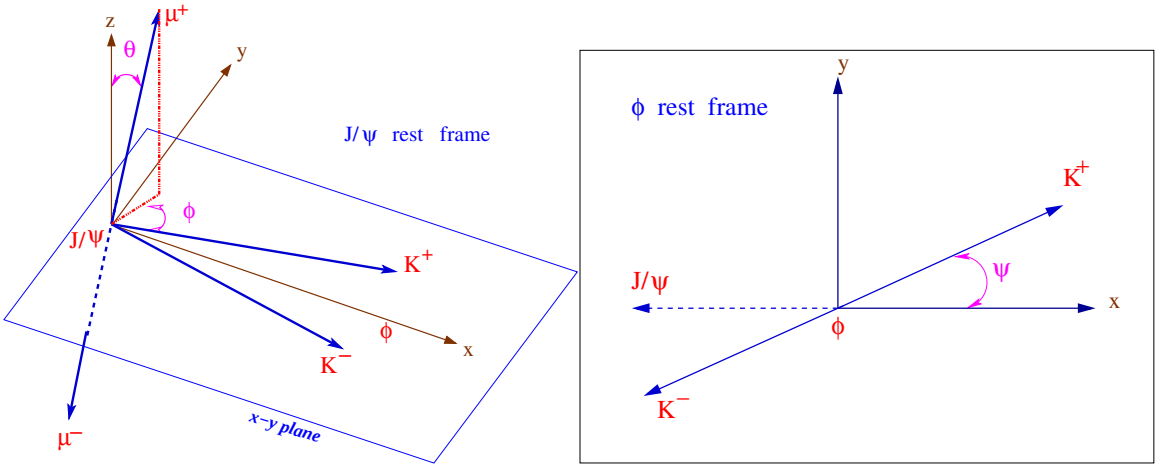

Figure 2.6: schematic diagram of three decay angles, in decay chain of $B_s^0 \to J/\psi\phi(J/\psi \to \mu^+\mu^-, \phi \to K^+K^-)$, used in Eqn. 2.21.

The time evolution of the individual components are given in Table 2.6, where $\Delta m \equiv m_H - m_L > 0$ is the mass difference of the mass eigenstates B_s^H(CP-odd) and B_s^L(CP-even) of the $(B_s^0, \overline{B}_s^0)$ system and $\overline{\Gamma} \equiv (\Gamma_H + \Gamma_L)/2$ denotes their average decay width. The phases $\delta_1 \equiv \mathrm{Arg}(A_\parallel(0)^* A_\perp(0))$ and $\delta_2 \equiv \mathrm{Arg}(A_0(0)^* A_\perp(0))$ are *CP-conserving* strong phases. In the absence of final-state interactions[7], they are expected to be 0 (mod π).

The quantity $\delta\phi_{\mathrm{CKM}}$ (ϕ_{CKM} in SM) is a CP-violating weak phase, which is introduced through interference effects between B_s^0–$\overline{B_s^0}$ mixing and decay processes. It can be expressed in terms of elements of the CKM matrix [23]) as

$$e^{i\phi_{\mathrm{CKM}}} = \frac{V_{ts}V_{tb}^*}{V_{ts}^*V_{tb}}\frac{V_{cs}^*V_{cb}}{V_{cs}V_{cb}^*}, \tag{2.23}$$

[7]Probably not a justifiable assumption for $B_s^0 \to J/\psi\phi$

Observable	Time evolution
$\lvert A_0(t)\rvert^2$	$\lvert A_0(0)\rvert^2 \left[e^{-\Gamma_L t} - e^{-\overline{\Gamma} t}\sin(\Delta m t)\delta\phi_{\rm CKM}\right]$
$\lvert A_\parallel(t)\rvert^2$	$\lvert A_\parallel(0)\rvert^2 \left[e^{-\Gamma_L t} - e^{-\overline{\Gamma} t}\sin(\Delta m t)\delta\phi_{\rm CKM}\right]$
$\lvert A_\perp(t)\rvert^2$	$\lvert A_\perp(0)\rvert^2 \left[e^{-\Gamma_H t} + e^{-\overline{\Gamma} t}\sin(\Delta m t)\delta\phi_{\rm CKM}\right]$
$\mathrm{Re}(A_0^*(t)A_\parallel(t))$	$\lvert A_0(0)\rvert\lvert A_\parallel(0)\rvert\cos(\delta_2-\delta_1)\left[e^{-\Gamma_L t} - e^{-\overline{\Gamma} t}\sin(\Delta m t)\delta\phi_{\rm CKM}\right]$
$\mathrm{Im}(A_\parallel^*(t)A_\perp(t))$	$\lvert A_\parallel(0)\rvert\lvert A_\perp(0)\rvert\left[e^{-\overline{\Gamma} t}\sin(\delta_1-\Delta m t) + \frac{1}{2}\left(e^{-\Gamma_H t} - e^{-\Gamma_L t}\right)\cos(\delta_1)\delta\phi_{\rm CKM}\right]$
$\mathrm{Im}(A_0^*(t)A_\perp(t))$	$\lvert A_0(0)\rvert\lvert A_\perp(0)\rvert\left[e^{-\overline{\Gamma} t}\sin(\delta_2-\Delta m t) + \frac{1}{2}\left(e^{-\Gamma_H t} - e^{-\Gamma_L t}\right)\cos(\delta_2)\delta\phi_{\rm CKM}\right]$

Table 2.6: Time evolution of the decay $B_s^0 \to J/\psi(\to l^+l^-)\phi(\to K^+K^-)$ of an initially (i.e. at $t = 0$) pure B_s^0 meson. For the $\overline{B}_s^0$decay, the terms with Δm have an opposite sign.

In terms of the Wolfenstein expansion, $\phi_{\rm CKM}$ is proportional to the parameter η:

$$\phi_{\rm CKM} = 2\lambda^2\eta = \mathcal{O}(0.03). \tag{2.24}$$

Note that $\lambda = \sin\theta_{\rm C} = 0.22$ is related to the well measured Cabibbo angle, $\theta_{\rm C}$.

Integration of the full three-angle distributions for tagged $B_s^0 \to J/\psi(\to l^+l^-)\phi(\to K^+K^-)$ decays discussed above (and given by Eq. 2.21), over the two decay angles φ and Ψ, leads to the following one-angle distribution[8].

$$\frac{d^2\mathcal{A}}{d\cos\theta\, dt} = \frac{3}{8}\left[\ (|A_0(t)|^2 + |A_\parallel(t)|^2)(1+\cos^2\theta) + 2|A_\perp(t)|^2\sin^2\theta\ \right] \tag{2.25}$$

From Table 2.6 using observables for B_s^0 and $\overline{B_s^0}$, the time integrated decay rate of

[8]In practice, due to limited detector coverage and kinematic thresholds, the detector response to the angles are non-uniform, as shown in Figs. A.1. The parametrization of these angle-dependent acceptance has been taken into account along with 3-angle distribution given in Eq. 2.21. Because of this correction, the final observed decay rate of 1-angle distribution slightly deviates from Eq. (2.25) (see Appendix A for details).

untagged one-angle distribution, can be written as:

$$\frac{d^2\mathcal{A}}{d\cos\theta\, dt} = \frac{3}{8}\Big[\ (1-R_\perp)(1+\cos^2\theta)e^{-\Gamma_L t} + 2R_\perp(1-\cos^2\theta)e^{-\Gamma_H t}\ \Big] \tag{2.26}$$

where, $R_\perp = |A_\perp(0)|^2$.

Eq. 2.26 shows that, in time integrated decay rate of untagged one-angle distribution, the CP-even and CP-odd terms evolve like $(|A_0(0)|^2 + |A_\parallel(0)|^2)e^{-\Gamma_L t}$ and $|A_\perp(0)|^2 e^{-\Gamma_H t}$, respectively. Fit with two exponentials, one to CP-even, other to CP-odd term, gives the decay width Γ_L and Γ_H. Only one parameter is required to get the amplitude of the two exponentials, as sum of them is normalized to one. We call this parameter, the fraction of the CP-odd rate, i.e. $R_\perp$. Above results with proper treatment of detector acceptance are used to study the untagged decay of $B_s^0 \to J/\psi(\to \mu^+\mu^-)\phi(\to K^+K^-)$ and to measure decay widths Γ_L, Γ_H and other physical quantities of $(B_s^0, \overline{B}_s^0)$ system.

All the above relations are obtained under a tacit assumption that the CP-violating phase is negligible, as predicted by Standard Model ($\phi_{\rm CKM} = -0.03$), and that the mass eigenstates coincide with CP eigenstates. New phenomena may cause the effective phase, $\delta\phi_{\rm CKM}$, to deviate from $\phi_{\rm CKM}$. As pointed out in [24], the spontaneously broken left-right (SB–LR) model predicts values for the mixing-induced CP asymmetries of $B_s^0 \to J/\psi\,\phi$, that largely deviate from the SM expectation of very small CP-violating effects. In this case, the relations between $(\Delta\Gamma/\overline{\Gamma})_{\rm SM}$ as given by SM theory prediction, and the observable that we measure are [18]: $\Delta\Gamma/\overline{\Gamma} = (\Delta\Gamma/\overline{\Gamma})_{\rm SM}\cos^2(\delta\phi_{\rm CKM})$.

Eq. 2.26 does not depend on the mass difference $(\Delta m)_{B_s^0}$. The extraction of $(\Delta m)_{B_s^0}$ requires tagging. In the case of tagged measurements, the integrated decay rates

$$\mathcal{A}(t) = \int_{-1}^{+1} d(\cos\theta)\,\frac{d\mathcal{A}(t)}{d\cos\theta} \tag{2.27}$$

evolve in time for initially present B_s^0 and $\overline{B_s^0}$ mesons as

$$\begin{aligned}\mathcal{A}(t) \ \propto\ & \Big(|A_0(0)|^2 + |A_\parallel(0)|^2\Big)\, e^{-\Gamma_L t} + |A_\perp(0)|^2 e^{-\Gamma_H t} \\ & - \Big(|A_0(0)|^2 + |A_\parallel(0)|^2 - |A_\perp(0)|^2\Big)\, e^{-\overline{\Gamma} t}\sin(\Delta m t)\,\delta\phi_{\rm CKM}\end{aligned} \tag{2.28}$$

and

$$\begin{aligned}\overline{\mathcal{A}}(t) \;\propto\; & \left(|A_0(0)|^2 + |A_\parallel(0)|^2\right) e^{-\Gamma_L t} + |A_\perp(0)|^2 e^{-\Gamma_H t} \\ & + \left(|A_0(0)|^2 + |A_\parallel(0)|^2 - |A_\perp(0)|^2\right) e^{-\overline{\Gamma} t} \sin(\Delta m t)\, \delta\phi_{\rm CKM}\,, \end{aligned} \tag{2.29}$$

respectively.

Consequently, the time-dependent CP asymmetry arising in the decay $B_s^0 \to J/\psi\,\phi$ takes the following form:

$$\begin{aligned} a_{\rm CP}(B_s^0(t) \to J/\psi\,\phi) &\equiv \frac{\mathcal{A}(t) - \overline{\mathcal{A}}(t)}{\mathcal{A}(t) + \overline{\mathcal{A}}(t)} \\ &= -\left(\frac{|A_0(0)|^2 + |A_\parallel(0)|^2 - |A_\perp(0)|^2}{\left(|A_0(0)|^2 + |A_\parallel(0)|^2\right) e^{-\Gamma_L t} + |A_\perp(0)|^2 e^{-\Gamma_H t}}\, e^{-\overline{\Gamma} t}\right) \sin(\Delta m t)\, \delta\phi_{\rm CKM} \end{aligned} \tag{2.30}$$

The coefficient of $\sin(\Delta m t)\,\delta\phi_{\rm CKM}$ in Eq. 2.30, can be experimentally determined from the untagged studies. Value of Δm can be extracted (using Eq. 2.30) by tagging of B_s^0 candidates. However, due to limited statistics and very small tagging power, measurement of Δm has not been done in the present work.

Chapter 3

The Tevatron accelerator and DØ Detector for Run II

The Tevatron proton anti-proton ($p\overline{p}$) collider at Fermi National Accelerator Laboratory (FNAL [25]), is the highest-energy particle collider currently operational, at a center of mass energy of 1.96 TeV. The DØ detector is a multi-purpose detector located at one of the interaction points of Tevatron ring. In this chapter we describe in brief, the Tevatron accelerator and DØ detector. Our emphasis will be on the upgrade of the Tevatron and the DØ, for its Run II operation. More details of Tevatron and DØ, may be obtained from [26] [27].

3.1 The Tevatron at Fermilab

The Tevatron is an accelerator complex, where protons and anti-protons are produced and accelerated to collide head on, at center of mass energy of 1.96 TeV. There are several stages to complete this process, starting from producing protons and anti-protons, accelerating them in different components of the accelerator complex to different energies and finally colliding them in the Tevatron ring at two detector points. The Tevatron accelerator overview is shown in Fig. 3.1. The whole process has following main systems:

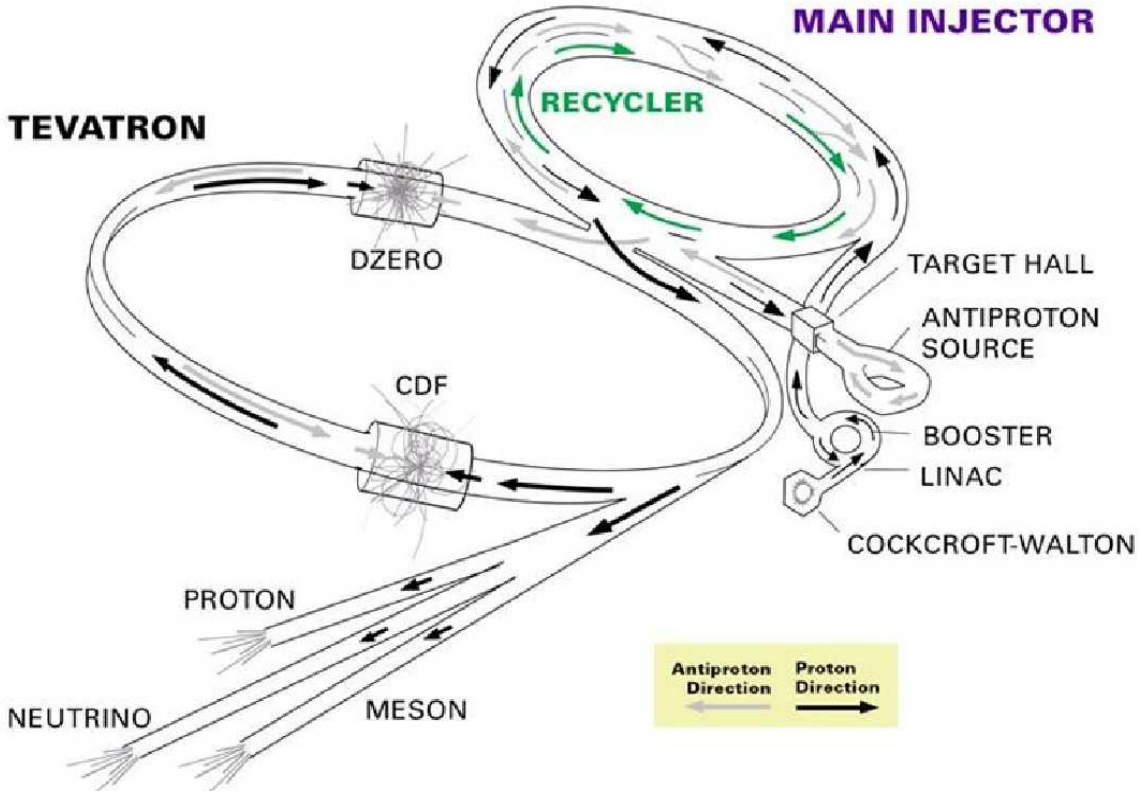

Figure 3.1: Overview of Fermilab Tavatron Collider.

3.1.1 Production of protons and pre-acceleration

In this system we mainly have a Cockroft-Walton accelerator, a linear accelerator (Linac) and a Booster synchrotron. The beam starts in an "ion source", where H^- ions are produced by a electrical discharge from hydrogen gas, and accelerated by a +ve voltage upto 25 keV. These 25 keV H^- ions are released into an electrostatic Cockroft-Walton chamber, which accelerates them upto 750 KeV. After the Cockroft-Walton stage, H^- ions are injected into a 500 feet long Linac, where they are accelerated upto 400 MeV using oscillating electric field. The 400 MeV H^- ions are pass though a carbon foil, which takes out two electrons and leave H^+ ions (or protons). The protons are extracted from beam and steered into the Booster synchrotron ring and accelerated upto 8 GeV. From Booster 5-6$\times 10^{12}$ protons

bunch are made and pulses of 5 to 7 bunches are passed to the Main Injector for next stage of acceleration.

3.1.2 Main Injector (MI)

At this stage anti-proton production and acceleration is performed to inject proton and anti-proton into the Tevatron. Along with MI, other main components are debuncher, accumulator and recycler. Main Injector performs several functions besides accelerating p and $\overline{p}$ to the energy of 150 GeV and injecting them into the Tevatron. MI accepts 8 GeV protons from the Booster and first accelerates them to 120 GeV and delivers them to the anti-proton production target (made of nickel/copper), later it also accepts 8 GeV anti-protons from the anti-proton accumulator and the recycler. From the anti-proton production target, anti-protons are produced with a range of momenta and production angles. These anti-protons are first stochastically cooled to 8 GeV by applying correction signals and then transferred to the accumulator ring, at the rate of 10^{12} anti-protons/hour. From the accumulator, anti-protons are transferred to the permanent magnet storage Recycler ring. These new anti-protons are then added to the ones remaining at the end of the previous collider store. Once enough anti-protons are collected they are again extracted to the Main Injector, to accelerate them from 8 GeV to 150 GeV.

3.1.3 The Tevatron Ring Synchrotron

In the final acceleration process, the 150 GeV $p\overline{p}$ bunches are passed in the opposing direction into the Tevatron ring from the Main Injector. 36 bunches of protons and 36 bunches of anti-protons are loaded in the opposite direction which results in a time interval of 396 ns between two consecutive collision. The Tevatron having approximately 4 miles circumference, uses superconducting magnets and resonant cavities, which can raise the beam energy upto 1 TeV for each p and $\overline{p}$. Once both p and $\overline{p}$ beam are raised to this energy the beams are squeezed in the transverse plane though the low-β quadrapole magnets and collided at

two crossing points: BØ(the location of the CDF detector) and DØ (the location of the DØ detector). The number of collisions per second depends on the instantaneous luminosity given by

$$\mathcal{L} = \frac{10^{-6}\ f\ B\ N_p\ N_{\overline{p}}\ (6\beta_r\gamma_r)}{2\pi\ \beta^*\ (\epsilon_p + \epsilon_{\overline{p}})}\ H(\sigma_l/\beta^*)\ 10^{31}\ /cm^2/sec, \tag{3.1}$$

where, f is bunch revolution frequency ($\equiv$ 47.7 KHz) and B is number of bunches equal to 36 for Run II. $\beta_r\gamma_r$ is relativistic beta $\times$ gamma and equal to 1045. ϵ_p and $\epsilon_{\overline{p}}$ are transverse emittance for proton and anti-proton at the interaction region. β^* is beta function at the interaction region at the collision point[1], which is designed to be equal to 35 cm. H is hour glass factor[2] and lies in the range of 0.60-0.75. N_p and $N_{\overline{p}}$ are bunch intensities for proton and anti-proton of the order of 10^9. σ_l is the bunch length in centimeter. We try to optimize all the parameters to the best possible values for obtaining higher instantaneous luminosity.

3.1.4 Tevatron Upgrade for Run II

- The Fermilab Tevatron has undergone significant upgrades since its operation during Run I(1989-1995). Presently, it is delivering instantaneous luminosity of order of $10^{32}cm^{-2}sec^{-1}$ at 1.96 TeV center-of-mass energy, of $p\overline{p}$ collisions, which is a slightly higher energy than the 1.8 TeV that was available in Run I.

- During Run I, Main Injector was known as Main Ring, which was 400 GeV proton synchrotron. For Run II it was upgraded in a separate tunnel from the Tevatron and is now called Main Injector. The Main Injector performs several functions, but is mainly used as an accelerator for $p\overline{p}$ from 8 GeV to 150 GeV and inject them to the Tevatron. It produces four times more $\overline{p}$ per hour [28] compare to Main Ring.

[1] β^* is related with beam width (σ) in transverse plane through following relation: $\sigma^2 = \epsilon_{eff}\left(\beta^* + \frac{(z-z_0)^2}{\beta^*}\right)$, where $\epsilon_{eff} = \frac{\epsilon_p\epsilon_{\overline{p}}}{\epsilon_p+\epsilon_{\overline{p}}}$.

[2] Effective number due to increase of the β^* along the $p-\overline{p}$ bunches during collision.

- A new permanent magnet "Recycler Ring" [29] allows recovery and reuse of uncollided anti-protons. The number of bunches is increased to 36 of p and 36 of $\overline{p}$ from 6 bunches of each species.

3.2 The DØ Detector for Run II

To take advantage of the Tevatron improvements and to enhance the physics reach of the experiment, the DØ detector[3] has underwent significant upgrade before its Run II operation. The upgraded detector consists of three major subsystems: central tracking detectors, uranium/liquid-argon calorimeters, and a muon spectrometer. The central tracking system has been completely replaced by a new system, which includes a silicon microstrip tracker and a scintillating-fiber tracker located within a 2 T solenoidal magnet. Between the solenoidal magnet and the central calorimeter and in front of the forward calorimeters, preshower detectors have been added for improved electron identification. In the forward muon system, proportional drift chambers have been replaced by mini drift tubes and trigger scintillation counters while additional shielding has been added to the beam pipe. In the central region, scintillation counters have been added for improved muon triggering. Forward proton detector is also added for the study of diffractive physics. A side view of the upgraded DØ detector is shown in Fig. 3.2.

To cope up with much higher instantaneous luminosity compared to Run I, DØ Run II upgrade required the improvement of the read-out electronics and the implementation of pipelining for the front-end signals from the tracking, calorimeter, and muon systems. The calorimeter preamplifiers, signal-shaping electronics, and the electronics for the muon system have been replaced. The trigger system has been significantly upgraded, providing three full trigger levels to cope with the higher collision rate. Muon triggering has been enhanced by the addition of scintillation counters in the central and forward regions.

[3]The description of upgraded DØ detector is based on [30].

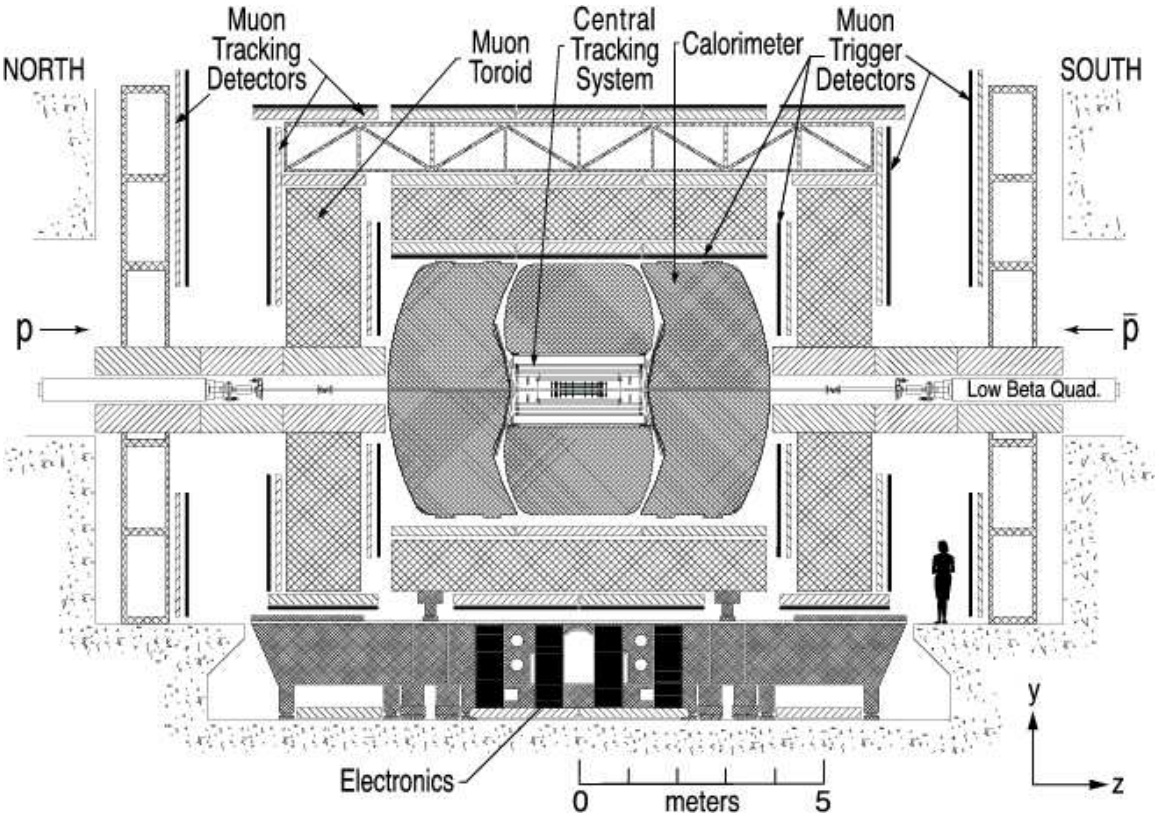

Figure 3.2: Diagram of the upgraded DØ detector, as installed in the collision hall and viewed from inside the Tevatron ring. The forward proton detector is not shown. The detectors in the central region of the detector are shown in Fig. 3.3.

3.3 The DØ Coordinate System

In the detector description and data analysis, we use a right-handed coordinate system in which the z-axis is along the proton direction and the y-axis is upward (Fig. 3.2). The angles ϕ and θ are the azimuthal and polar angles, respectively.

The rapidity y is defined as: $y = \frac{1}{2} \ln \frac{E+p_z}{E-p_z}$.

The pseudorapidity, $\eta = -\ln[\tan(\theta/2)]$, approximates the true rapidity, for finite angles in the limit $(m/E) \to 0$. We use the term "forward" to describe the regions at $|\eta| > 1$.

3.4 Central Tracking

The central tracking system consists of the silicon microstrip tracker (SMT) and the central fiber tracker (CFT) surrounded by a solenoidal magnet. It surrounds the DØ beryllium beam pipe, which has a wall thickness of 0.508 mm and an outer diameter of 38.1 mm, and is 2.37 m long. Combined SMT and CFT information, provide excellent tracking performance. The track momentum resolution is $\sigma(p_T)/p_T^2 \sim 0.2\%$, with track reconstruction efficiency of more than 95%. The impact parameter resolution is ∼20 microns in the transverse plane, and ∼40 microns along the beamline. A schematic view of the central tracking system is shown in Fig. 3.3.

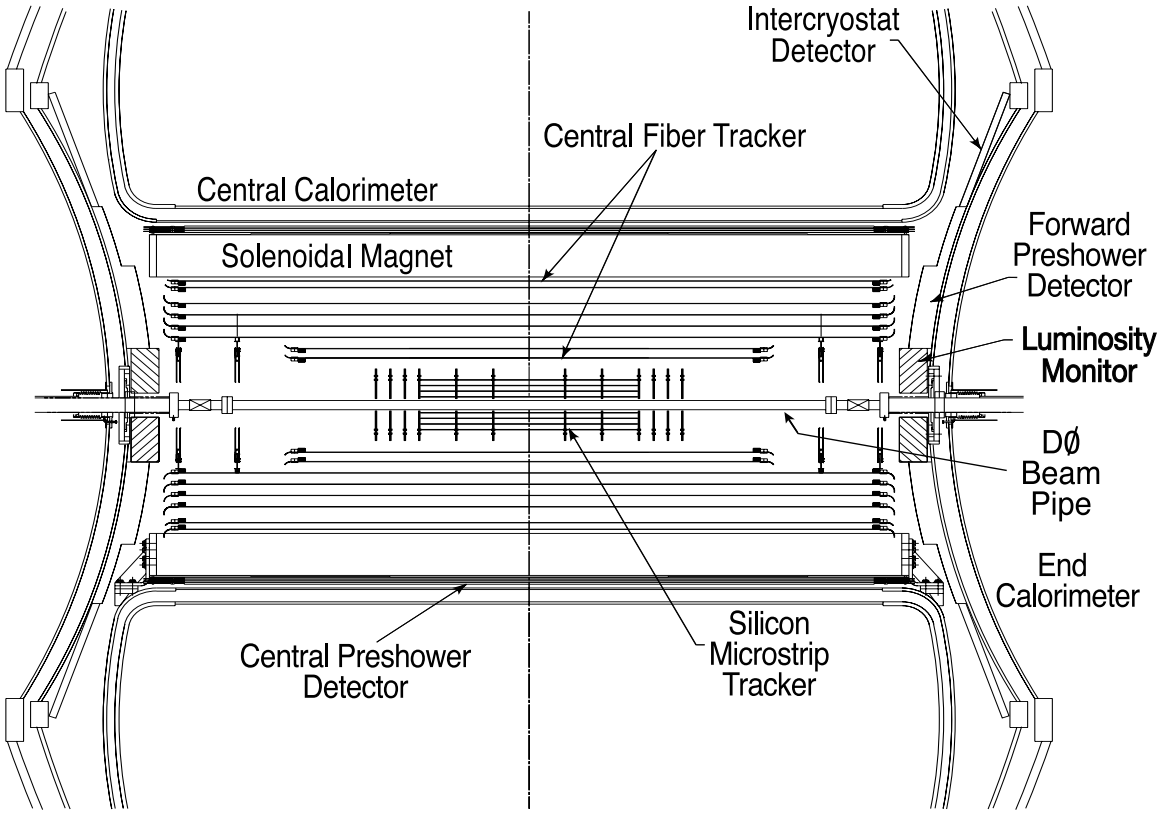

Figure 3.3: Cross-sectional view of the new central tracking system in the $y-z$ plane. Also shown are the locations of the solenoid, the preshower detectors, luminosity monitor, and the calorimeters.

3.4.1 Silicon Microstrip Tracker (SMT)

The SMT provides both track and vertex information over nearly the full η coverage of the calorimeter and muon systems. The SMT has a design of barrel modules interspersed with disks in the central region and assemblies of disks in the forward regions such that tracks are generally perpendicular to detector surfaces for all η. The barrel detectors primarily measure the $r-\phi$ coordinate and the disk detectors measure $r-z$ as well as $r-\phi$. Thus vertices for particles at high η are reconstructed in three dimensions by the disks, and vertices of particles at small values of η are determined using the barrels and central fiber tracker.

An isometric view of the SMT is shown in Fig. 3.4. The detector has six barrels in the central region. Each barrel has four silicon readout layers. The silicon modules installed in the barrels are called "ladders." Layers 1 and 2 have twelve ladders each; layers 3 and 4 have twenty-four ladders each, for a total of 432 ladders. Each barrel is capped at high $|z|$ with a disk of twelve double-sided wedge detectors, called an "F-disk." Forward of the three disk/barrel assemblies on each side is a unit consisting of three F-disks. In the far forward regions, two large-diameter disks, "H-disks," provide tracking at high $|\eta|$. Twenty-four full wedges, each consisting of two back-to-back single-sided "half" wedges, are mounted on each H-disk. There are 144 F-wedges and 96 full H-wedges in the tracker; each side of a wedge (upstream and downstream) is read out independently. There is a grand total of 912 readout modules, with 792,576 channels. The centers of the H-disks are located at $|z| = 100.4,\ 121.0$ cm; the F-disks are at $|z| = 12.5,\ 25.3,\ 38.2,\ 43.1,\ 48.1$, and 53.1 cm. The centers of the barrels are at $|z| = 6.2,\ 19.0,\ 31.8$ cm. The SMT is read out by custom-made 128-channel SVXIIe readout chips [31].

The SMT uses a combination of single-sided (SS), double-sided (DS), and double-sided double-metal (DSDM) sensors. Table 3.1 shows the sensor types used in the SMT and their locations. Disk sensors are trapezoids with readout strips arranged parallel to the long edge of the devices. This provides an effective 30° stereo angle for the double-sided F-disks. A wedge for the H-disks consists of a pair of single-sided half-wedges mounted back-to-back,

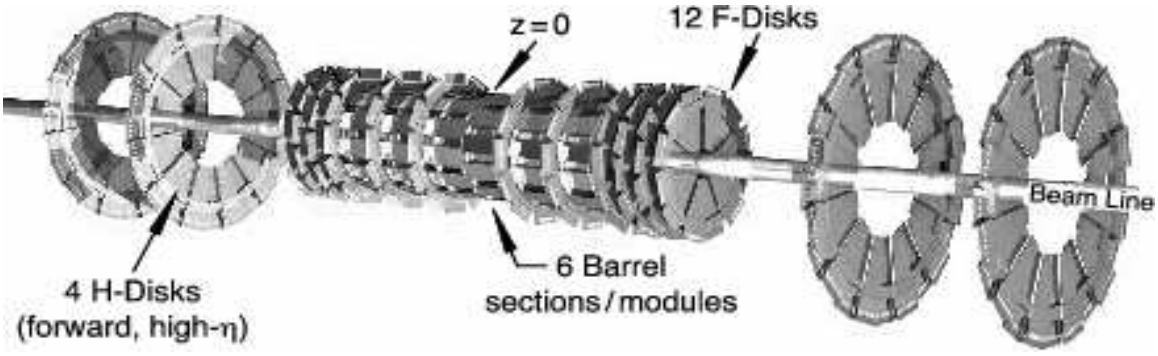

Figure 3.4: The disk/barrel design of the silicon microstrip tracker.

Module	Type	Layer	Pitch (μm) p/n	Length (cm)	Inner radius (cm)	Outer radius (cm)
F-disks	DS	–	50/62.5	7.93	2.57	9.96
H-disks	SS	–	40 80 readout	7.63^i 6.33^o	9.5	26
Central barrels (4)	DSDM	1, 3	50/153.5	12.0	2.715	7.582
	DS	2, 4	50/62.5	12.0	4.55	10.51
Outer barrels (2)	SS	1, 3	50	12.0	2.715	7.582
	DS	2, 4	50/62.5	12.0	4.55	10.51

Table 3.1: Characteristics and deployment of various sensor types in the SMT. i indicates the length of the inner H-disk sensor; o is the length of the outer H-disk sensor.

giving an effective stereo angle of 15°.

3.4.2 Central Fiber Tracker (CFT)

The CFT consists of scintillating fibers mounted on eight concentric support cylinders and occupies the radial space from 20 to 52 cm from the center of the beampipe. To accommodate the forward SMT H-disks, the two innermost cylinders are 1.66 m long; the outer six cylinders are 2.52 m long. The outer cylinder provides coverage for $|\eta| \lesssim 1.7$. Each cylinder supports one doublet layer of fibers oriented along the beam direction (z) and a

second doublet layer at a stereo angle in ϕ of $+3^\circ$ (u) or -3° (v). Doublet layers with fibers oriented along the beam axis are referred to as axial layers, while the doublet layers oriented at small angles are referred to as stereo layers. From the smallest cylinder outward, the fiber doublet orientation is $zu - zv - zu - zv - zu - zv - zu - zv$. The scintillating fibers are coupled to clear fiber waveguides which carry the scintillation light to visible light photon counters for read out. The small fiber diameter (835 μm) gives the CFT an inherent doublet layer resolution of about 100 μm as long as the location of the individual fibers is known to better than 50 μm. Scintillating fiber detectors are discussed in detail in [32].

Discriminator signals from the axial doublet layers are used to form a fast Level 1 hardware trigger based upon the number of track candidates above specified p_T thresholds (with a minimum threshold of 1.5 GeV/c). Level 1 track candidates are used by the Level 2 trigger, while the Level 3 trigger uses the full CFT readout information.

3.4.3 Solenoidal Magnet

The superconducting solenoidal magnet was designed [33, 34] to optimize the momentum resolution, $\delta p_T/p_T$, and tracking pattern recognition within the constraints imposed by the Run I detector. The overall physical size of the magnet was determined by the available space within the central calorimeter vacuum vessel: 2.73 m in length and 1.42 m in diameter. A central field of 2 T was selected after considering the momentum resolution and tracking pattern recognition, the available space, and the thickness of the cryostat which depends on the thicknesses of the conductor and support cylinder. In addition, the magnet is required *i*) to operate safely and stably in either polarity, *ii*) to have a uniform field over as large a percentage of the volume as practical, *iii*) to be as thin as possible to make the tracking volume as large as possible, and *iv*) to have an overall thickness of approximately one radiation length (X_0) at $\eta = 0$ to optimize the performance of the central preshower detector mounted outside the solenoid cryostat. Services such as cryogenics, magnet current buses, vacuum pumpout and relief, reach the magnet from the control dewar through a narrow space (7.6 cm) between the central and end calorimeter vacuum vessels. The magnet system

is controlled remotely, including cool down, energization, de-energization for field reversal, quench recovery, and warmup, without access to the magnet cryostat, service chimney, or control dewar.

Addition of solenoidal magnet for central tracking system made a substantial improvement in the DØ low p_T (transverse momentum) program. It provides a good measurement of momentum and charge of the particles including muons, since muon momentum resolution from the central tracking system is much better than that from the stand-alone muon system. It enhances the physics reach of DØ, specially in the forward region.

3.5 Preshower Detectors

The preshower detectors aid in electron identification and background rejection during both triggering and offline reconstruction. They function as calorimeters as well as tracking detectors, enhancing the spatial matching between tracks and calorimeter showers [35]. The detectors can be used offline to correct the electromagnetic energy measurement of the central and end calorimeters for losses in the solenoid and upstream material, such as cables and supports. Their fast energy and position measurements allow preshower information to be included in the Level 1 trigger. The central preshower detector (CPS) covers the region $|\eta| < 1.3$. It is located between the solenoid and the central calorimeter, with an inner radius of 71.8 cm and an outer radius of 74.2 cm. The two forward preshower detectors (FPS) [36] cover $1.5 < |\eta| < 2.5$ and are attached to the faces of the end calorimeters. The preshower detectors can be seen in Fig. 3.3.

3.5.1 Common properties of the preshower detectors

Both preshower detectors are made from triangular strips of scintillator, as shown in Fig. 3.5. Since the triangles are interleaved, there is no dead space between strips and most tracks traverse more than one strip, allowing for strip-to-strip interpolations and improved position

measurement. The strips are made by extruding polystyrene plastic doped with 1% p-terphenyl and 150 ppm diphenyl stilbene, with a light yield similar to that of commercial Bicron BC-404 scintillator. Each scintillator strip is machine-wrapped in aluminized mylar for optical isolation, and the ends are painted white to enhance reflectivity. The packing density is different for the CPS and the FPS modules, resulting in different layer thicknesses and strip pitches. Because of the nesting process, which requires epoxying the strips together to form a layer, the measured pitch can differ by up to 20% from the design dimensions shown in Fig. 3.5. After extrusion and wrapping, the triangular strips have a tendency to bow. To relieve stress in the plastic, and make them easier to handle, the strips were slumped to the required shapes by heating them to about 180° F for two hours, followed by gradual cooling at room temperature.

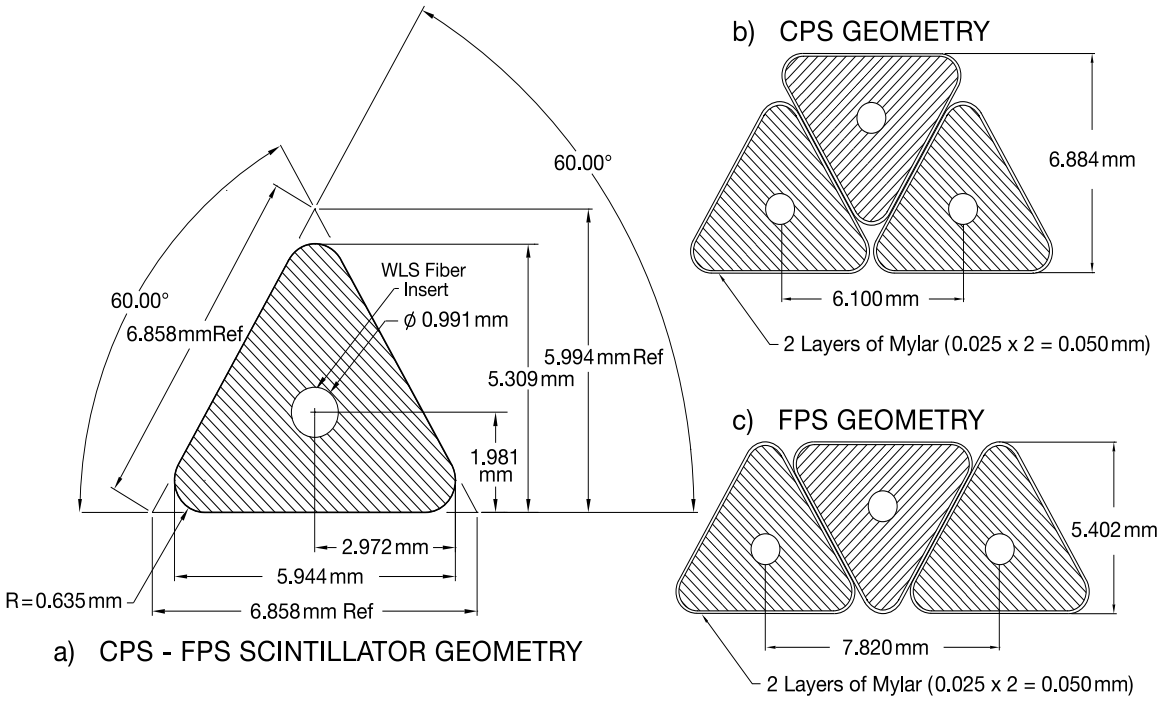

Figure 3.5: Cross section and layout geometry of the CPS and FPS scintillator strips. The circles show the location of the embedded wavelength-shifting fibers. Design dimensions are shown.

Embedded at the center of each triangular strip is a wavelength-shifting fiber that collects and carries the light to the end of the detector. The non-readout ends of the WLS fibers are diamond-polished and silvered. At the readout end, fibers are grouped into bunches of sixteen, and potted into connectors for transition to clear light-guide fibers. Light is transmitted via the clear fibers to visible light photon counters (VLPC) cassettes for readout.

3.5.2 Central Preshower Detector

The CPS consists of three concentric cylindrical layers of triangular scintillator strips and is located in the nominal 5 cm gap between the solenoid and the central calorimeter. Between the solenoid and the CPS is a lead radiator 0.56 cm thick (approximately 1 radiation length (X_0)) and 244 cm long, covering $|\eta| < 1.31$. The lead is covered by stainless steel skins 0.08 cm thick and 262 cm long. The solenoid itself is $0.9X_0$ thick, providing a total of about two radiation lengths of material for particles at normal incidence, increasing to about four radiation lengths at the largest angles.

The three layers of scintillator are arranged in an axial-u-v geometry, with a u stereo angle of 23.774° and a v stereo angle of 24.016°. Each layer contains 1280 strips. The WLS fibers are split at $z = 0$ and read out from each end resulting in 2560 readout channels/layer.

3.5.3 Forward Preshower Detector

The FPS detectors are mounted on the spherical heads of the two end calorimeter cryostats (north and south), occupying the region between the luminosity monitor (see section 3.9) at the inner edge and the intercryostat detectors at the outer edge. Each detector is made from two layers, at different z, of two planes of scintillator strips. A $2X_0$-thick lead-stainless-steel absorber separates the two layers, as shown in Fig. 3.6. The upstream layers (those nearest the interaction region) are known as the minimum ionizing particle, or MIP, layers while the downstream layers behind the absorber are called the shower layers. Charged particles passing through the detector will register minimum ionizing signals in the MIP

layer, allowing measurement of the location (in η, ϕ, and z) of the track. Electrons will readily shower in the absorber, leading to a cluster of energy, typically on the order of three strips wide, in the shower layer that is spatially matched with the MIP-layer signal. Heavier charged particles are less likely to shower, typically producing a second MIP signal in the shower layer. Photons will not generally interact in the MIP layer, but will produce a shower signal in the shower layer. The shower layers cover the region $1.5 < |\eta| < 2.5$ while the MIP layers and the absorber cover the region $1.65 < |\eta| < 2.5$. The outer region of the FPS, $1.5 < |\eta| < 1.65$, lies in the shadow of the solenoidal magnet coil, which provides up to $3X_0$ of material in front of the FPS. This amount of material readily induces showers that can be identified in the shower layers of the detector.

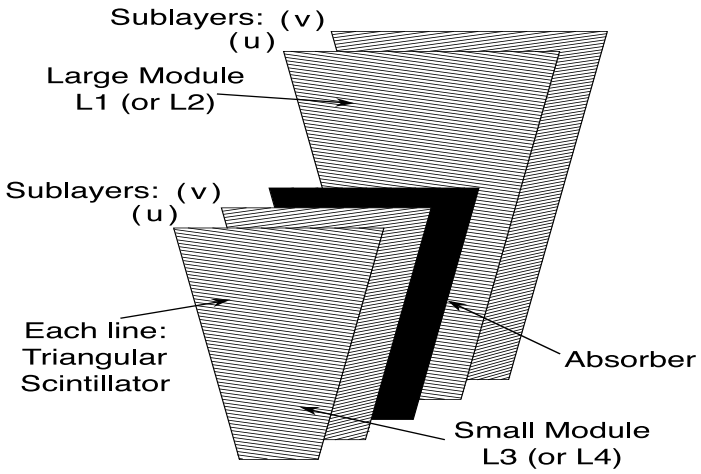

Figure 3.6: Complete ϕ-segment of a FPS module showing the overlapping $u - v$ MIP and shower layers, separated by a lead and stainless steel absorber.

3.6 Calorimetry

The DØ calorimeter system consists of three sampling calorimeters (electromagnetic, fine hadronic and coarse hadronic) and an intercryostat detector.

3.6.1 Calorimeters

The calorimeters were designed to provide energy measurements for electrons, photons, and jets in the absence of a central magnetic field (as was the case during Run I of the Tevatron), as well as assist in identification of electrons, photons, jets, and muons and measure the transverse energy balance in events. The calorimeters themselves are unchanged from RunI, described in detail in [27] and are illustrated in Fig. 3.7, while the readout electronics is new for RunII.

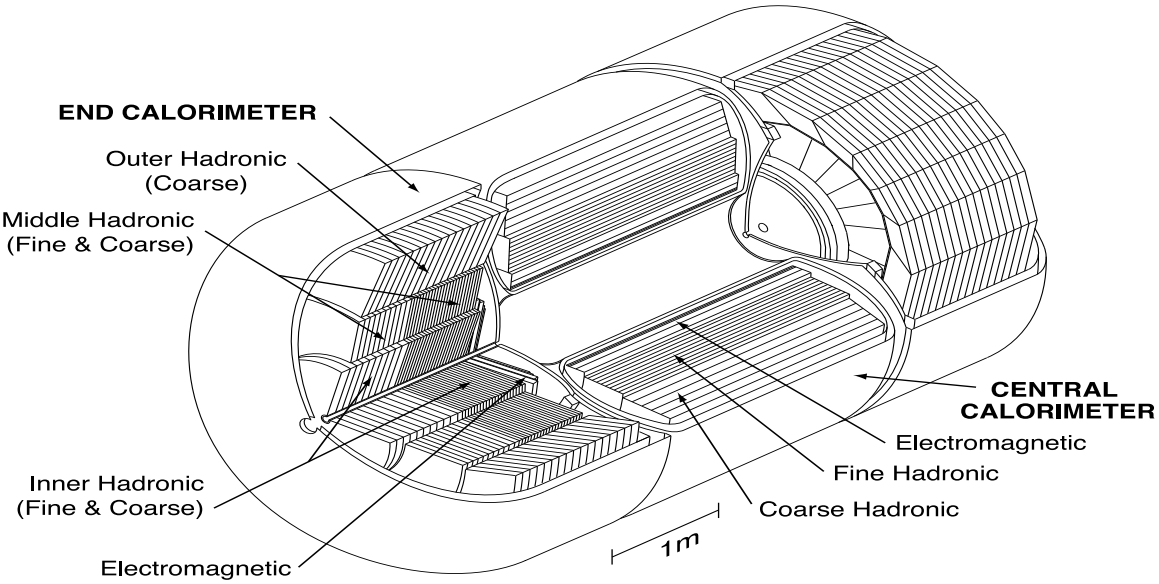

Figure 3.7: Isometric view of the central and two end calorimeters.

As shown in Fig. 3.8, the central calorimeter (CC) covers $|\eta| \lesssim 1$ and the two end calorimeters, ECN (north) and ECS (south), extend coverage to $|\eta| \approx 4$. Each calorimeter contains an electromagnetic section closest to the interaction region followed by fine and coarse hadronic sections. The active medium for the calorimeters is liquid argon and each of the three calorimeters (CC, ECN, and ECS) is located within its own cryostat that maintains the detector temperature at approximately 90 K. Different absorber plates are used in different locations. The electromagnetic sections (EM) use thin plates (3 or 4 mm in

the CC and EC, respectively), made from nearly pure depleted uranium. The fine hadronic sections are made from 6-mm-thick uranium-niobium (2%) alloy. The coarse hadronic modules contain relatively thick (46.5 mm) plates of copper (in the CC) or stainless steel (in EC).

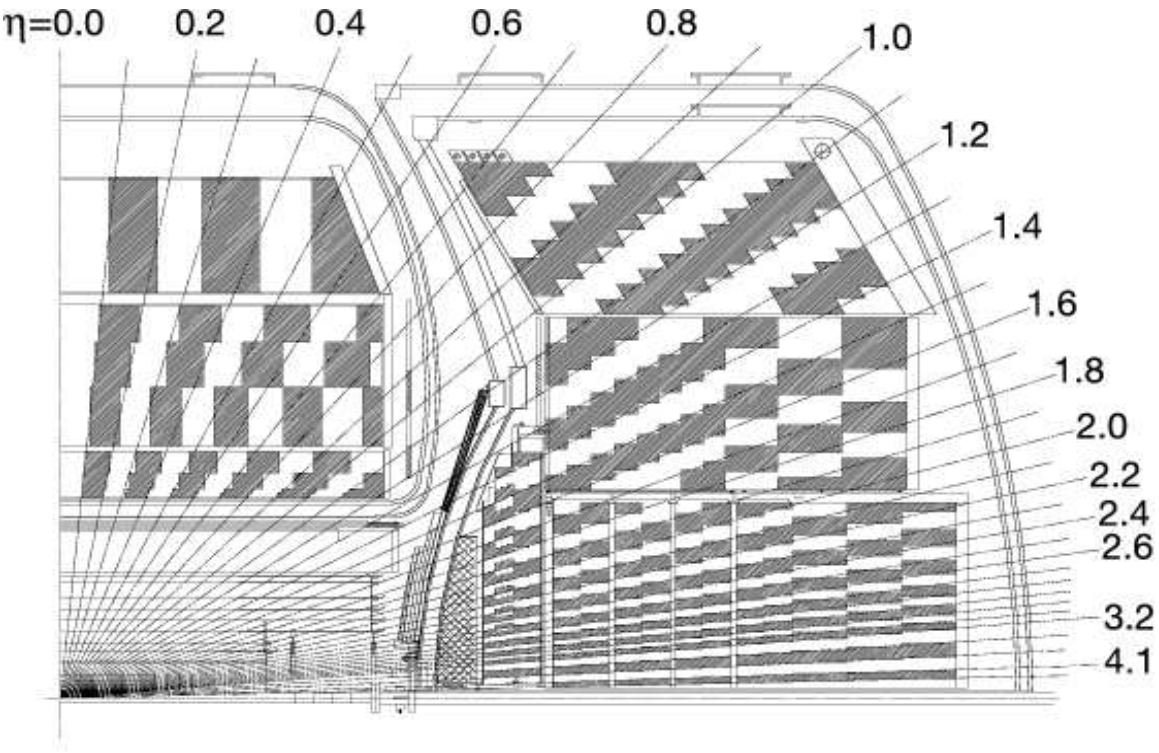

Figure 3.8: Schematic view of a portion of the DØ calorimeters showing the transverse and longitudinal segmentation pattern. The shading pattern indicates groups of cells ganged together for signal readout. The rays indicate pseudorapidity intervals from the center of the detector.

A typical calorimeter cell is shown in Fig. 3.9. The electric field is established by grounding the metal absorber plates and connecting the resistive surfaces of the signal boards to positive high voltage (typically 2.0 kV). The electron drift time across the 2.3 mm liquid argon gap is approximately 450 ns. Signal boards for all but the EM and small-angle

hadronic modules in the EC are made from two 0.5 mm G-10 sheets. The surfaces of the sheets facing the liquid argon gap are coated with carbon-loaded epoxy [37] with a typical sheet resistivity of 40 M$\Omega/meter$; these surfaces serve as the high voltage electrodes for the gap. For one sheet, the other surface is bare G-10; the facing inner surface of the second sheet, originally copper-coated, is milled into the pattern necessary for segmented readout. Several such pads at approximately the same η and ϕ are ganged together in depth to form a readout cell.

Calorimeter readout cells form pseudo-projective towers as shown in Fig. 3.8, with each tower subdivided in depth. We use the term "pseudo-projective" because the centers of cells of increasing shower depth lie on rays projecting from the center of the interaction region, but the cell boundaries are aligned perpendicular to the absorber plates. Pseudo-projective towers have been segmented into covering of $\eta \times \phi = 0.1 \times 0.1$ rad, except third EM layer, where shower is at its maximum development, where maximum shower develops,

the segmentation is even finer for the covering $\eta \times \phi = 0.05 \times 0.05$ rad.

The calorimeter provides hermetic coverage to $|\eta| < 4$. The energy resolution is $\sigma_E/E = 15\%/\sqrt{E(GeV)} \oplus 0.4\%$ for electromagnetic showers. For hadronic jets the resolutions are $\sim 50\%/\sqrt{E(GeV)}$ and $\sim 80\%/\sqrt{E(GeV)}$ for pions and jets respectively.

3.7 Muon System

For muon triggering and measurement, the upgraded detector uses the original central muon system proportional drift tubes (PDTs) and toroidal magnets [27], central scintillation counters (some new and some installed during Run I), and a completely new forward muon system[4]. The central muon system provides coverage for $|\eta| \lesssim 1.0$. The new forward muon system extends muon detection to $|\eta| \approx 2.0$, uses mini drift tubes (MDTs) rather than PDTs, and includes trigger scintillation counters and beam pipe shielding. The small angle muon system [27] of the original detector, including its associated magnets, has been removed.

[4]For detailed description of DØ RunII muon system, see [38].

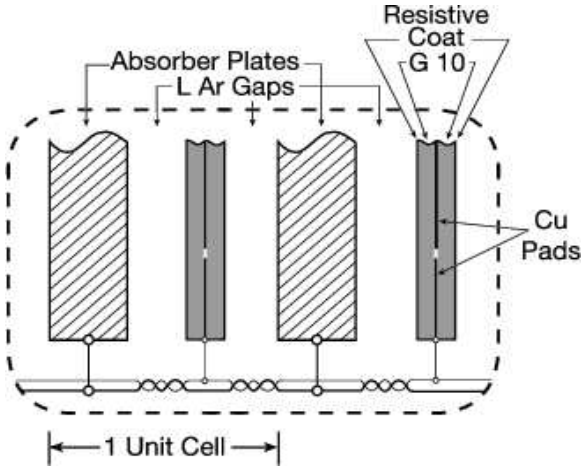

Figure 3.9: Schematic view of the liquid argon gap and signal board unit cell for the calorimeter.

During Run I, a set of scintillation counters, the cosmic cap [39], was installed on the top and upper sides of the outer layer of central muon PDTs. This coverage has been extended to the lower sides and bottom of the detector, to form the cosmic bottom. These trigger scintillation counters are fast enough to allow us to associate a muon in a PDT with the appropriate bunch crossing and to reduce the cosmic ray background. Additional scintillation counters, the $A\phi$ counters, have been installed on the PDTs mounted between the calorimeter and the toroidal magnet. The $A\phi$ counters provide a fast detector for triggering and identifying muons and for rejecting out-of-time background events.

The scintillation counters are used for triggering; the wire chambers are used for precise coordinate measurements as well as for triggering. Both types of detectors contribute to background rejection: the scintillator with timing information and the wire chambers with track segments.

Muon detector components are discussed in the following sections; original components are described briefly. Exploded views of the muon system are shown in Fig.s 3.10 and 3.11.

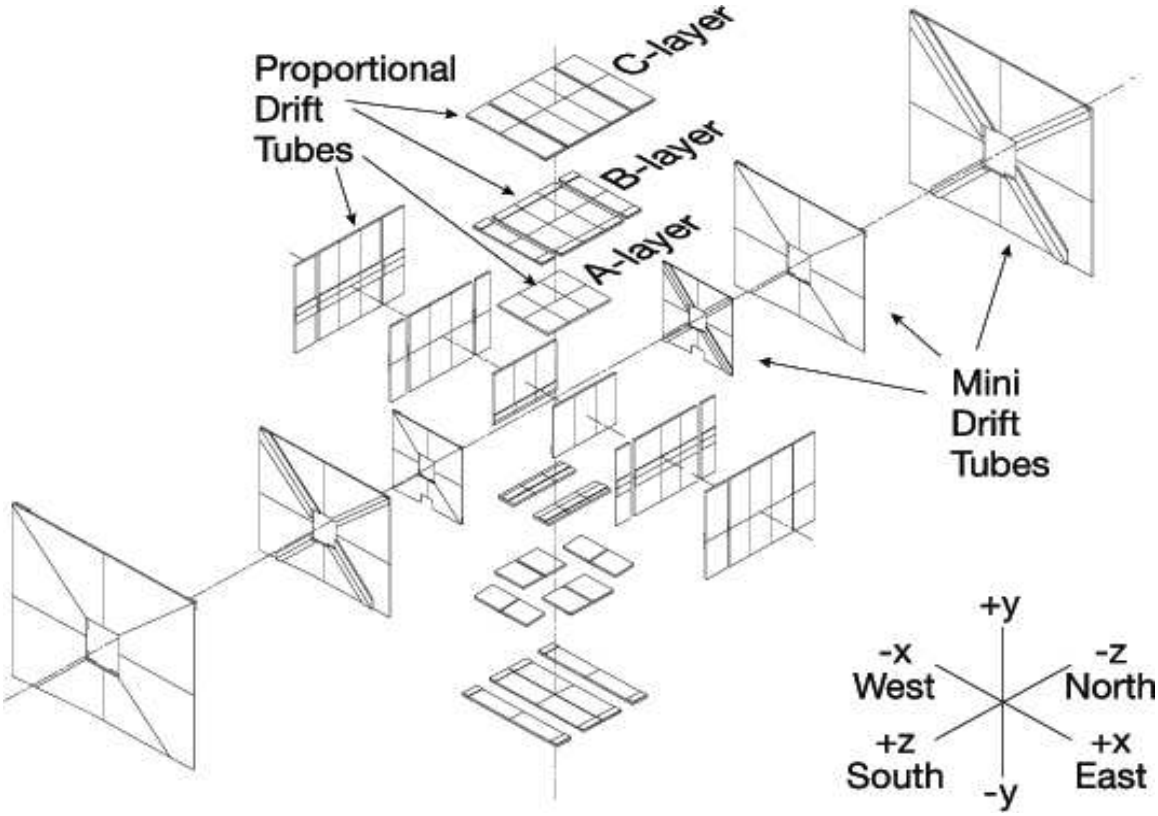

Figure 3.10: Exploded view of the muon wire chambers.

3.7.1 Toroidal Magnets

The toroidal magnets are described in detail in [27] and visible in figures 3.2. Although offline measurement of the muon momentum is performed using the new central tracking system, this muon-system momentum measurement helps in following way:

i) enables a low-p_T cutoff in the Level 1 muon trigger,

ii) allows for cleaner matching with central detector tracks,

iii) rejects π/K decays, and

iv) improves the momentum resolution for high momentum muons.

The central toroid is a 109 cm thick square annulus, whose inner surface is about 318 cm

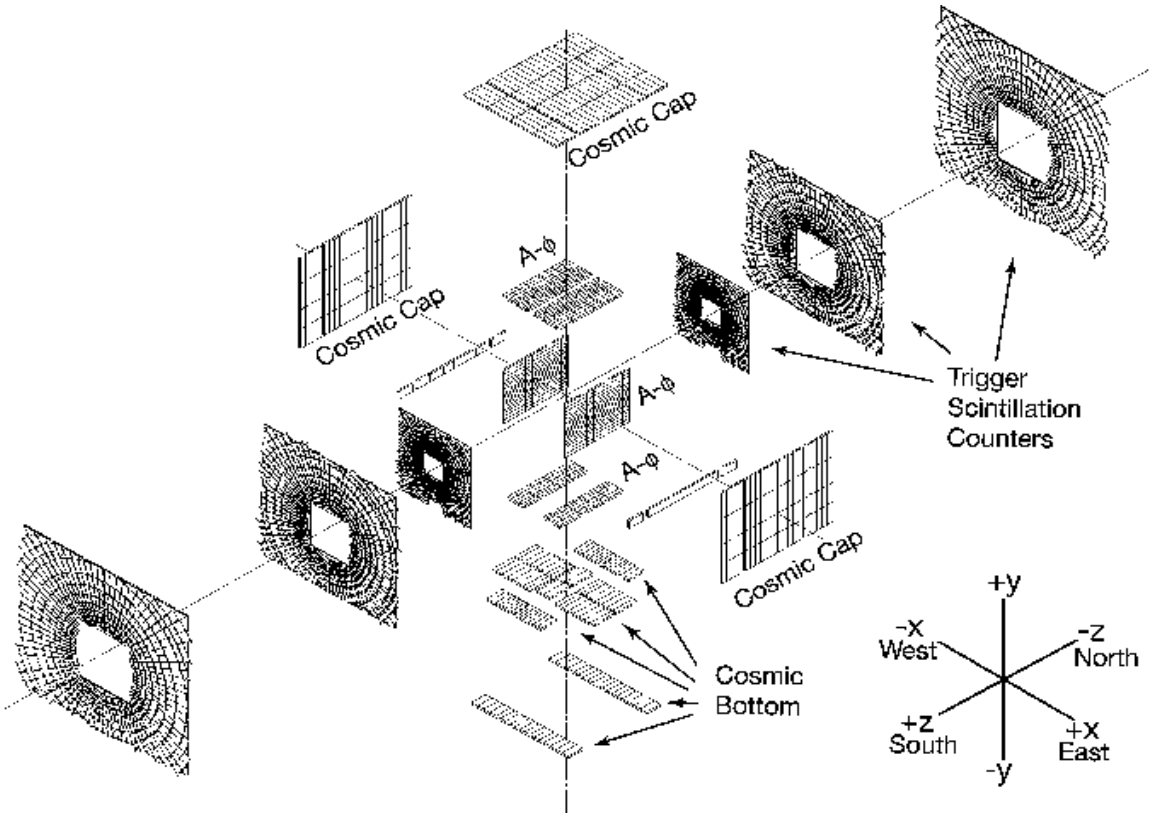

Figure 3.11: Exploded view of the muon scintillation counters.

from the Tevatron beamline; it covers the region $|\eta| \lesssim 1$. To allow access to the inner parts of the detector, it was constructed in three sections. The center-bottom section is 150-cm-wide beam, fixed to the detector platform, which provides a base for the calorimeters and central tracking detectors.

3.7.2 Central Muon Detector

The central muon system consists of a toroidal magnet (Section 3.7.1), drift chambers, cosmic cap, bottom scintillation counters, and the $A\phi$ scintillation counters.

Central Muon Drift Chambers

The drift chambers are described in detail in [27]. These are the same chambers as that of Run I, but with new electronics. The three layers of drift chambers are located inside (A layer) and outside (B and C layers) of the central toroidal magnet and cover $|\eta| \lesssim 1$. Approximately 55% of the central region is covered by three layers of PDTs; close to 90% is covered by at least two layers. Fig. 3.12 shows the geometry of the PDT cells. The drift chambers are large, typically 2.8×5.6 m^2, and made of rectangular extruded aluminum tubes. The cells are 10.1 cm across; typical chambers are 24 cells wide and contain 72 or 96 cells. Along with an anode wire at the center of each cell, vernier cathode pads are located above and below the wires to provide information on the hit position along the wire. The wires are ganged together in pairs within a deck and then read out by electronics located at one end of each chamber.

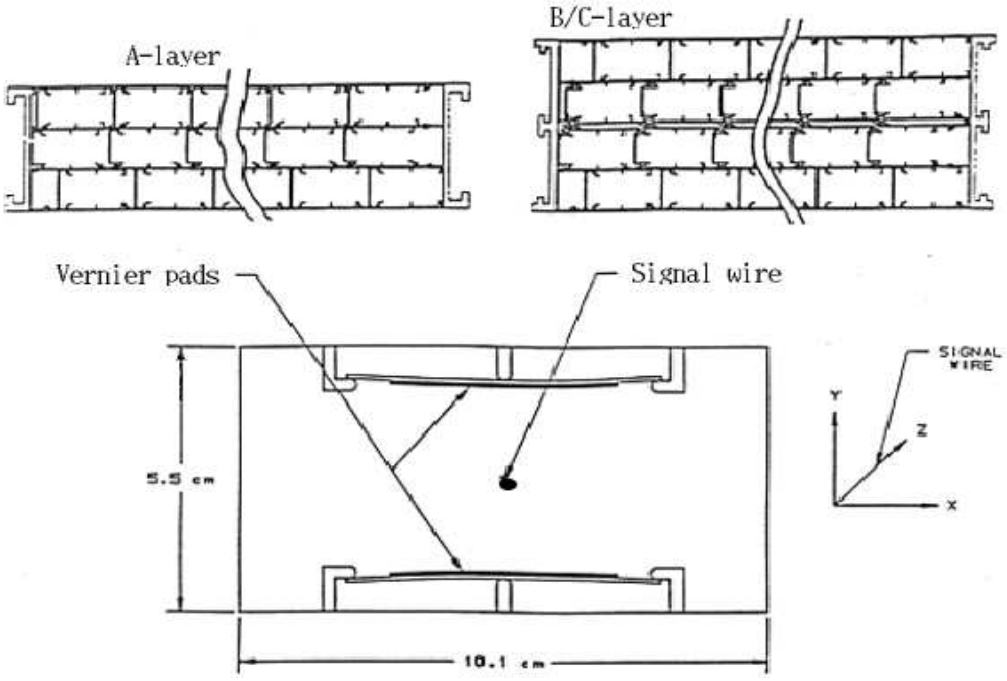

Figure 3.12: Geometry of a PDT cell.

Cosmic Cap and Bottom Counters

The cosmic cap and bottom counters are installed on the top, sides and bottom of the outer layer of the central muon PDTs. They provide a fast timing signal to associate a muon in a PDT with the appropriate bunch crossing and discriminate against the cosmic ray background.

The cosmic cap counters are described in detail in [39]. They are made from grooved 1.27 cm Bicron 404A scintillator with Bicron BCF 91A and Kuraray Y11 wave-shifting fibers glued into the grooves using Bicron 600 optical epoxy. There are 240 counters, 63.5 cm wide, and 207 cm – 287 cm long. The counters are positioned with their width along z and length along ϕ.

The cosmic bottom counters complete the scintillator coverage of the central toroidal magnet. There are 132 counters, of two different designs. The forty-eight counters located on the outside of the center bottom B layer of PDTs (where there is no C layer) are nearly identical to the cosmic cap counters described above. Some minor improvements were made in the placement of the edge fibers to increase the light yield and the counter frames are made from 0.32 cm steel bent into U-shaped channels. The counters are suspended from the B-layer PDTs.

$A\phi$ Scintillation Counters

The $A\phi$ scintillation counters cover the A-layer PDTs, those between the calorimeter and the toroid. They provide a fast detector for triggering on and identifying muons and for rejecting out-of-time backscatter from the forward direction. In-time scintillation counter hits are matched with tracks in the CFT in the Level 1 trigger (see section 3.10) for high-p_T single muon and low-p_T dimuon triggers. The counters also provide the time stamp for low-p_T muons which do not penetrate the toroid and thus do not reach the cosmic cap or bottom counters.

An end view of the $A\phi$ counter layout is shown in Fig. 3.13. The ϕ segmentation

is approximately 4.5° which matches the central fiber tracker trigger segmentation. The longitudinal segmentation is 84.5 cm which provides the necessary time resolution and a match to the size of the PDTs; there are nine counters along the detector in the z direction. The nearly constant segmentation in ϕ is accomplished through the use of three sizes of counter: 36.7 cm, 27.5 cm, and 23.09 cm wide. The widest counters are located at the corners of the detector, the narrowest at the center of each side. There is a gap at the bottom of the detector where the calorimeter support is located. The counters overlap an average of about 3% in ϕ to reduce the possibility of muons passing through cracks. Along the length of the detector, the counters are butted end-to-end with a small gap between each. There are a total of 630 $A\phi$ counters.

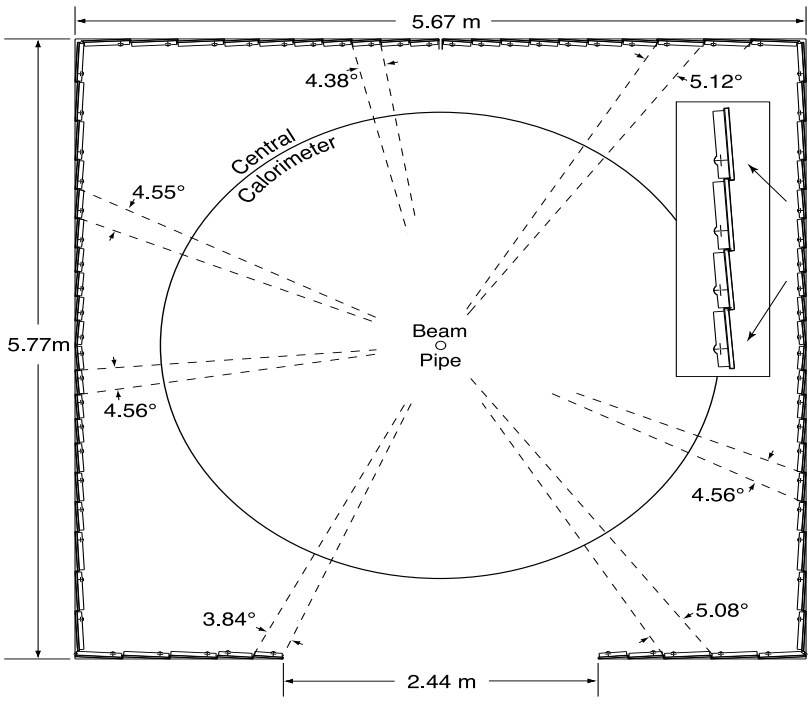

Figure 3.13: End view of the layout of the $A\phi$ scintillation counters. The inset box shows an enlarged view of four counters. Azimuthal coverage is shown for seven of the counters. The bump on each counter represents the photomultiplier tube attached to the counter case.

3.7.3 Forward Muon System

The layout of the forward muon system is shown in Fig. 3.2. It covers $1.0 \lesssim |\eta| \lesssim 2.0$ and consists of three major parts: three layers of MDTs for muon track reconstruction, three layers of scintillation counters for triggering on events with muons, and shielding around the beam pipe.

Mini Drift Tubes

Mini drift tubes were chosen for their short electron drift time (below 132 ns), good coordinate resolution (less than 1 mm), radiation hardness, high segmentation, and low occupancy. The MDTs are arranged in three layers (A, B, and C, with A closest to the interaction region inside the toroidal magnet and C furthest away), each of which is divided into eight octants, as illustrated in Fig. 3.10. A layer consists of three (layers B and C) or four (layer A) planes of tubes mounted along magnetic field lines (the field shape in the forward toroids is more "square" than "circular"). The entire MDT system contains 48,640 wires; the maximum tube length is 5830 mm in layer C. Since the flux of particles drops with increasing distance from the beam line, the occupancy of individual tubes is the same within a factor of two over an entire layer.

An MDT tube consists of eight cells, each with a 9.4×9.4 mm^2 internal cross section and a 50 μm W-Au anode wire in the center, see Fig. 3.14. The tubes are made from commercially available aluminum extrusion combs (0.6 mm thick) with a stainless steel foil cover (0.15 mm thick) and are inserted into PVC sleeves. They are closed by endcaps that provide accurate positioning of the anode wires, wire tension, gas tightness, and electrical and gas connections. The anode wires are supported by spacers; the unsupported wire length never exceeds 1 m.

The MDT system uses a CF_4-CH_4 (90%-10%) gas mixture. It is non-flammable, fast, exhibits no radiation aging, and has a wide operational plateau. The maximum drift time for tracks that are perpendicular to the detector plane is 40 ns; for tracks inclined at 45°,

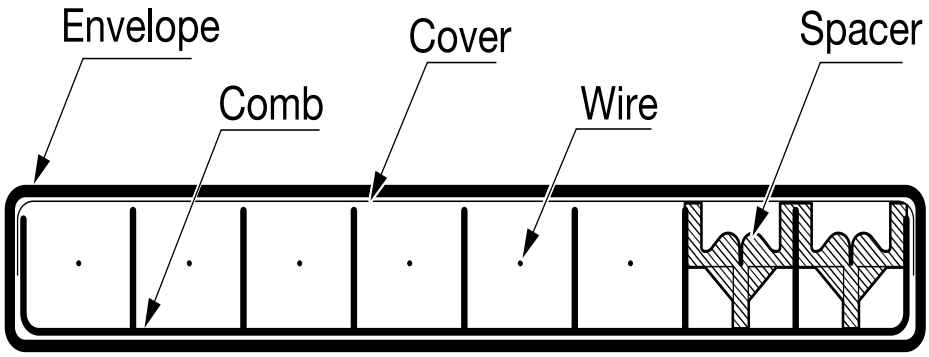

Figure 3.14: Cross-sectional view of a mini drift tube.

the maximum drift time is 60 ns.

Trigger Scintillation Counters

The muon trigger scintillation counters are mounted inside (layer A) and outside (layers B and C) of the toroidal magnet (see Fig. 3.2). Each layer is divided into octants containing about ninety-six counters. The ϕ segmentation is 4.5° and matches the CFT trigger sectors. The η segmentation is 0.12 (0.07) for the first nine inner (last three) rows of counters. The largest counters, outer counters in the C layer, are 60×110 cm^2. The B and C layers have geometries similar to that of the A layer, but limited in places by the collision hall ceiling and floor.

The design of the counter was optimized to provide good timing resolution and amplitude uniformity for background rejection, high muon detection efficiency, and reasonable cost for the production of nearly five thousand counters.

Shielding

Three sources contribute to non-muon background in the central and forward muon systems: *i*) scattered proton and antiproton fragments that interact with the end of the calorimeter or

with the beampipe, produce background in the central and forward A layer; *ii*) proton and antiproton fragments interacting with the Tevatron low-beta quadrupole magnets produce hits in the B and C layers of the forward muon system; and *iii*) beam halo interactions from the tunnel. Shielding installed in the accelerator tunnel during Run I [40] significantly reduced the background from beam halo. New shielding has been installed for Run II to reduce the background due to proton and antiproton remnants. Reduction in backgrounds along with the use of radiation-hard detectors, ensures long-term, reliable operation of the muon system.

The shielding consists of layers of iron, polyethylene, and lead in a steel structure surrounding the beam pipe and low-beta quadrupole magnets. Iron is used as the hadronic and electromagnetic absorber due to its relatively short interaction (16.8 cm) and radiation (1.76 cm) lengths and low cost. Polyethylene is a good absorber of neutrons due to its high hydrogen content. Lead is used to absorb gamma rays.

The position of the shielding is shown in Fig. 3.2. It extends from the end calorimeter cryostat, through the end toroid magnet, to the wall of the collision hall.

3.8 Forward Proton Detector

The forward proton detector (FPD) [41] measures protons and antiprotons scattered at small angles (on the order of 1 mrad) that do not impinge upon the main DØ detector. During Run I, such diffractive events were tagged using a rapidity gap (the absence of particles in a region of the detector). However a forward particle detector is necessary for access to the full kinematics of the scattered particle.

The FPD consists of a series of momentum spectrometers that make use of accelerator magnets in conjunction with position detectors along the beam line. The position detectors operate a few millimeters away from the beam and have to be moved out of the beamline during injection of protons or antiprotons into the accelerator. Special stainless steel containers, called Roman pots [42], house the position detectors, allowing them to function

outside the ultra-high vacuum of the accelerator, but close to the beam. The scattered p or $\bar{p}$ traverses a thin steel window at the entrance and exit of each pot. The pots are remotely controlled and can be moved close to the beam during stable conditions.

The Roman pots are housed in stainless steel chambers called castles. The FPD consists of eighteen Roman pots arranged in six castles. The castles are located at various distances from the DØ interaction point and in locations that do not interfere with the accelerator. The arrangement of the FPD is shown in Fig. 3.15. Four castles are located downstream of the low beta quadrupole magnets on each side of the collision point: two on the p side (P1 and P2) and two on the $\bar{p}$ side (A1 and A2). Each of these quadrupole castles contains four Roman pots arranged to cover most of the area around the beam. Two castles (D1 and D2) are located on the outgoing $\bar{p}$ side after the dipole magnet. Each of these dipole castles contains only one Roman pot. There are nine spectrometers: the two dipole castles form one, and on each side of the interaction region the two up, two down, two in, and two out pots are paired to form the other eight.

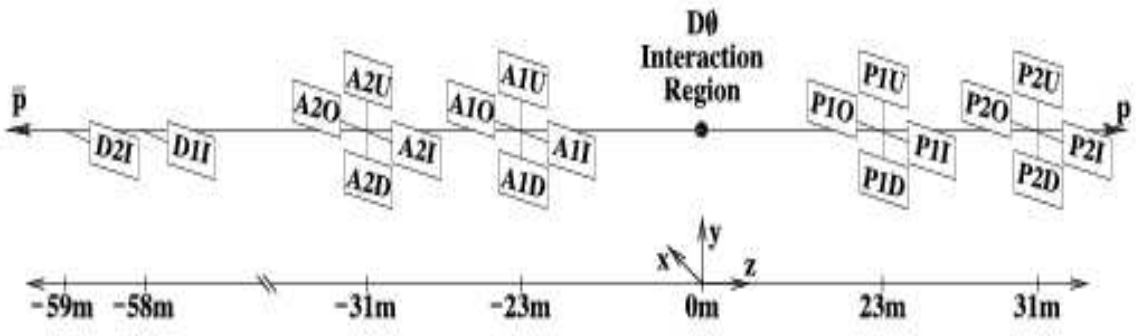

Figure 3.15: FPD layout. Quadrupole castles are designated with a leading P or A when placed on the p side or the $\bar{p}$ side, respectively; the number designates the station location; while the final letter indicates pot position (U for up, D down, I in, O out). D1I and D2I are dipole castles.

3.9 Luminosity Monitor

The primary purpose of the luminosity monitor (LM) is to determine the Tevatron luminosity at the DØ interaction region. This is accomplished by detecting inelastic $p\overline{p}$ collisions with a dedicated detector. The LM also serves to measure beam halo rates and to make a fast measurement of the z coordinate of the interaction vertex.

The LM detector consists of two arrays of twenty-four plastic scintillation counters with PMT readout located at $z = \pm 140$ cm, as shown in Fig. 3.16. A schematic drawing of an array of detectors is shown in Fig. 3.17. The arrays are located in front of the end calorimeters and occupy the radial region between the beam pipe and the forward preshower detector. The counters are 15 cm long and cover the pseudorapidity range $2.7 < |\eta| < 4.4$.

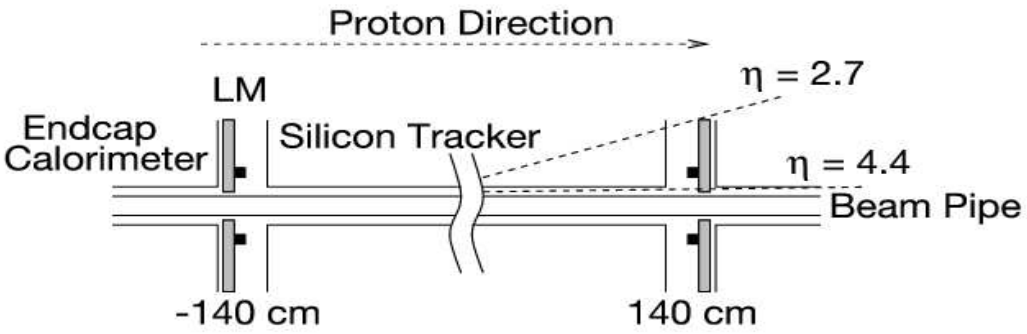

Figure 3.16: Schematic drawing showing the location of the LM detectors.

The luminosity $\mathcal{L}$ is determined from the average number of inelastic collisions per beam crossing $\bar{N}_{LM}$ measured by the LM: $\mathcal{L} = \frac{f\bar{N}_{LM}}{\sigma_{LM}}$ where f is the beam crossing frequency and σ_{LM} is the effective cross section for the LM that takes into account the acceptance and efficiency of the LM detector [43]. Since $\bar{N}_{LM}$ is typically greater than one, it is important to account for multiple $p\overline{p}$ collisions in a single beam crossing. This is done by counting the fraction of beam crossings with no collisions and using Poisson statistics to determine $\bar{N}_{LM}$.

To accurately measure the luminosity, it is necessary to distinguish $p\overline{p}$ interactions from

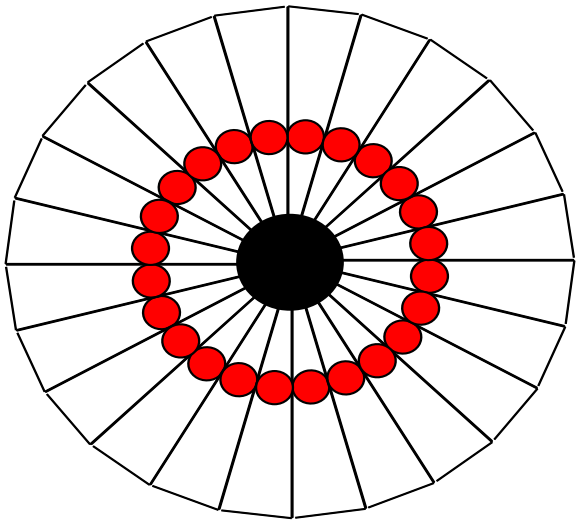

Figure 3.17: Schematic drawing showing the geometry of the LM counters and the locations of the PMTs (solid dots).

the beam halo backgrounds. We separate these processes by making precise time-of-flight measurements of particles traveling at small angles with respect to the beams. We first assume that particles hitting the LM detector originate from a $p\overline{p}$ interaction and estimate the z coordinate of the interaction vertex z_v from the difference in time-of-flight: $z_v = \frac{c}{2}(t_- - t_+)$ where t_+ and t_- are the times-of-flight measured for particles hitting the LM detectors placed at ± 140 cm. Beam-beam collisions are selected by requiring $|z_v| < 100$ cm, which encompasses nearly all $p\overline{p}$ collisions produced by the Tevatron ($\sigma_z \approx 30$ cm). Beam halo particles traveling in the $\pm\hat{z}$ direction will have $z_v \approx \mp 140$ cm, and are eliminated by the $|z_v| < 100$ cm requirement.

3.10 Trigger System

With the increased luminosity and higher interaction rate delivered by the upgraded Tevatron, a significantly enhanced trigger is necessary to select the interesting physics events to be recorded. Three distinct levels form this new trigger system with each succeeding level

examining fewer events but in greater detail and with more complexity. The first stage (Level 1 or L1) comprises a collection of hardware trigger elements that provide a trigger accept rate of about 2 kHz. In the second stage (Level 2 or L2), hardware engines and embedded microprocessors associated with specific subdetectors provide information to a global processor to construct a trigger decision based on individual objects as well as object correlations. The L2 system reduces the trigger rate by a factor of about two and has an accept rate of approximately 1 kHz. Candidates passed by L1 and L2 are sent to a farm of Level 3 (L3) microprocessors; sophisticated algorithms reduce the rate to about 50 Hz and these events are recorded for offline reconstruction of events. An overview of the DØ trigger and data acquisition system is shown in Fig. 3.18. A block diagram of the L1 and L2 trigger systems is shown in Fig. 3.19.

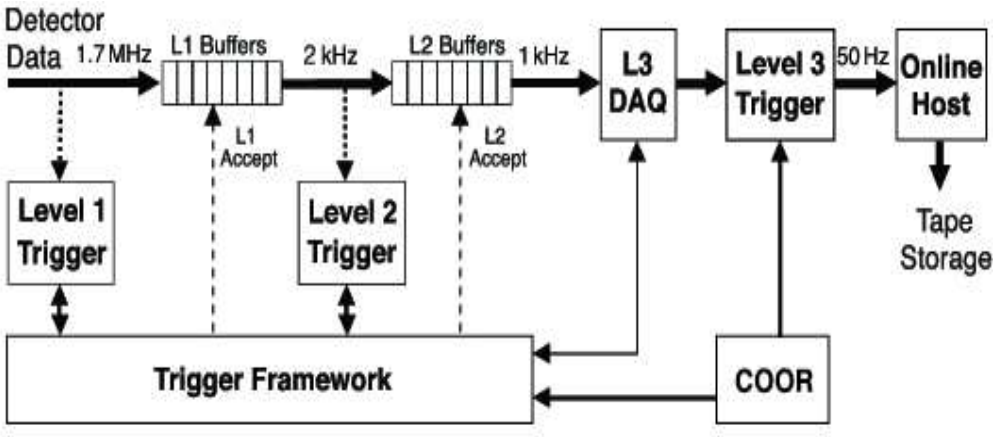

Figure 3.18: Overview of the DØ trigger and data acquisition systems.

The trigger system is closely integrated with the read out of data, as illustrated in Fig. 3.18. Each event that satisfies the successive L1 and L2 triggers is fully digitized, and all of the data blocks for the event are transferred to a single commodity processor in the L3 farm. The L1 and L2 buffers play an important role in minimizing the experiment's deadtime by providing FIFO storage to hold event data awaiting a Level 2 decision or awaiting transfer to Level 3.

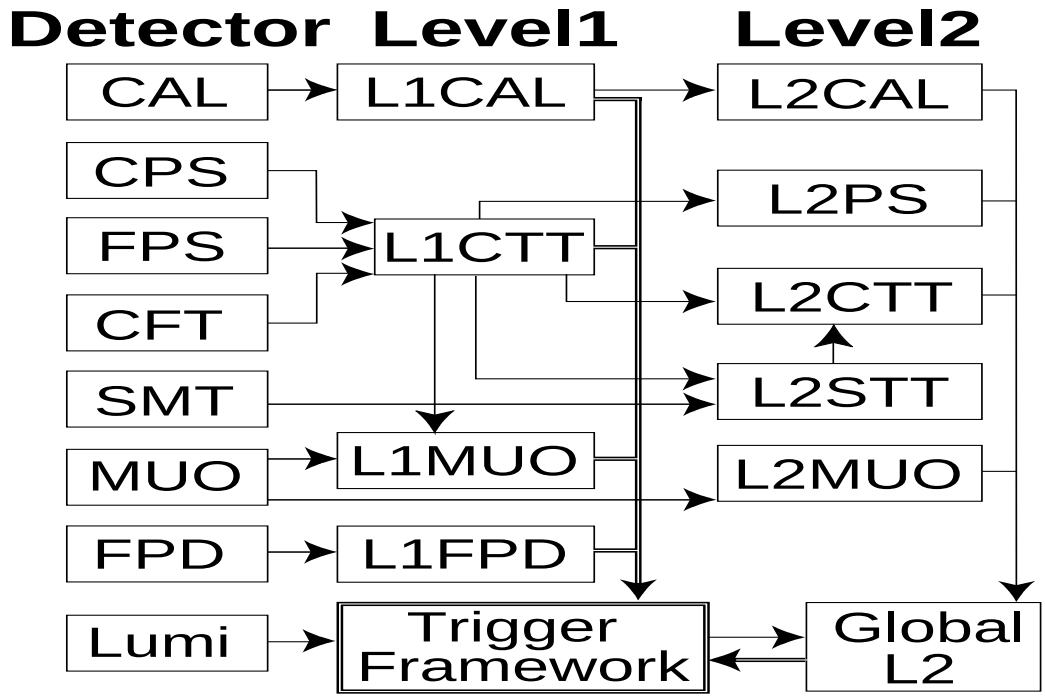

Figure 3.19: Block diagram of the DØ L1 and L2 trigger systems. The arrows show the flow of trigger-related data.

3.10.1 The Level 1 Trigger

L1 is implemented in specialized hardware and examines every event for interesting features. The calorimeter trigger (L1Cal) looks for energy deposition patterns exceeding programmed limits on transverse energy deposits; the central track trigger (L1CTT) and the muon system trigger (L1Muon) compare tracks, separately and together, to see if they exceed preset thresholds in transverse momentum. The L1 forward proton detector trigger (L1FPD) is used to select diffractively-produced events by triggering on protons or antiprotons scattered at very small angles.

All events awaiting L1 trigger decisions are pipelined and thus make minimal contributions to the deadtime. In order to participate in the trigger decision, the L1 trigger decision must arrive at the trigger framework in 3.5 μs or less. The acceptance rate of L1 trigger is

limited by the maximum readout rates of the participating subsystems and by a desire to minimize the deadtime associated with the readout.

The trigger framework (TFW) gathers digital information from each of the specific L1 trigger devices and chooses whether a particular event is to be accepted for further examination. In addition, it coordinates various vetoes that can inhibit triggers, provides the prescaling of triggers too copious to pass on without rate reduction, correlates the trigger and readout functions, manages the communication tasks with the front-end electronics and the trigger control computer (TCC), and provides a large number of scalers that allow accounting of trigger rates and deadtimes.

3.10.2 The Level 2 Trigger

The L2 trigger provides detector-specific preprocessing engines and a global stage (L2Global) to test for correlations in physics signatures across detector subsystems. The L2 trigger system was designed to handle input rates of up to 10 kHz with a maximum accept rate of 1 kHz. L2 preprocessors collect data from the front-ends and L1 trigger system and analyze these data to form physics objects. L2 can also combine data across detectors to form higher quality physics objects and examine event-wide correlations in all L2 physics objects. The L2Global processor selects events based on the set of 128 selections applied at L1 and additional script-controlled criteria. Events passing L2 are tagged for full readout and further analysis in the L3 trigger.

3.10.3 The Level 3 Trigger

The L3 trigger provides additional rejection both to enrich the physics samples and to maintain an acceptable throughput which can be recorded to tape. A high level, fully programmable software trigger, L3 performs a limited reconstruction of events, reducing a nominal 1 kHz input rate to 50 Hz for data recorded for offline analysis. Its decisions are based on complete physics objects as well as on the relationships between such objects

(such as the rapidity or azimuthal angle separating physics objects or their invariant mass). Candidate physics objects, or relations between them, are generated by object-specific software algorithms (filter tools). Tools perform the bulk of the work: unpacking raw data, locating hits, forming clusters, applying calibration, and reconstructing photons, electrons, muons, taus, jets, vertices, and $\not\!\!E_T$. Reference sets (refsets) of programmable algorithm parameters are input to the tools via the programmable trigger list. The refsets define the physics objects precisely (jet refsets specify cone size, for example, and electron refsets, the electromagnetic fraction, among other characteristics) for each invocation of the filter tool. All tools cache their results to expedite possible multiple calls within the same event, and if the event is accepted, add L3 object parameters to the data block.

3.11 Data Acquisition System

The data acquisition system (L3DAQ) transports detector component data from the VME readout crates to the processing nodes of the L3 trigger filtering farm. The online host receives event data from the L3 farm nodes for distribution to logging and monitoring tasks. Overall coordination and control of triggering and data acquisition is handled by the COOR program running on the online host system.

The L3DAQ system's designed bandwidth is 250 MB/s, corresponding to an average event size of about 200 kB at an L2 trigger accept rate of 1 kHz. A schematic diagram of the communication and data flow in the system is shown in Fig. 3.20. All nodes in the system are based on commodity computers (SBCs) and run the Linux operating system. TCP/IP sockets implemented via the ACE [45] C++ network and utility library are used for all communication and data transfers.

The supervisor process provides the interface between the main DØ run control program (COOR) and the L3DAQ system. When a new run is configured, the supervisor passes run and general trigger information to the RM and passes the COOR-provided L3 filter configuration to the EVB process on relevant farm nodes, where it is cached and passed on

to the L3 filter processes.

The final repository for the raw event data is a tape, maintained in a robotic tape system located about 3 km from the detector. Data must be transmitted to each tape drive at approximately 10 MB/s to keep the drive operating in streaming mode, since the remote tape drive nodes have no intermediate disk buffer. The online system is capable of simultaneous output to multiple tape streams and of buffering in case of tape robot unavailability. In addition to logging data, the online host system must supply between ten and twenty data monitoring clients at anywhere from 1% to 100% of the full data rate.

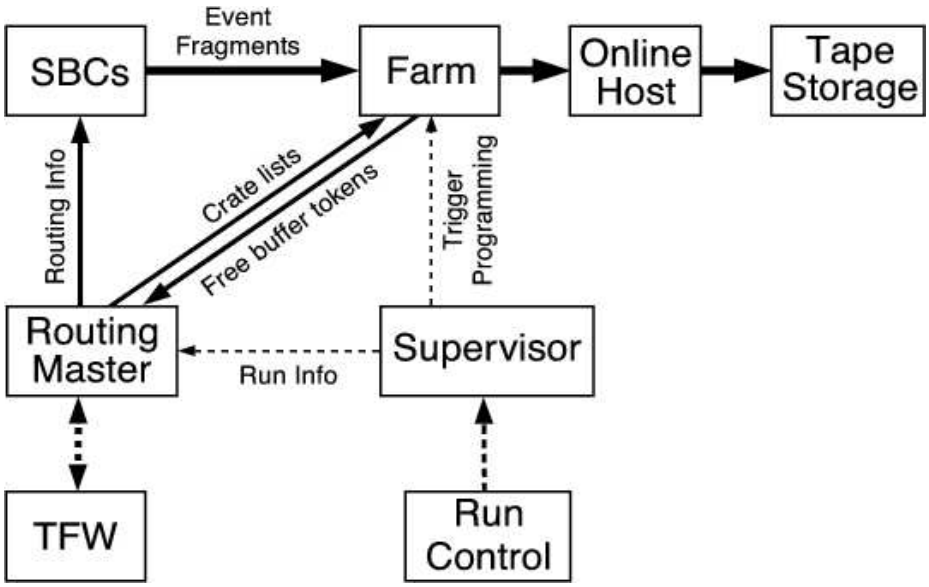

Figure 3.20: Schematic illustration of the information and data flow through the L3DAQ system.

Chapter 4

DØ Software and Tools

This chapter begins with brief introduction of raw data, followed by Monte Carlo simulation method of event generation and detector simulation whose output is equivalent to the raw data. From raw data, physics objects are reconstructed for the data analysis. A brief description of the track reconstruction, vertex reconstruction and muon reconstruction, relevant for this analysis, are given under event reconstruction algorithm.

4.1 Raw Data

The uncalibrated data read out directly from the various parts of the detector are called raw data. These basically consist of channel addresses and associated signal information. In a raw data event, information is stored in a structured form, from various part of the detector known as raw information (e.g. RawSiliconVertex). Structure wise, raw data has various modules, each consists of array of channels. A channel is the smallest unit of various detector electronics (e.g. silicon microstrip, muon drift wire) at readout time, whose format depends on the type of detector.

For data analysis, a physics event should have meaningful physics objects. In order to get physics objects from raw data, it is processed though reconstruction algorithms. Before reconstruction of raw data, it is uncompressed and normalized using calibration constants from each sub detector. Various elements in a typical physics event are shown in figure 4.1.

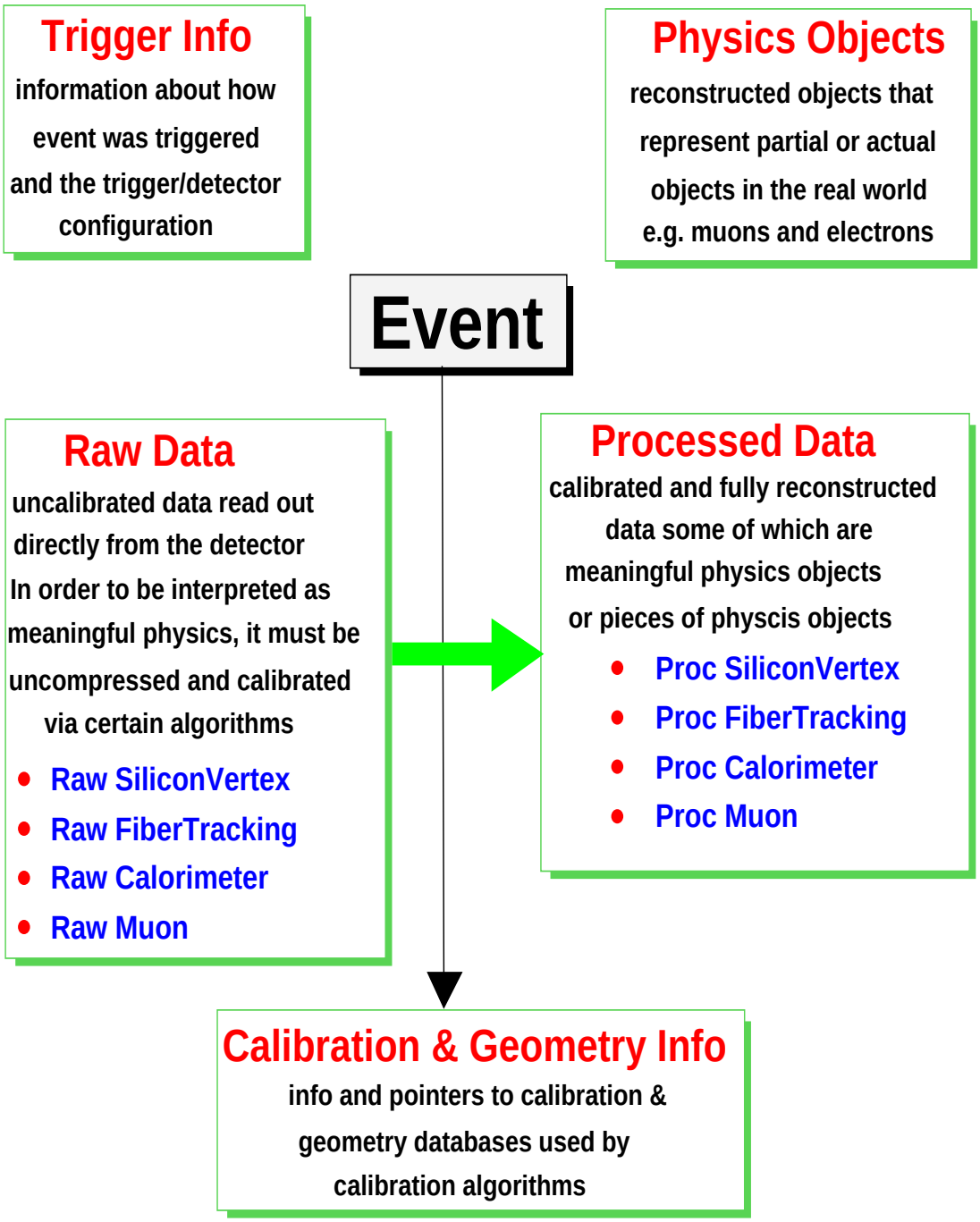

Figure 4.1: Elements of a physics event.

4.2 Monte Carlo Simulation

Monte Carlo (MC) simulation method, a widely employed simulation technique for imitating real life system, is an essential tool to understand physics process and detector response in high energy physics experiments. To simulate the whole procedure of a physical process such as a B meson decay, and the detector response, DØ has developed a package called mc_runjob [46]. The package is capable of handling full event simulation, from the event generation to the event reconstruction, in one cycle. At DØ, we have a wide range of MC event generators for different physics processes. A combination of two or more event generators may also be used as per requirement, for example to generate B_s^0 meson events with a specific transversity distribution (such as pure CP-even state), two event generators `PYTHIA [47]` and `EvtGen [48]` are used. Although `PYTHIA` is the commonly used event generator, other event generators are also used for some specific physics process, for example `ALPGEN` [49] is used for exact LO matrix elements.

For generating large samples of MC events, special Central Processing Unit (CPU) clusters known as MC farms [50] are used. These MC farm centers are located at various places in the world and contribute to the DØ Remote Analysis Coordination Effort Group [51]. The process of MC event generation with a full chain of detector simulation and event reconstruction is relatively very fast, because of a very big number of dedicated CPU's working at the same-time.

4.2.1 Event Generation

Event generators are employed for simulating final state of collision particles in high energy physics experiments. Some of the popular generators such as `PYTHIA`, `ISAJET [52]` etc. are used to simulate $p\bar{p}$ interaction. In an event generator program, basic theoretical models, which describe the known physics process are implemented. Before using an event generator, many parameters need to be tuned carefully according to available experimental results. The output of an event generator is usually a file containing a list of particles with their

four-momenta and the primary and decay vertex positions.

There are some physical process where one event generator is not adequate enough to simulate entire process accurately. For example decay of B-hadrons cannot be simulated completely using `PYTHIA`. In such cases either one needs to develop and maintain new event generator for a desired physical process or one can combine two or more event generators to simulate desired physics process. `QQ` [53] and `EvtGen`, are two mostly used event generators for production and decay of B-hadrons, which were developed and maintained by CLEO and BaBar collaborations respectively. DØ physics group has used `PYTHIA` for production of B-hadrons in $p\overline{p}$ collision, and `EvtGen` for its decay to final state particles.

Main features of `PYTHIA` event generator are given below:

- Events are generated according to the multiple interactions model from hard scattering of $p\overline{p}$ interactions.
- Quantum chromodynamics radiative corrections corresponding to both the initial state radiation (ISR) and final state radiation (FSR), are included. Initial state showers is interleaved in one single sequence of falling transverse momentum.
- Because gluons have self-coupling field lines, which behave like flux tubes, this finally leads to independent fragmentation of gluons and quarks into hadrons. This process is also known as fragmentation or hadronization. Different event generators use different empirical schemes for hadronization, for example, `PYTHIA` uses LUND string fragmentation scheme [54] while `HERWIG` uses CLUSTER fragmentation scheme [55].
- The final step is to evolve and hadronize the leftover partons known as "spectators", again `PYTHIA` uses an extension of the LUND Color Scheme [54].

Inelastic $p-\overline{p}$ collisions are dominated by soft (low$-p_T$) interactions with an occasional hard scattering. The underlying events (UE) are usually defined to be everything except the two outgoing hard scattered jets, including multiple-parton interactions, ISR and FSR,

as shown in Fig. 4.2. At DØ to model UE, we are using CDF tuned PDF library function "CTEQ5L", which agrees with LO prediction. Multiple interaction model is used for partonic remnants confinement process.

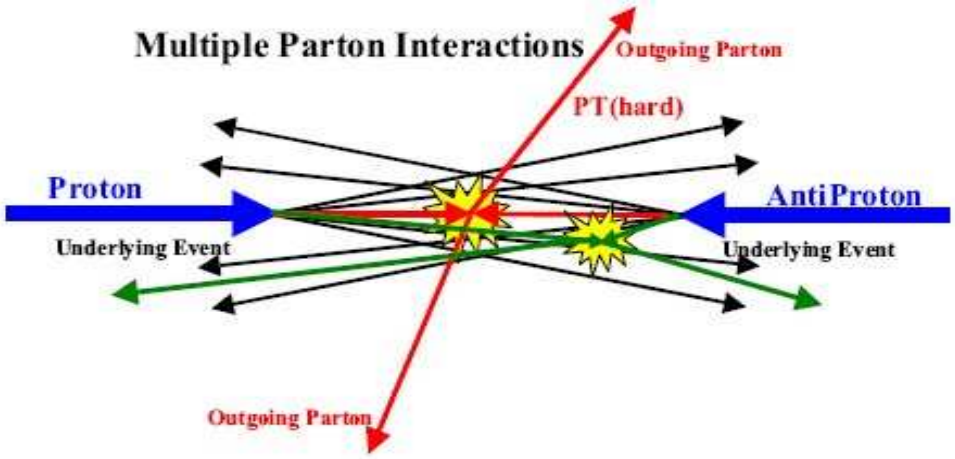

Figure 4.2: Illustration of the way PYTHIA models the UE in $p - \overline{p}$ collision by including multiple parton interactions.

4.2.2 Detector Simulation

Simulation of detector response to the particles produced at the event generator level is known as detector simulation. After production and decay of short lived particles for desired physical process, one needs to understand how final state particles travel though the detector. This is a complicated and time consuming process.

Almost all high energy physics experiments simulates the response of the detector to these particles using `GEANT` [56] program from CERN. Detector geometry, chemical and physical properties of the active and passive components are defined under `GEANT` framework. Theoretical knowledge of the interactions of particles with materials is also built into the program. It starts with tracks of particles from the event generator output and propagates them through the detector, by simulating effect of particle interaction with the

detector material. If a particle interacts in the detector material to produce new particles, those secondary particles are also propagated through the detector. While particles are propagating, the energy lost into the active part of the detector is stored into the buffer which is used for digitization in next step.

For the Tevatron RunII, the MC simulation of the DØ RunII detector is based upon `GEANT 3.21` and called, "DØ Geant Simulation of the Total Apparatus Response(`DØGSTAR`) [57]". `GEANT 3.21` is a FORTRAN based program but `DØGSTAR` has C++ wrappers, to allow it to run in the DØ RunII software environment. `DØGSTAR` models the entire DØ RunII detector including the silicon vertex detector, central fiber tracker, preshower detector, calorimeter and muon system. `DØGSTAR` has been tested for known physics and many upgrade, such as addition of cable etc. have been made time to time. The output of `DØGSTAR` simulation is a file containing pulse heights and time information if signals from all detector cells.

The digitization of the `DØGSTAR` output of each detector cell at DØ is done using a program `DØSim` [58]. Its output looks like real raw data. `DØSim` generates a file suitable as input for the event reconstruction package, and can also be used for trigger simulation programs. Low p_T parton scattering (approx. $p_T < 2GeV$) are the dominant process, known as "minimum bias" (minbias) process. These events consist only of beam jets. At high energy the jet cross sections become large, and to represent the total cross section a sample of minbias events is added at this stage of simulation. During `DØSim` run following main functions are performed:

- Merge hard scatter and minbias events.
- Add calorimeter pileup from previous events.
- Make L1CalTTowerChunk for L1 simulation.
- Add SMT, CFT, calorimeter and muon noise and inefficiencies.

4.3 Event Reconstruction

The output of the DØSim program and event recorded by the DØ detector in raw data format, consists of signals from various detector elements, such as digital signal from calorimeter, hits in the central tracking system, drift time from muon system etc. For physics analysis, one needs physics objects such as muons, electrons, photons, jets etc. High level algorithms written in C++ are used to convert the raw data format into physics objects, and assembled in what is known as "DØReco" [59].

The DØReco program reads raw data as input, and decodes the detector hits, fits track trajectories, and uses the particle identification algorithms to create the particle objects of the event (for example candidate may be a electron or a muon etc.). The output of DØReco can be written in various data formats but at DØ mostly it is written in "thumbnail" [60] format, having packed content of object informations.

The DØReco event reconstruction program based on following major steps:

- Decoding Hit information: The digitized signals from the tracking detectors are converted into spatial locations of hits, while signals from calorimeter cells are converted to energy deposits.
- Tracking and Clustering: The tracking hits are combined together to form tracks. The calorimeter energy depositions in the cells are grouped to form clusters.
- Vertexing: The location of the $p\bar{p}$ interaction is calculated and used in the calculation of various kinematic quantities. The vertices are essential for particle identification.
- Particle identification: The tracking and calorimeter information is combined to form candidates for muons, electrons, photons, etc.

Out of various reconstruction programs and particle identification, the track reconstruction, the muon identification and the vertex reconstruction are the most relevant for this

analysis. These are discussed in brief in the following sections.

4.3.1 Track Reconstruction

The reconstruction of particle tracks is a first step in the event reconstruction. The trajectory of all charged particles are reconstructed from the energy they deposit in the tracking detector i.e. in the silicon and fiber tracker detectors. At DØ, track reconstruction is done using `GTR` [61] algorithm, which takes the hit information from the different layers of the central tracking system and uses a Kalman Filter [62] and Smoother fitter. Input to the tracking algorithm is in the form of so called clusters, the signal position measurement and its error. Using two related steps of track finding and fitting, track reconstruction is performed. The basic `GTR` components needed to carry out the track finding are described below.

- `Surfaces:` During the first step, `GTR` builds a model of the tracking detector as a collection of layers made of bounded abstract surfaces. The specific types of surfaces are needed to describe the DØ detector such as the cylindrical surface for the fiber tracker and $x-y$ and z planes for the SMT. Each cluster is associated with a surface in a layer. A track is made of a list of clusters and a kinematic fit of five parameters (two for the position on the surface, two corresponding to the direction, and one describing the track curvature) and an error matrix for these parameters. The first few surfaces are used to build a 'seed' track with approximate parameters and errors.

- `Paths:` The paths are an ordered list of the surfaces that a particle coming from a $p\overline{p}$ collision would cross. Paths are used for searching for good tracks with specified path maps and rejecting bad tracks based on fixed conditions such as number of missed surfaces.

- `Propagators:` Propagators are used for track fitting, that is, to extrapolate the seed tracks between the remaining surfaces. A track propagator solves the equation

of motion for a track, including the effect of magnetic fields. The propagator also updates the track errors for the effects of multiple scattering and energy lost in any material crossed while reaching the target surface.

- `Fitters:` For known track parameters and errors at a given surface, *fitters* attempt to add a new cluster to the track using Kalman Filter algorithm. The fitter combines the track and cluster errors into a match χ^2 and reject the cluster if the χ^2 is higher than specific value otherwise the cluster is added to the track, followed by update of track parameters and errors.

- `Filters:` When the track density is high, filters are applied to clean the list of candidate tracks. These filters reject tracks based on the overall χ^2 of their fit and the number of missed surfaces. Tracks are also rejected if they share some specified number of clusters, among these tracks one track is kept based on the χ^2 fit.

The `GTR` track finding algorithm has four different paths, for four different angular regions at DØ. These four regions are central region, overlap region, gap and forward region. The central region is covered by SMT and CFT, overlap by axial and stereo fiber edge of the CFT, gap with no CFT information and forward by silicon barrels and H-Disks. The output of the `GTR` algorithm is a list of reconstructed track helices, parametrized at the distance of closest approach to the origin (DCA). Each track is described by following five parameters:

1. q/p_T: charge q is either +1 or -1, p_T (=p sinθ) is the transverse momentum of the particle. θ is given by $cos^{-1}(dz/ds)$, where s is the path length along the helix, increasing when moving in the particle direction.

2. *dca*: distance of closest approach in transverse plane as shown in Fig. 4.3. The sign of *dca* is given by the vector product $\vec{dca}$ X $\vec{p_T}$.

3. *zca*: z at dca.

4. ϕ: angle between transverse momentum direction of the particle and x-axis, known as azimuthal angle at DCA.

5. tanλ: known as dip angle, measures the slope of the helix, where $\lambda + \theta = \pi/2$.

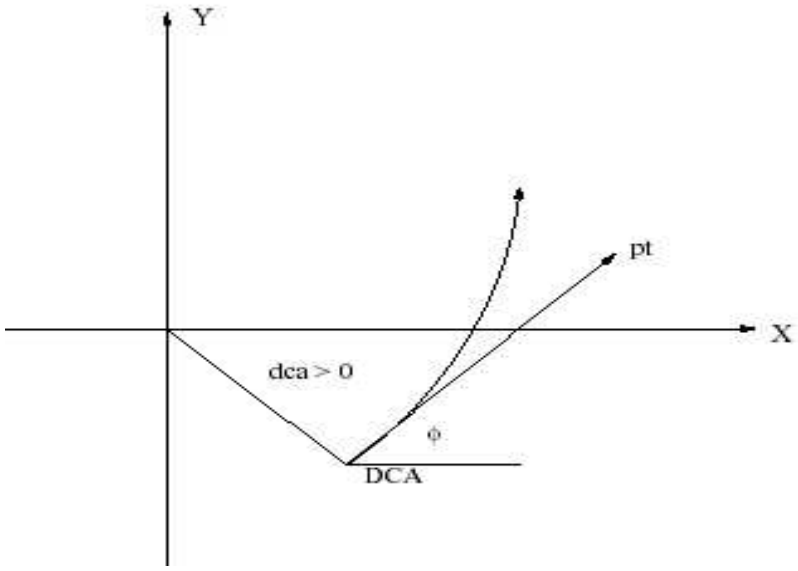

Figure 4.3: Track parameters in transverse plane

4.3.2 Muon Reconstruction

The DØ muon spectrometer is divided in two main regions, central region ($|\eta| \leq 1$) and forward region ($1 \leq |\eta| \leq 2$). Each region has three layers (usually called A, B and C layer, from interaction point to outside). After reading out the primary muon information (such as wire hits, drift time etc. from various segments of muon spectrometer) in the form of electronic signal, offline muon identification has the following main steps:

- **Muon Hit Reconstruction:** The reconstruction of muon tracks starts with conversion of the drift time, wire hit etc. to the individual muon hits. Based on the muon system hardware, three types of muon hit reconstructions are performed. In

the central region, proportional drift tubes (PDTs) hit reconstruction, using PDTs drift time measurement is carried out. In the forward region, from mini drift tubes (MDTs) drift time (assuming hit in the MDT has occurred at the middle of the wire), MDT hit reconstruction is done. In both central and Forward region, using scintillator time information, MSC hit reconstruction is done.

- **Muon Segment Reconstruction:** After the individual hits are found, straight lines (track segments) are reconstructed in each layer of the local muon system by fitting groups of hits. The straight line fit is done separately for A-layer (4 planes of tubes) and B, C-layers (3 planes of tubes) before and after the toroid magnet.

- **Local Muon Track Reconstruction:** The track segments reconstructed in the A-layer are matched with track segments in the B and C layers in search for muon track. For muon track finding, a fitting algorithm is used which takes into account the toroidal magnetic field, energy loss in the toroid and multiple Coulomb scattering during propagation of the muon track. The estimate of the muon track momentum is done from the measurement of the bend of the muon track while passing through the toroid magnet.

- **Muon Central Track Match:** At this stage, local muon tracks are matched with tracks of central tracking system. The matching is done using the error matrix propagation, which takes into account the magnetic field (both solenoid and toroid), multiple Coulomb scattering and the energy loss in the solenoid, toroid and calorimeter. If the algorithm finds a match, the two tracks and two error matrices are combined to obtain the final track parameters.

- **Offline Muon Reconstruction:** In the offline muon reconstruction, the results of the object reconstructed in the muon system are combined in various ways with the information provided by the central tracking system and the calorimeter, to define a muon object suitable for physics analysis. The status of match is reflected by the value given to a variable. For simplicity standard quality criteria for “tight”, “medium” and

"loose" muons are also defined based on different local muon conditions and matching with central tracking system.

4.3.3 Vertex Reconstruction

The vertices of an event are the essential elements of the space-time signature of an interaction. Vertex reconstruction[1] must be of high precision for correct measurement of physical quantities of interest. All vertices in an interaction are either the space-time locations of primary interaction (source of all primary particles in an event) or space-time locations where an unstable particle has decayed. These space-time locations are also known as primary and secondary vertices in an event. At Tevatron, along with the "hard scatter" primary vertex and displaced secondary vertices (due to decay of unstable long lived particles), additional "minimum bias" interaction vertices are also expected.

A vertex algorithm must be able to reconstruct the hard scatter primary vertex and displaced vertices in an event with enough accuracy and without any bias, so that physical quantities based on space-time location of these vertices can be measured accurately. The vertex reconstruction algorithm works by an iterative procedure, building a vertex around a point known as *vertex seed*. Around vertex seed, tracks are added to and narrow down the allowed space overlapped by candidate tracks (as shown in Fig. 4.4) to converge into a vertex. Off vertex tracks are rejected if they increase the vertex size or the overlap area. The starting point or the vertex seed is very important to reconstruct a hard scatter primary vertex, beam spot position (i.e. hard scatter interaction point) determined with other methods, is used as a vertex seed.

Primary Vertex The accurate location of the primary vertex of an event is essential for the measurement of physical quantities specially related with lifetime of unstable particles. For the primary vertex determination, a pattern recognition (or vertex finding) algorithm is used based on an iterative process, to identify the tracks coming from a vertex (primary vertex), as prior knowledge of tracks (whether they belong to primary vertex or

[1]For detail of vertex reconstruction algorithms, see [63]

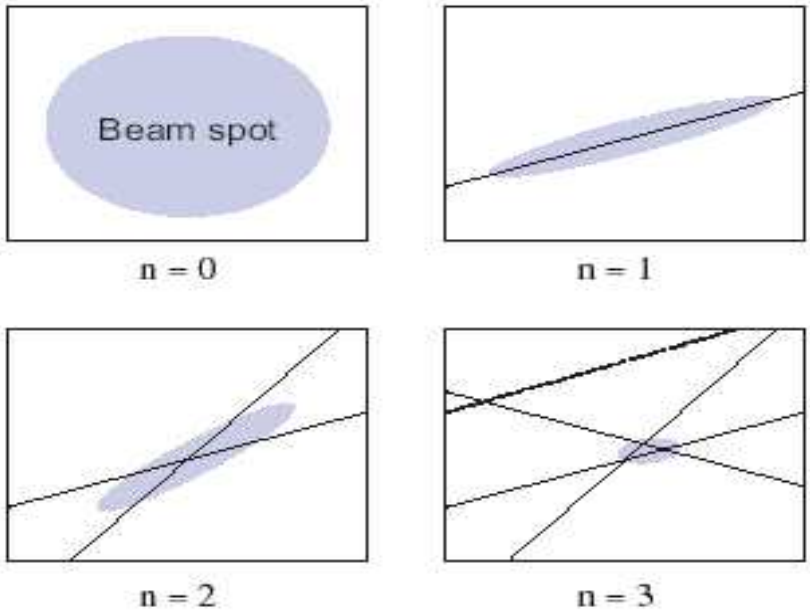

Figure 4.4: Vertex reconstruction steps, where n is the number of tracks in each step. Shaded area is allowed space, while dashed line is off-vertex track.

not) is not available. Since most of the particles produced in an interaction come from the primary vertex, the algorithm used to find these vertices is based on a "tear-down" approach.

The primary vertex reconstruction consist following steps:

1. **Track clustering:** tracks are clustered along the z axis, and looped in descendant order of track p_T. Tracks are added to the pre-cluster if Δz is less then few $centimeters$ (where Δz is the difference between the z of closest approach of the track, and the pre-cluster z average position). The Δz value should be small enough to resolve multiple interactions, and at the same time, big enough to be able to cluster all tracks from each interaction taking into account track resolution, the typical value is 2 cm.

2. **Track selection:** Quality cuts are applied to every track in the track-cluster in order to remove fake and badly reconstructed tracks. Tracks are required to be within

few standard deviations of the distance of closest approach (e.g. $|dca/\sigma(dca)| < 3$), while at least few hits in the SMT detector (e.g. $N_{smt} \geq 2$) and p_T of each track must be greater than some reasonable value (e.g. $p_T > 0.5\,GeV/c$).

3. **Vertex finding and fitting:** If we assume that a track-cluster has N selected tracks and $N_{trk} > 1$, the tear-down vertex search algorithm proceeds as follows:

   - All selected tracks are fitted to a common vertex and the total χ^2 of the fit is computed, $\chi^2(N_{trk})$.
   - Each track is excluded separately from the fit and a new $\chi^2(N_{trk}-1)$ is computed.
   - The track which gives the maximum difference $\chi^2(N_{trk})-\chi^2(N_{trk}-1)$ is removed from the vertex, if the total vertex χ^2 per degree of freedom exceeds a threshold of 10.
   - This procedure is repeated until the total vertex χ^2 per degree of freedom is smaller than some reasonable value (for this analysis it is 10, motivated by MC study).

   The final list of vertices found will contain the primary (hard scatter) vertex, and additional minimum bias interactions.

4. **Hard scatter vertex selection:** The event sample we used for this analysis is di-muon sample. Among all the primary vertex candidates the difference between hard scatter vertex z position and p_T-weighted average z position of the di-muon object (mostly J/ψs) should be less than few cm (for this analysis we choose this value to be 5 cm, motivated by MC study)

Secondary Vertex Secondary vertices in an event are due to the decay of long lived hadrons, for such secondary vertices associated tracks are not attached to the primary or minimum bias vertices. The purpose of secondary vertex reconstruction is to identify the decay of a long lived particle (e.g. B hadron) from the signature of several tracks emanating from a common point displaced from the primary interaction.

While reconstructing the secondary vertex, there are difficulties, because of much less tracks associated with secondary vertex compared to primary vertex and the initial vertex point (vertex seed) is not known. Due to these difficulties it is important to find an efficient algorithm for reconstructing secondary vertex. There are many approaches to find secondary vertices, but physics-motivated approaches and most useful for this analysis are given below:

- ***V0* vertex reconstruction:** The reconstruction of *V0* secondary vertices starts by fitting all pair of opposite charged tracks (from the given track cluster) in the event. *V0* algorithm search for vertices combining the simple build-up technique with a requirement of a given physics content or topology of the vertices. For e.g. in $J/\psi \rightarrow \mu^+\mu^-$ search, both tracks are assumed to be charged muons. These mass assignments are used in the calculation of the vertex invariant mass. The additional physics requirements can be added such as quality of the vertex fit etc.

- ***VertexGlobalFitter* vertex reconstruction:** To reconstruct a secondary vertex from set of tracks (usually more than 2), this approach is used. The input is a list of GTracks and the output is an object of the class vertex containing the position of the vertex and the re-fitted vertex-constrained tracks. The fit consists of the minimization of a χ^2 of following two terms:

  1. The spacial distance between the tracks and the reconstructed vertex.
  2. The distance between the reconstructed track momentum and the propagated track momentum at the vertex.

  The main advantage of this approach is to find a vertex which has three (or more) tracks coming out of it, and it works for both charged tracks and vertices.

In both approaches, the procedure is similar to the primary vertex reconstruction algorithm: it starts from a vertex seed and uses the "tear-down" approach based on Kalman Filter iterative method.

Chapter 5

Data Analysis

This chapter begins with a brief description of the data sample used in this analysis, followed by details of 'event reconstruction' and 'final event selection'. The next two sections describe the fit variables, fitting procedure, and the fit results. We next discuss the sources and the estimate of systematic uncertainties, and different verification of the entire procedure, including an ensemble test.

5.1 Data and Monte Carlo Event Samples

The $p\overline{p}$ interaction events at DØ detector are recorded on tapes in the thumbnail format [60] which are transfered to Sequential data Access via Meta-data (SAM [64]), for permanent storage. The total data size is so huge that it would be difficult and inconvenient to run the B-meson reconstruction program on the entire data. This calls for an event selector which has to be efficient, and must not bias the measurement of the physical quantities. The Monte Carlo data samples are also stored at the SAM in the thumbnail format.

5.1.1 Di muon Data Sample

Our aim is to reconstruct the B_s^0 (or B_d^0) events from the $B_s^0 \to J/\psi(\to \mu^+\mu^-)\phi(\to K^+K^-)$ decay mode (or $B_d^0 \to J/\psi(\to \mu^+\mu^-)K^*(\to K^\pm\pi^\mp)$). Since we have two opposite-sign

muons in the final state, we first select the di-muon events from entire reconstructed data. Selection criteria are kept very loose to ensure good efficiency without biasing the physical measurements. In technical terms used at DØ, we use 'Rounds 1-8 of the di-muon Common Sample [65]', which corresponds to the data recorded between June 2002 to August 2004. The data sample contains two reconstructed muons having a transverse momentum of each muon greater than 1.5 GeV. Muons are required to be detected as a track segment in at least one layer of the muon system and matched to a central track. One muon is required to have segments both inside and outside the toroid. We reject the events where muon data or central tracking data are corrupt. An event is required to have atleast one unbiased muon trigger. Muon triggers with a cut on impact parameter of tracks (to have well separated decay vertex) are not included, as they bias physical measurement relevant to this analysis.

5.1.2 Monte Carlo Event Samples

To understand the detector response to the physical process, and to cross-check the whole procedure, we have generated the decay chains $B_s^0 \to J/\psi\phi$ and $B_d^0 \to J/\psi K^*$ with a full detector simulation. The details of the MC generation are given below:

1. **MC Signal of $B_s^0 \to J/\psi\phi$ Decay**

   To simulate the decay chain $B_s^0 \to J/\psi\phi$, $J/\psi \to \mu^+\mu^-$, $\phi \to K^+K^-$ we use the SVV_HELAMP model [48] in the EvtGen generator interfaced to the Pythia program. The decay amplitude (A) is specified by the helicity amplitudes (H) which are given as arguments for the decay. The arguments are H_+, H_0, and H_-, specified as magnitude and phase. Here, we use the parameters (1.0, 0.0, 0.0, 0.0, 1.0, 0.0), which corresponds to CP-even state. This choice corresponds to $A_{||}$=1, $A_\perp$=0, and A_0=0 in the linear polarization basis, while for CP-odd state, we use the parameters (1.0, 0.0, 0.0, 0.0, -1.0, 0.0), corresponds to $A_{||}$=0, $A_\perp$=0, and A_0=-1.

   The decay $J/\psi \to \mu^+\mu^-$ is simulated using the VLL model of the PHOTOS package. The VSS model is used in the decay $\phi \to K^+K^-$. The amplitude for this decay is

given by $A = \varepsilon^{\mu} v_{\mu}$ where ε is the polarization vector of the parent particle and the v is the velocity (obtained from four momentum vector) of the first daughter. As an example, definition of CP-even state under `EvtGen` is shown below:

```
noMixing
Decay anti-B_s0
1.000    J/psi   phi             SVV_HELAMP 1.0 0.0 0.0 0.0 1.0 0.0;
Enddecay
Decay J/psi
1.000    mu+  mu-               PHOTOS  VLL;
Enddecay
Decay phi
1.000   K+   K-                          VSS;
Enddecay
End
```

The B_s^0 proper decay length is 439 μm in the EvtGen ptable file. Before passing the generated events through the suite of programs for the detector simulation, hit simulation, track and particle reconstruction, we apply the following "pre-geant" selection cuts on event generator output:

- presence of the decay chain $\overline{B_s^0} \to J/\psi\phi$.
- $p_T(\mu) \geq 1.5$ GeV.
- $p_T(K^{\pm}) \geq 0.5$ GeV.
- $p_T(\phi) \geq 0.7$ GeV.
- $p_T(B_s^0) \geq 4.0$ GeV.

The number of reconstructed events of the pure CP-even state, passing all event selection criteria, is 25 K. We have also generated 23 K events of pure CP-odd state.

2. **MC Signal of $B_d^0 \to J/\psi K^*$ Decay**

   Again to simulate the decay chain $B_d^0 \to J/\psi K^*$, $J/\psi \to \mu^+\mu^-$, $K^* \to K^\pm\pi^\mp$ we use the SVV_HELAMP model in the EvtGen generator interfaced to the Pythia program. We use the parameters (1.0 0.0 0.0 0.0 -1.0 0.0), which corresponds to CP-odd state. This choice corresponds to $A_{||}$=0, $A_\perp$=0, and A_0=-1 in the linear polarization basis. The decay $J/\psi \to \mu^+\mu^-$ is simulated using the VLL model of the PHOTOS package, analogous to $B_s^0 \to J/\psi\phi$.

   The B_d^0 proper decay length is 464 μm in the EvtGen ptable file. Before passing the generated events for the full detector simulation, we apply the following "pre-geant" selection cuts:

   - presence of the decay chain $B_d \to J/\psi K^*$.
   - $p_T(\mu) \geq 1.5$ GeV.
   - $p_T(K^+) \geq 0.5$ GeV and $p_T(\pi^-) > 0.5$ GeV.
   - $p_T(K^*) \geq 0.7$ GeV.
   - $p_T(B_d) \geq 4.0$ GeV.

   The total number of reconstructed events are 25K.

In simulating the detection and reconstruction of the B mesons, we have assumed a fully efficient event trigger. But for a realistic simulation, we should pass the MC events through a trigger simulation tool. There is a complication arising from the fact that the event selection was based on the presence of two muons of loose quality in the final state, independent of the trigger condition that was satisfied by the event. As a result, the kinematic spectra of objects such as the leading and trailing muon, J/ψ, leading and trailing kaons/pions, ϕ/K^*, and the parent B meson in data are harder than in MC. We correct for this difference by deriving an event weight by forcing the p_T distributions of J/ψ to agree between data and MC for the central and forward regions, separately, and injecting the resulting weight in the MC distributions.

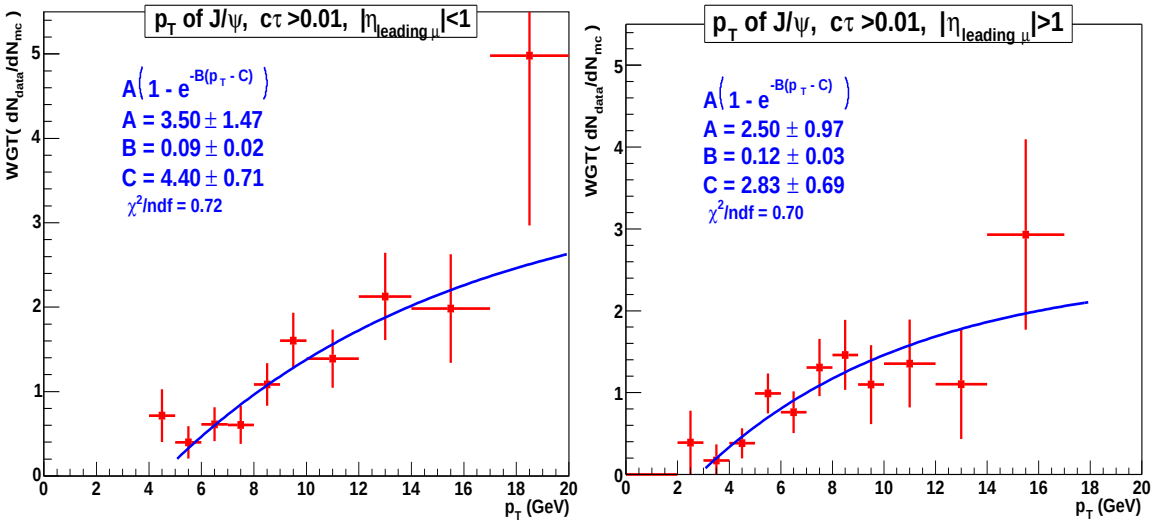

Figure 5.1: Weight factor as a function of $p_T(J/\psi)$, used to correct MC p_T distribution of B_s^0 and B_d^0 decay objects for central region (left) and forward region (right).

We use the pseudo-rapidity of the leading muon to define the two regions as $|\eta_{\mu 1}| < 1$ and $|\eta_{\mu 1}| > 1$, called central region and forward region respectively. To select a data sample dominated by the signal, we require invariant mass of B_s^0 between 5.26–5.42 GeV, with secondary vertex displaced at least by 100 μm, with respect to primary vertex. Fig. 5.1 shows the behavior of the relative weight factor as a function of $p_T(J/\psi)$ for the central and forward regions. We apply these weight factors to correct the simulated transversity distribution of the signal, as will be discussed in the section on the fitting procedure. In Appendix B, the p_T distributions of the objects (leading and trailing muons, J/ψ, leading and trailing kaons, ϕ and B_s^0), in the central and forward regions, before and after the correction are shown. It can be seen that the corrected MC distributions are in a good agreement with data.

5.2 B Decay Reconstruction

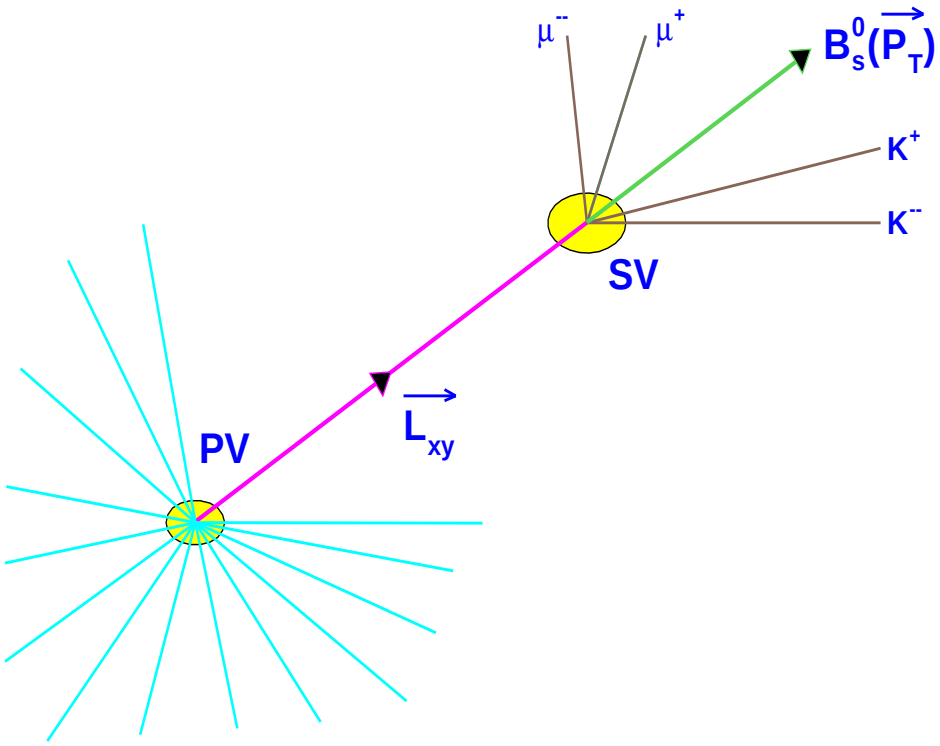

Figure 5.2: B_s^0 decay topology, where PV is the primary vertex and SV is the secondary vertex.

To reconstruct the decay sequences $B_s^0 \to J/\psi(\to \mu^+\mu^-)\phi(\to K^+K^-)$ and $B_d^0 \to J/\psi(\to \mu^+\mu^-)K^*(\to K^\pm\pi^\mp)$ [1] we start with di-muon data sample. The decay topology of $B_s^0 \to J/\psi(\to \mu^+\mu^-)\phi(\to K^+K^-)$ is shown in Fig. 5.2. The J/ψ and ϕ decays are governed by the electromagnetic and strong force respectively, so practically their decay products seem to be coming out of the B_s^0 decay vertex. The B mesons are long-lived particles since their decay is governed by the weak force. As a result they travel a significant distance from the primary vertex before their decay. We reconstruct the J/ψ decay using two opposite-sign muon tracks. Since we do not have the particle identification at DØ, we

[1] Here after we will discuss the reconstruction of B_s^0 events only, as the event reconstruction and selection for the B_d meson decay follows the same pattern.

use the kaon mass assignment to all opposite sign track pairs to reconstruct all the ϕ candidates in an event. For all the pairs of J/ψ and ϕ candidates in an event, we reconstruct the parent B_s^0 mesons. We reconstruct the primary vertex using the known beam spot point for the given run as the vertex seed, by excluding the decay products of the B_s^0 candidate. An event is stored if at least one B_s^0 candidate is found. To reconstruct the J/ψ and ϕ decays, the *V0* algorithm is used, while for B_s^0 candidates *VertexGlobalFitter* algorithm is used.

The vertex reconstruction algorithms relevant for this analysis, are part of the certified DØ package called "d0root_analysis" [66] with its following auxiliary packages:

```
d0root_analysis v00-09-54
d0root_tmbtree v00-09-28
d0root_btag v00-09-69
tmb_tree p14-br-05
AATrack header
```

5.2.1 Initial Event Selection

[2] To reconstruct the Primary Vertex we select tracks with $p_T > 0.3$ GeV. To reconstruct a J/ψ vertex, we use muon tracks with p_T >1.5 GeV. To eliminate spurious or mis-measured muon tracks, we apply the following cuts: at least one SMT hit, *dca* with respect to the Primary Vertex less than 2.5 cm, and *zca* with respect to the Primary Vertex less than 5.0 cm. The χ^2 of J/ψ vertex is required to be less than 20.0 and the invariant mass is required to be in the range of 2.7 to 3.4 GeV. To improve the mass resolution of B_s^0 candidates, the selected J/ψ candidates are subjected to the mass constraint of 3.072 GeV (J/ψ mass, as measured by DØ experiment).

To reconstruct a ϕ vertex, we use all tracks with p_T above 0.5 GeV with additional cuts such as at least one SMT hit, track *dca* with respect to Primary Vertex less than 2.5 cm, and *zca* with respect to Primary Vertex less than 5.0 cm. χ^2 of ϕ vertex is required to

[2] All numbers in the selection cuts are motivated by MC study.

be less than 10.0 and the allowed candidate mass range is 1.00 to 1.04 GeV. The initial event selection cuts are tabulated in Table 5.1. The resulting J/ψ mass distribution after applying these minimal requirements is shown in Fig. 5.3 (left).

Quantity	Cut
p_T of muon	> 1.5 GeV
χ^2 of J/ψ	< 20.0
J/ψ candidate mass	$2.7 < M(\mu^+, \mu^-) < 3.40$ GeV
p_T of hadronic track	> 0.5 GeV
SMT hits on track	> 0
χ^2 of ϕ	< 10.0
ϕ candidate mass	$1.00 < M(K^+, K^-) < 1.04$ GeV
B candidate mass	$4.8 < M(\psi, \phi) < 5.9$ GeV

Table 5.1: Summary of initial event selection cuts.

5.2.2 Final Event Selection

To select the final B_s^0 candidate sample we apply further kinematic and quality cuts. Transverse momentum thresholds for the B_s^0 and ϕ mesons are necessary to optimize the signal to background ratio, and to minimize the statistical uncertainty of the lifetime measurement. In this analysis we set the p_T thresholds at 6.0 GeV for B_s^0, 1.5 GeV for ϕ, and 0.7 GeV for each ϕ decay product.

The B_s^0 candidate sample is selected by requiring a $(J/\psi, \phi)$ pair to be consistent with that coming from a common vertex, and to have a mass in the range 5.0 – 5.8 GeV. J/ψ candidates are accepted if the unconstrained invariant mass resulting from the vertex fit is in the range 2.9 – 3.25 GeV. For events in the central rapidity region (defined by the requirement on the pseudo-rapidity of the higher p_T muon $|\eta_{\mu 1}| < 1.0$), we require the transverse momentum of J/ψ to exceed 4 GeV. ϕ candidates are required to satisfy a fit to a common vertex, and to have the invariant mass in the range of 1.01 – 1.03 GeV.

We require the B_s^0 proper decay length to be well measured, with an accuracy of 60 μm. Finally, we reject an event if the number of tracks other than muons in a cone $\Delta R < 1.0$

Quantity	Cut
J/ψ candidate mass	$2.9 < M(\mu^+, \mu^-) < 3.25$ GeV
p_T of J/ψ	> 4 GeV if $\|\eta\| < 1$
χ^2 of J/ψ	< 10.0
Decay length error of J/ψ candidate	< 0.03 cm
p_T of hadronic track	> 0.7 GeV
SMT hits on track	> 0
CFT hits on track	> 0
CFT + SMT hits on track	> 3
χ^2 of ϕ	< 15.0
p_T of ϕ	> 1.5 GeV
ϕ candidate mass	$1.01 < M(K^+, K^-) < 1.03$ GeV
Decay length error of B_s^0 candidate	< 0.006 cm
p_T of B_s^0	> 6.0 GeV
Absolute decay length difference between B_s^0 candidate and J/ψ	< 0.04 cm
B_s^0 candidate mass	$5.0 < M(J/\psi, \phi) < 5.8$ GeV

Table 5.2: Summary of final event selection cuts.

around J/ψ are greater than 25, as we donot expect a jet around J/ψ within a small cone. The final event selection cuts are tabulated in Table 5.2. After applying all final selection cuts, more than 96% of the time we are left with one B_s^0 candidate per event (Fig. 5.3, right). In case of multiple candidates, we select the one with the highest $\phi(p_T)$. Monte Carlo studies show that the p_T spectrum of the ϕ mesons coming from B_s^0 decays is harder than the p_T of a pair of a random tracks from the underlying events. 9699 events survived after raw and final selection cuts. These events are used in this analysis for measurement of lifetime and other physical parameters.

Background is divided into two categories, based on their origin and lifetime characteristics. "Prompt" background is due to directly produced J/ψ mesons accompanied by random tracks arising from hadronization. This background is distinguished from "non-prompt" background, where the J/ψ meson is a product of a $B-$hadron decay while the tracks forming the ϕ candidate emanate from a multi-body decay of the same $B-$hadron or from the underlying event. For the sake of discussion, we define the "prompt" events

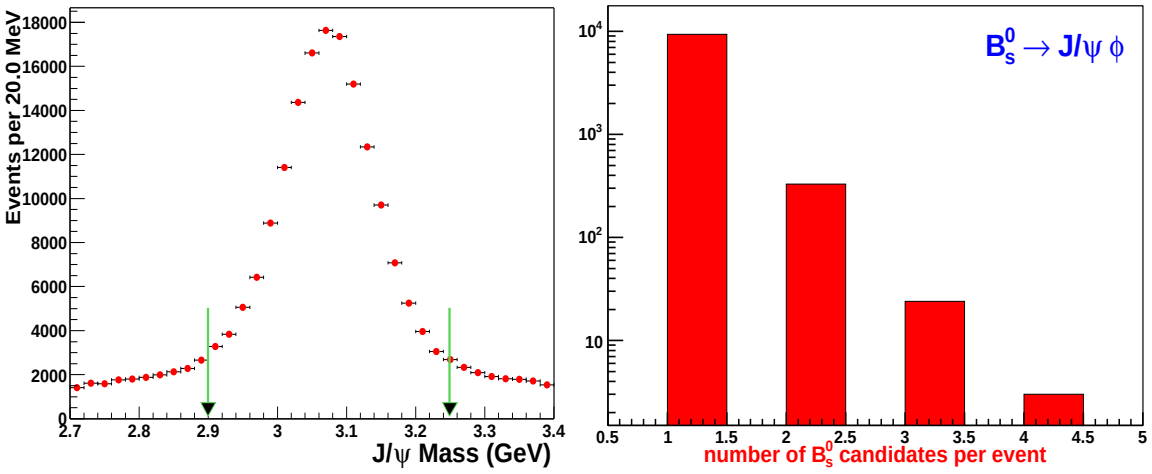

Figure 5.3: Left: J/ψ candidate mass distribution after applying initial event selection cuts. The arrows show the mass range for final event selection. Right: Number of B_s^0 candidates per event, after final event selection cuts.

having proper decay length ct (see Eq. 5.3) to be less then 5 times to its error i.e. ct /σ(ct) < 5. We define the signal region as 5.26$< M(B_s^0) <$5.42 GeV and the background region as $M(B_s^0)$ <5.2 GeV or $M(B_s^0)$ >5.5 GeV.

For the selected B_s^0 candidates, invariant mass distribution of the J/ψ candidates is shown in Fig. 5.4(left). With the final event selection cuts, but without applying ϕ mass range cut, the invariant mass of the ϕ candidates for signal-dominated subsample is shown in Fig. 5.4(right). The resulting invariant mass distribution of the $(J/\psi, \phi)$ system is shown in Fig. 5.5 (left panel). The fitted curve is a projection of the maximum likelihood fit, described later. The fit assigns 513±33 events to due the B_s^0 decay. The B_s^0 signal for "long-lived" events, i.e. for events with ct/σ(ct) >5, is shown in Fig. 5.5 (right panel). Lifetime distribution of the B_s^0 candidates for signal region and side band region is shown in Fig. 5.6, which shows clear distinction between signal and background lifetime behavior. In Fig. 5.7 we show the scatter plot of the invariant mass distribution of the (K^+, K^-) pair (ϕ candidate) versus mass of the $(J/\psi, \phi)$ system for the selected candidates events for the data (left) and for the MC (right).

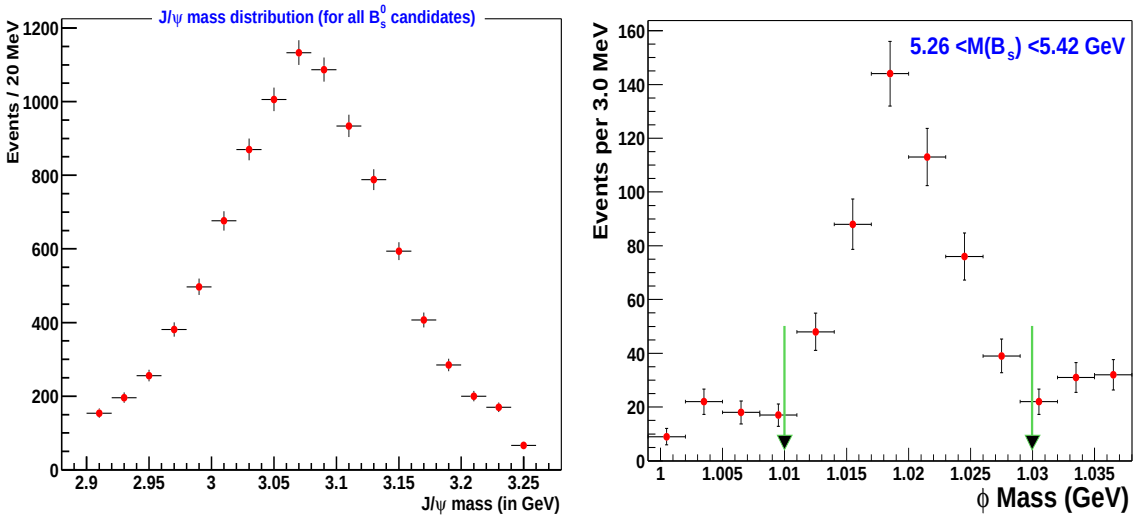

Figure 5.4: Left: The invariant mass distribution of the J/ψ candidates for the selected B_s^0 candidates. Right: The invariant mass distribution of the ϕ candidates for the B_s^0 candidates in the signal-dominated region, the arrows show the mass range for final event selection.

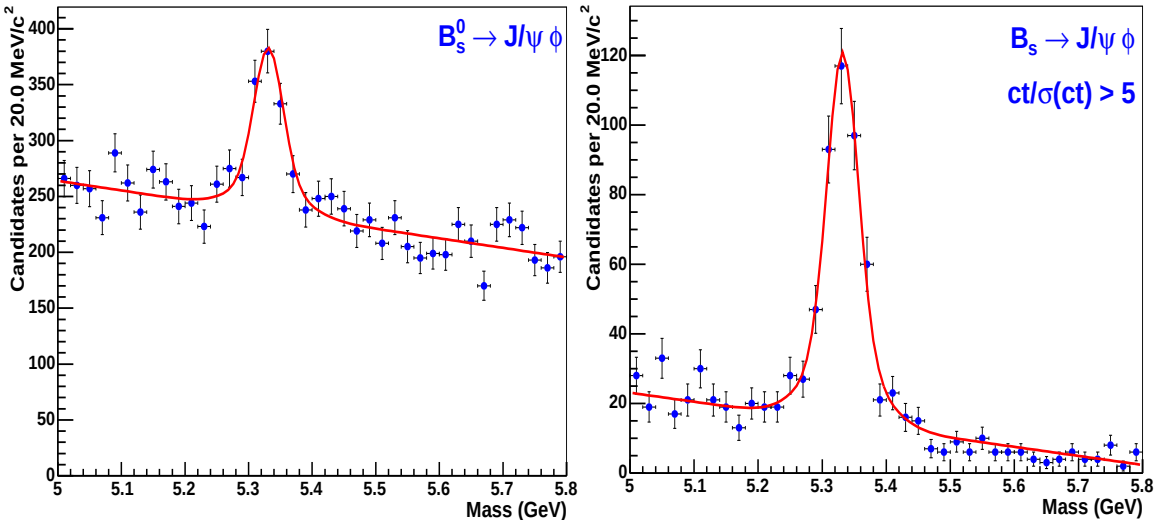

Figure 5.5: The Invariant mass distribution of the $(J/\psi, \phi)$ system for the B_s^0 . Left: all candidates; Right: prompt background suppressed.

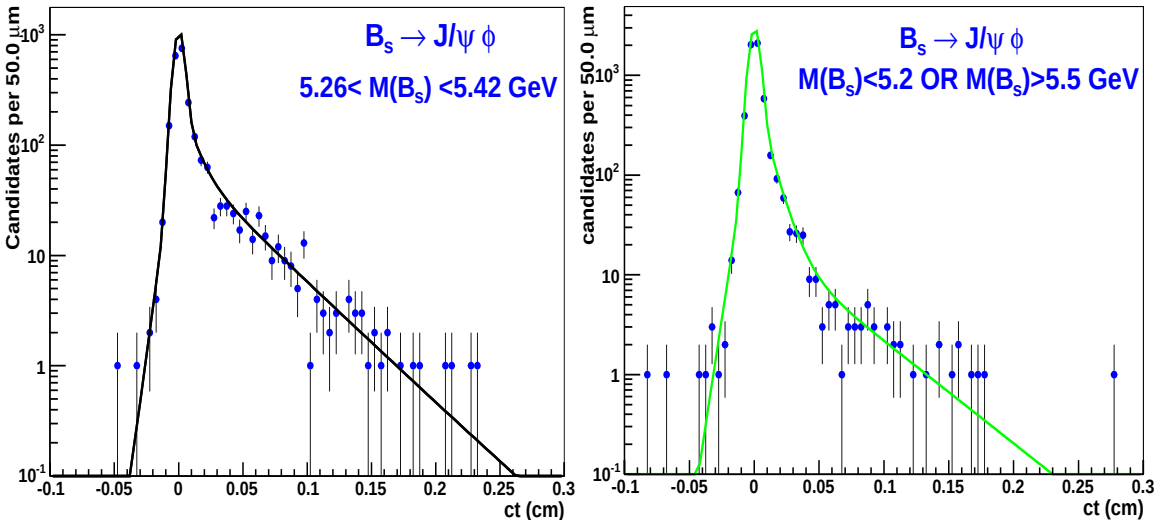

Figure 5.6: The Proper decay length distribution for the B_s^0 candidates, signal region(left), side band region(right).

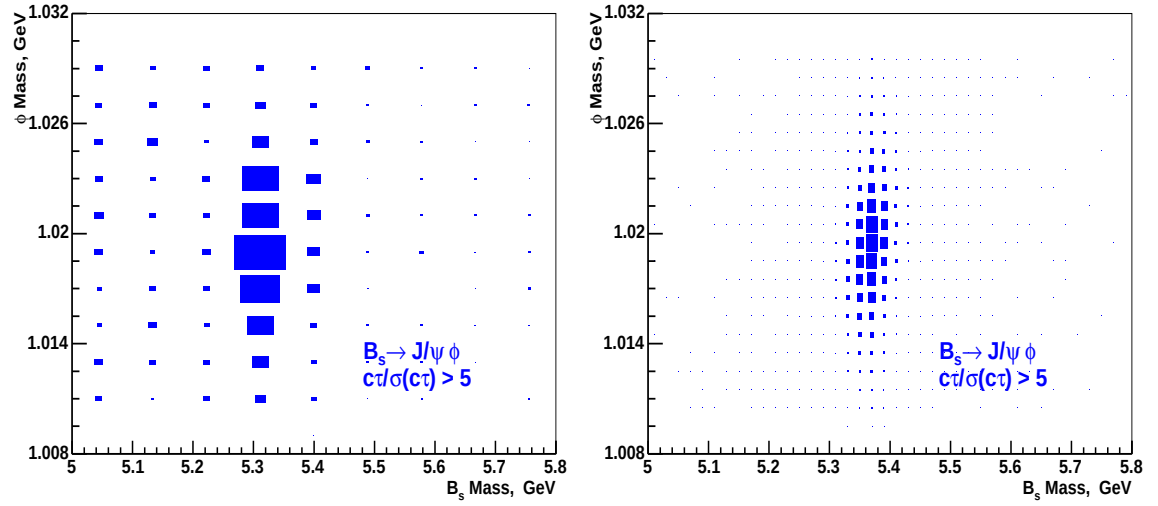

Figure 5.7: The invariant mass distribution of the (K^+, K^-) pair, i.e. ϕ candidates, versus mass of the $(J/\psi, \phi)$ system for the sample with the prompt background suppressed, for data (left) and MC (right).

5.3 Fit Variables and Probability Distribution Functions

We perform the unbinned maximum likelihood fit [67] to mass, lifetime and transversity distributions of the selected B_s^0 candidates. We define a likelihood function ($\mathcal{L}$), which is the product of probability distribution functions (PDFs) of all candidate events in a given sample and defined as:

$$\mathcal{L} = \prod_{i=1}^{N} [f_{sig}\mathcal{F}_{sig}^{i} + (1 - f_{sig})\mathcal{F}_{bck}^{i}]. \tag{5.1}$$

In the above equation, N=9699 is the total number of events. $\mathcal{F}_{sig}^{i}$ is the signal PDF, $\mathcal{F}_{bck}^{i}$ is the background PDF for a given event, and f_{sig} is the fraction of the signal in the sample.

To construct the PDFs we need to know how the signal and background look in the three-dimensional space of mass, proper decay length, and transversity. For the signal distributions, the model is given by theory, but for the background one depends entirely on the fitted empirical parametrization.

5.3.1 Input Variables

A brief introduction to the various input variables is given below:

- B_s^0 **Mass:** This is the first variable which goes to maximum likelihood fit, calculated from J/ψ and ϕ vertex as described in last section. In B_s^0 mass distribution of candidate events, B_s^0 signal sits on top of linear background, showing the presence of the signal.

- **Proper Decay Length and its Error:** The signed decay length of a B_s^0 meson is defined as the vector pointing from the primary vertex to the decay vertex projected on the B_s^0 momentum in the transverse plane as shown in Fig 5.2 and defined by

following Eq. :

$$L_{xy}^{B} = (\vec{x}_B - \vec{x}_{prim}) \cdot \vec{p}_T / p_T, \tag{5.2}$$

where $\vec{p}_T$ is the measured transverse momentum vector and p_T is its magnitude. The proper lifetime, t, and the proper decay length, ct, are then defined by the relation:

$$ct = L_{xy}^{B} \cdot M_{B_s^0} / p_T, \tag{5.3}$$

where $M_{B_s^0} = 5.3696$ GeV is the world average mass of the B_s^0 meson [23]. Proper decay length distribution is a clear visualization of long lived particles versus prompt background (see Fig. 5.6). This variable together with mass can be used to identify probable signal events among all B_s^0 candidates.

The distribution of the proper decay length uncertainty ($\sigma(ct)$) of B_s^0 meson is shown in Fig. 5.8. It peaks around 25 μm and has a long tail. As said earlier we select events with the proper decay length uncertainty below 60 μm. The corresponding MC uncertainties are $\approx$20% lower. We present this comparison for the record. This mismatch does not affect our results, we use the proper length error distributions from data, allowing, in addition, for a possible systematic underestimation of the measurement errors.

- **Transversity:** The definition of the transversity variable is given in section 2.5. This is a very important and useful variable to separate CP-even state and CP-odd state among B_s^0 signal events as described in section 2.5. Transversity distribution for pure CP-even and CP-odd sample is shown in Fig. 5.9.

5.3.2 Probability Distribution Functions (PDFs)

Signal Parametrization

The signal PDF is a product of the signal mass PDF, and a function describing the sum of the time evolution of the acceptance-corrected transversity distributions of the CP-even and odd states.

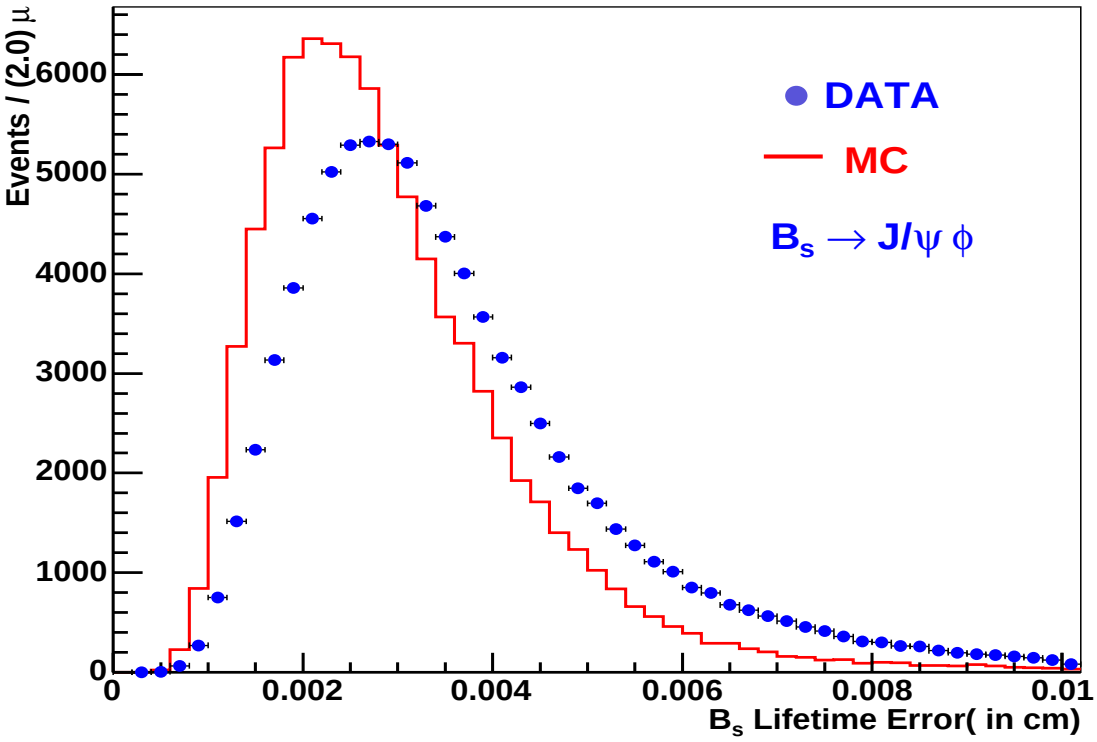

Figure 5.8: Distribution of the uncertainty of the decay length of B_s^0 candidates

- **Signal Mass PDF:** B_s^0 signal peak is of Gaussian shape because of detector resolution. Due to the wide range of particle momenta and the number of hits on tracks, we have a double Gaussian (sum of two Gaussian) shape, where Gaussian PDF is given by:

$$G(m_k\ |\mu,\sigma) = \frac{1}{\sigma\sqrt{2\pi}} exp\left(\frac{(m_k-\mu)^2}{2\sigma^2}\right). \tag{5.4}$$

  In the above Eq., m_k is the mass for k^{th} event, μ and σ are two free parameters for the mean and the resolution of B_s^0 signal. The double Gaussian function is given by: $N_1G(\mu_1,\sigma_1) + N_2G(\mu_2,\sigma_2)$. This shows that one need total 6 parameters, but we use

  – Common mean value to both Gaussian functions i.e. $\mu_1 = \mu_2 = \mu$.

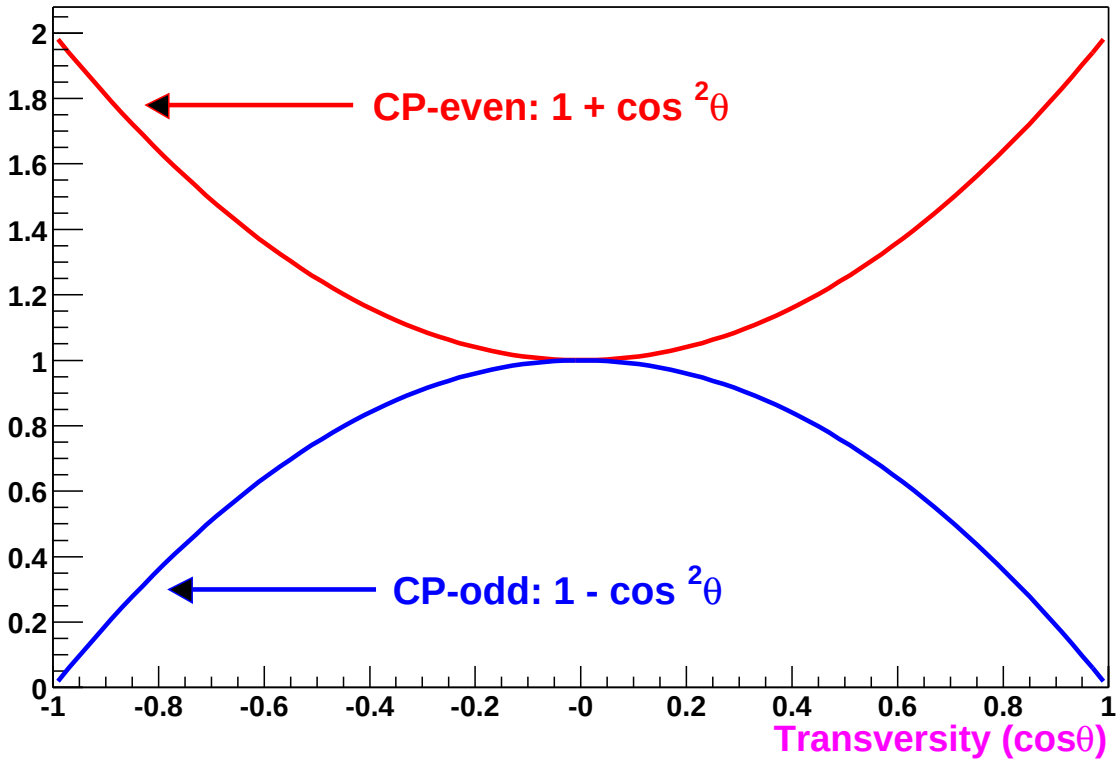

Figure 5.9: Distribution of the transversity of B_s^0 mesons, for CP-even and CP-odd state.

– Fixed sigma ratio and normalization constant from double Gaussian fit to signal dominated distribution given in Fig. 5.5(right). We use following fixed values, $\frac{\sigma_2}{\sigma_1} = 2.26$ and $N_2 : N_1 = 0.34 : 0.66$, from signal dominated mass distribution.

From the above conditions we finally need only two free parameters for signal mass PDF, these are mean mass (μ) and width of the narrow component(σ_1).

- **Signal Proper Decay Length and Transversity PDF:** The proper decay length and transversity distribution of the signal are determined by the time-dependent three-angle distribution for the decay of *untagged* B_s^0 mesons, i.e., summed over B_s^0 and $\overline{B}_s^0$, expressed in terms of the linear polarization amplitudes $|A_x(t)|$ and their relative phases δ_i given by Eq. 2.21. After integrating over the angles ϕ and ψ,

the one-angle distribution in transversity is given in Eq. 2.26. If in the one-angle distribution $cos\theta$ is represented by X, then term containing $(1 + X^2)$ corresponds to the CP-even term, while that containing (1 - X^2) corresponds to the CP-odd term. In the fit, we use lifetime of CP-even $\left(\tau_L = \overline{\tau}/\left(1 + \frac{\Delta\Gamma}{2\overline{\Gamma}}\right)\right)$ and CP-odd $\left(\tau_H = \overline{\tau}/\left(1 - \frac{\Delta\Gamma}{2\overline{\Gamma}}\right)\right)$ states, where $\overline{\tau}$ is average lifetime. For two free parameters, the $\Delta\Gamma/\overline{\Gamma}$ and fraction of CP-odd at time t=0($R_\perp$), the signal transversity PDF (T_{sig}) is given by:

$$\begin{aligned} & T_{sig}(X_k, ct_k, \sigma(ct_k) \mid c\tau_L, c\tau_H, R_\perp, S) \\ = \tfrac{3}{8} \Big[& (1 - R_\perp)\ Gexp(ct_k, \sigma(ct_k) \mid c\tau_L, S)\ (1 + X_k^2) \\ & + 2R_\perp\ Gexp(ct_k, \sigma(ct_k) \mid c\tau_H, S)\ (1 - X_k^2) \Big], \end{aligned} \tag{5.5}$$

where, X_k is the transversity of the k^{th} event. ct_k and $\sigma(ct_k)$ are proper decay length and its uncertainty of k^{th} event. The final one-angle distribution given by Eq. 2.26 is true only if detector response does not alter the distribution of three angles of generator level, during detector simulation chain. However detector response does distort this distribution. This modification is parameterized and included in three-angle distribution, which leads to a slightly different one-angle distribution, after integration over two angles, as described in Appendix[3] A.

In Eq. 5.5, the proper decay length distribution of each CP component of the signal is described as an exponential convoluted with a gaussian function with the width taken from the event-by-event estimate of uncertainty in proper decay length i.e. $\sigma(ct_k)$. To allow for the possibility that the lifetime uncertainty may have been systematically underestimated, we introduce a free scale factor S. The smeared distribution is

$$Gexp(ct_k, \sigma(ct_k) \mid c\tau, S) = \frac{1}{2}\ e^{xx}\ Erfc(yy), \tag{5.6}$$

where, ct_k and $\sigma(ct_k)$ are the proper decay length and its uncertainty for the k^{th} event. $xx = \left(\left(\frac{\sigma(ct_k)S}{c\tau}\right)^2 - \frac{ct_k}{c\tau}\right)$, $yy = \frac{1}{\sqrt{2}}\left(\frac{\sigma(ct_k)S}{c\tau} - \frac{ct_k}{\sigma(ct_k)}\right)$ and complementary error function ($Erfc$) is defined as: $Erfc(p) = \frac{2}{\sqrt{\pi}} \int_p^\infty e^{-t^2} dt$

[3]The final Signal Proper Decay Length and Transversity PDF used in the fit, including detector acceptance effect, is based on Eq. A.1 (as Eq. 5.5 is based on Eq. 2.26), while the constant N is determined by using Eq. A.2.

The PDF for the final one-angle distribution is given in Appendix A. It is similar to Eq. 5.5, but with a small new term $(|A_0(0)|^2 - |A_{\|}(0)|^2)$. This term is kept constant at 0.355 ± 0.066 from the CDF published result [70].

Background Parametrization

We allow for independent parameters for the prompt and non-prompt background components in mass, lifetime, and transversity, as discussed below.

- **Background Mass PDF:** Background mass distribution is a falling curve in the B_s^0 mass window. We have tried to describe it by the first order and higher degree polynomials and found that a linear shape given by $N(am_k + 1)$, where a is a free parameter, is sufficient. The distribution normalized to unity in the mass window M_{min} to M_{max} is given by:

$$P_M(m_k|a) = \frac{1 + a(m_k - M_{min})}{(M_{max} - M_{min}) + \frac{a}{2}(M_{max} - M_{min})^2}. \tag{5.7}$$

  We allow for separate parameters 'a' for the prompt and non-prompt background, so two free parameters are used for the background mass PDF.

- **Background Proper Decay Length PDF:** The prompt component of the background is simulated as a gaussian function centered at zero, with the width taken from the event-by-event estimate of uncertainty in proper decay length, scaled by the factor S. The non-prompt component is simulated as a superposition of one exponential for the unphysical decay length ($ct < 0$) region, mainly due to events with misreconstructed B vertices, and two exponentials for the positive ct region. We allow for free slopes and normalization factors of the three exponentials. (b_-, b_+ and b_{++}), and (n_-, n_+ and n_{++}). With a total of six free parameters, the background proper decay length PDF (τ_{bkg}) is given by:

$$\begin{aligned} &\tau_{bkg}(ct_k, \sigma(ct_k) \mid n_-, n_+, n_{++}, b_-, b_+, b_{++}, S) \\ &= (1 - n_- - n_+ - n_{++}) G(ct_k, \sigma(ct_k) \mid 0, S) \\ &+ n_- \, e^{(-ct_k \mid b_-)} \; + \; n_+ \, e^{(ct_k \mid b_+)} \; + \; n_{++} \, e^{(ct_k \mid b_{++})} \end{aligned} \tag{5.8}$$

where,

$$G(ct_k, \sigma(ct_k) \mid \mu, S) = \frac{e^{\frac{1}{2}a^2}}{\sqrt{2}\ \sigma(ct_k)\ (\ Freq(b) - Freq(c)\ )}, \tag{5.9}$$

and

$$e^{(ct_k \mid \tau)} = \frac{e^{\left(-\frac{ct_k}{\tau}\right)}}{\tau\left(1 - e^{-\frac{R}{\tau}}\right)}, \tag{5.10}$$

ct_k and $\sigma(ct_k)$ are the proper decay length and its uncertainty for the k^{th} event. μ is mean value and R is maximum/minimum value of the range[4] (from zero) in exponential fit. $a = (ct_k - \mu)/(\sigma(ct_k)S)$, $b = (-1 - \mu)/(\sigma(ct_k)S)$, $c = (1 - \mu)/(\sigma(ct_k)S)$ and normal frequency function $(Freq(p))$ is defined as: $Freq(p) = \frac{1}{\sqrt{2\pi}} \int_{-\infty}^{p} e^{-\frac{t^2}{2}} dt$.

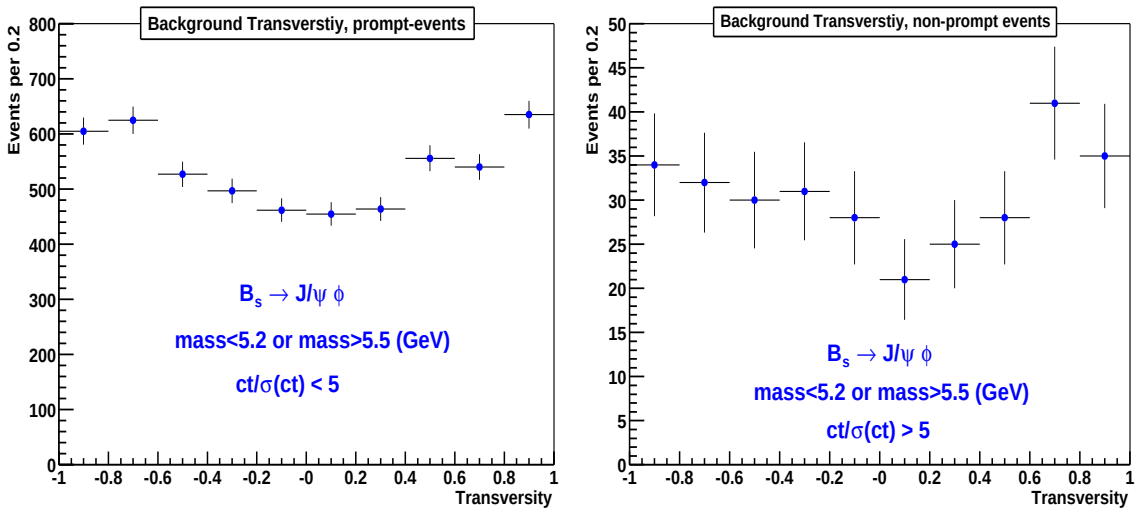

Figure 5.10: The Transversity distribution for the background B_s^0 candidates. Left: prompt events, Right:non-prompt events.

[4]For this analysis, we have chosen minimum value -0.15 cm and maximum value 0.45 cm, which is reasonable range from proper decay length distribution plot (see Fig.5.6).

- **Background Transversity PDF:** The transversity distributions for prompt and non-prompt events are shown in Fig. 5.10. We have used 4^{th} order symmetric polynomial to parameterize the transversity distribution of background:

$$P_T(X_k|A_2, A_4) = \frac{1 + A_2 X_k^2 + A_4 X_k^4}{2\left(1 + \frac{A_2}{3} + \frac{A_4}{5}\right)}. \tag{5.11}$$

Again, X_k is the transversity of the k^{th} event, A_2 and A_4 are free parameters. We allow for separate parameters of the transversity distribution for the prompt and non-prompt background, two for each component.

5.3.3 Fit Parameters

Below in Table 5.3 we summarize the free parameters of the likelihood function (defined in Eq. 5.1).

Index	Parameter name	notation	description
1	Signal fraction	f_{sig}	fraction of the signal in the total number of candidate events, defined in Eq. 5.1.
2	Scale factor	S	A free parameter multiplied to the proper decay length uncertainty ($\sigma(ct)$), in case if it is under/over estimated.
3	Mean signal mass	μ	The common mean value of the double Gaussian function in the signal mass PDF.
4	Mass resolution of narrow component	σ_1	The width of the narrow component in the double Gaussian function in the signal mass PDF.
5	Average B_s^0 lifetime	$\overline{\tau}$	The inverse of the average decay width.
6	Relative decay width difference	$\Delta\Gamma/\overline{\Gamma}$	Relative decay width difference between two CP eigenstates of (B_s^0, $\overline{B}_s^0$) system, where, $\Delta\Gamma = \Gamma_L - \Gamma_H$, $\overline{\Gamma} = (\Gamma_H + \Gamma_L)/2$ and $\overline{\tau} = 1/\overline{\Gamma}$.
7	CP-odd fraction at production time	$R_\perp$	Fraction of CP-odd component at time t=0 in $B_s^0 \to J/\psi\phi$ decay. In terms of linear polarization amplitude it is given by $R_\perp = \|A_\perp(0)\|^2$ and $(1 - R_\perp) = \|A_{\|}(0)\|^2 + \|A_0(0)\|^2$.

8	Prompt background mass slope	a_1	The coefficient of the mass term in the linear parametrization for the prompt background component.
9	Non-prompt background mass slope	a_2	The coefficient of the mass term in the linear parametrization for the non-prompt background component.
10	Negative background normalization constant	n_-	The normalization constant of the exponential in unphysical proper decay length region (ct < 0).
11	Positive background normalization constant	n_+	The normalization constant of the exponential in physical proper decay length region (ct > 0).
12	Long positive background normalization constant	n_{++}	The normalization constant of the second exponential in physical proper decay length region (ct > 0).
13	Negative background slope	b_-	The slope of the exponential function, in unphysical proper decay length region.
14	Positive background slope	b_+	The slope of the exponential function, in physical proper decay length region.
15	Long positive background slope	b_{++}	The slope of the exponential function, in physical proper decay length region.
16	Prompt background transversity-I	A_{12}	Coefficient of the $cos^2\theta$ term in the symmetric 4^{th} order polynomial $(1 + A_{12}cos^2\theta + A_{14}cos^4\theta)$ describing the transversity distribution of the prompt background.
17	Prompt background transversity-II	A_{14}	Coefficient of the $cos^4\theta$ term in the symmetric 4^{th} order polynomial $(1 + A_{12}cos^2\theta + A_{14}cos^4\theta)$ describing the transversity distribution of the prompt background.
18	Non-prompt background transversity-I	A_{22}	Coefficient of the $cos^2\theta$ term in the symmetric 4^{th} order polynomial $(1+A_{22}cos^2\theta+A_{24}cos^4\theta)$ describing the transversity distribution of the non-prompt-background.
19	Non-prompt background transversity-II	A_{24}	Coefficient of the $cos^4\theta$ term in the symmetric 4^{th} order polynomial $(1+A_{22}cos^2\theta+A_{24}cos^4\theta)$ describing the transversity distribution of the non-prompt background.

Table 5.3: Summary of the fit parameters used in unbinned maximum likelihood fit. In total there are nineteen free parameters in the fit.

5.4 Fitting Procedure and Fit Results

The likelihood function ($\mathcal{L}$) is maximized to get the most likely values of the free parameters. This maximization is done in the ROOT [68] framework, using the MINUIT [69] program.

5.4.1 Fit Results

In the default fit, we use all three variables (i.e. mass, proper decay length, and transversity) and all nineteen parameters are allowed to vary. We call this fit as "3D free $\Delta\Gamma/\overline{\Gamma}$" to distinguish it from various alternative fits. If we fix the parameter $\Delta\Gamma/\overline{\Gamma}$ at zero, the results are called "3D $\Delta\Gamma/\overline{\Gamma} \equiv 0$". If we do not use the transversity variable then the maximum likelihood fit results are called "2D". In the "2D" case we are left with only 13 free parameters belong to mass and lifetime PDFs, and this fit is equivalent to the "3D $\Delta\Gamma/\overline{\Gamma} \equiv 0$". The fit results are tabulated in Table 5.4.

Results of the "3D free $\Delta\Gamma/\overline{\Gamma}$" fit are presented in figures 5.11 – 5.14. The mass, proper decay length, and the transversity distributions, with the fit results overlaid are shown in Fig. 5.11, Fig. 5.12 (upper) and Fig. 5.12(lower) respectively. Fig. 5.13 shows fit projection on proper decay length distribution for all the B_s^0 candidates and sideband candidates. The 1-σ contour of $\Delta\Gamma/\overline{\Gamma}$ versus $R_\perp$ and $R_\perp$ versus f_{sig}, are shown in Fig. 5.14.

In case of conventional "2D" maximum likelihood fit to the B_s^0 candidates, using only mass and lifetime as input, we obtain $c\tau = 392 \pm 22$ μm, as the best estimate of the average lifetime for a single-exponential time evolution. This measurement is for an unknown mixture of CP-even and CP-odd components, under the assumption of equal acceptance of the two CP components. This result is same to the "3D $\Delta\Gamma/\overline{\Gamma} \equiv 0$" maximum likelihood fit result, shown in the 2^{nd} column of Table 5.4, which shows that there is no significant bias in the "2D" maximum likelihood fit measurements, which could have resulted from ignoring the effects of the kinematic acceptance as a function of transversity.

Index	Parameter	3D free $\Delta\Gamma/\overline{\Gamma}$	3D $\Delta\Gamma/\overline{\Gamma} \equiv 0$	2D
1	f_{sig}	0.053±0.003	0.053±0.003	0.053±0.003
2	S	1.29±0.02	1.29±0.02	1.29±0.02
3	μ (GeV)	5.331±0.002	5.331±0.002	5.331±0.002
4	σ_1 (MeV)	22.5±1.5	22.5±1.5	22.5±1.5
5	$c\overline{\tau}$ (μm)	417^{+39}_{-48}	392±22	392±22
6	$\Delta\Gamma/\overline{\Gamma}$	$0.24^{+0.28}_{-0.38}$	fixed at 0	not used
7	$R_\perp$	0.16±0.10	0.20±0.09	not used
8, 9	a_1, a_2	0.12±0.09, -1.0±0.04	0.12±0.09, -1.0±0.04	0.12±0.09, -1.0±0.04
10, 11	n_-, n_+	0.07±0.01, 0.17±0.01	0.07±0.01, 0.17±0.01	0.07±0.01, 0.17±0.01
12	n_{++}	0.030±0.006	0.030±0.006	0.030±0.006
13, 14	b_-, b_+ (μm)	51±4, 89±7	51±4, 89±7	51±4, 90±7
15	b_{++} (μm)	422±55	416±53	418±53
16, 17	A_{12}, A_{14}	1.00±0.20, -0.67±0.22	1.00±0.20, -0.67±0.22	not used
18, 19	A_{22}, A_{24}	0.62±0.33, -0.65±0.36	0.62±0.33, -0.65±0.36	not used

Table 5.4: Unbinned maximum likelihood fitting results for the B_s^0 decay.

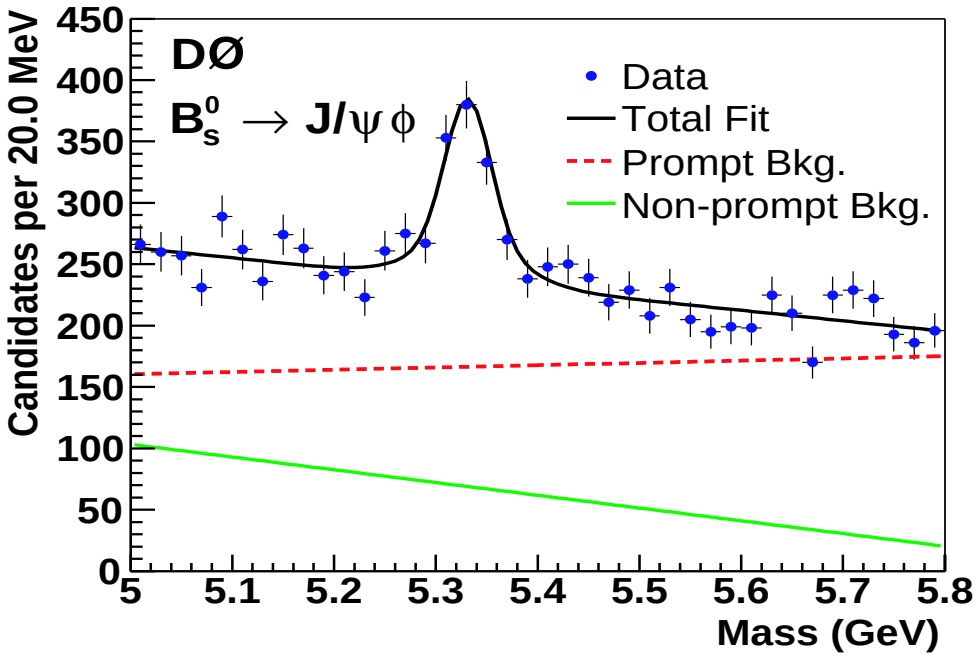

Figure 5.11: The invariant mass distribution of the B_s^0 candidates, the curves are projections of the maximum likelihood "3D free $\Delta\Gamma/\overline{\Gamma}$" fit.

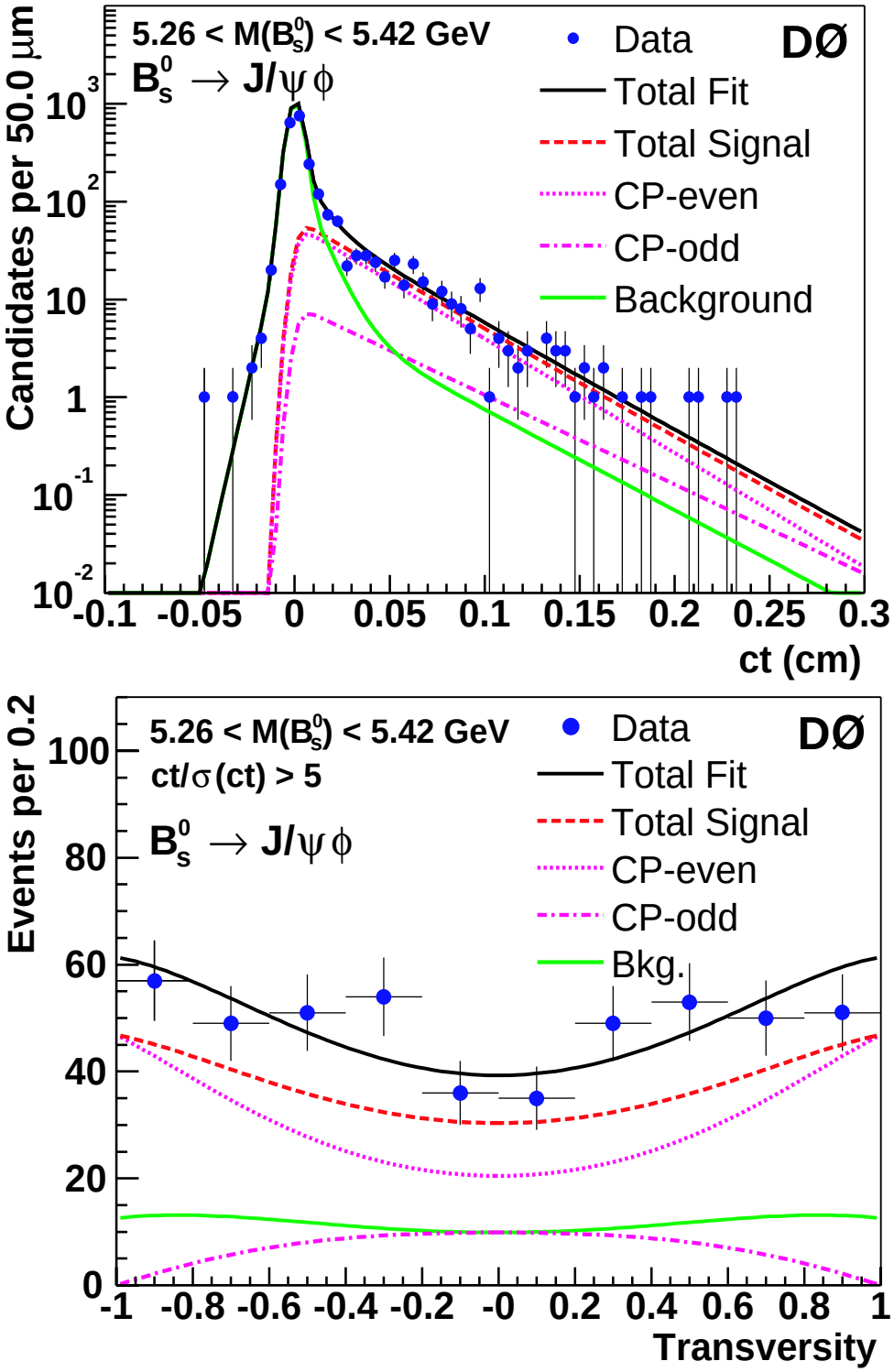

Figure 5.12: Upper: The proper decay length distribution of the B_s^0 candidates in the signal mass region. Lower: The transversity distribution of the B_s^0 candidates in the signal mass region for "non-prompt" events. In both the plots, the curves are projections of the maximum likelihood "3D free $\Delta\Gamma/\overline{\Gamma}$" fit.

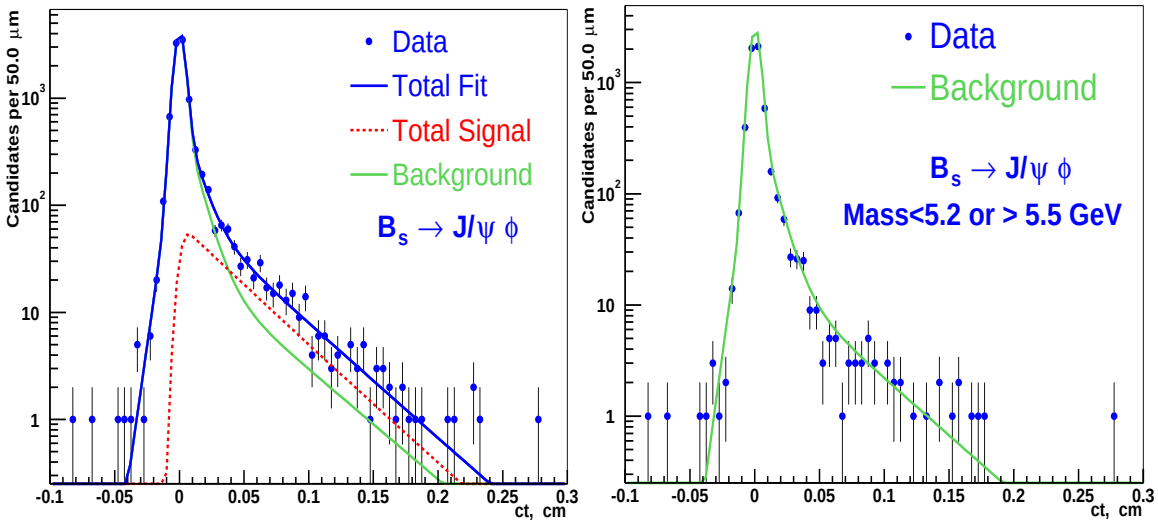

Figure 5.13: The proper decay length distribution of the B_s^0 candidates. Left: all candidates and Right: background region. The curves are projections of the maximum likelihood fit for "3D free $\Delta\Gamma/\overline{\Gamma}$". The curves show the signal contribution, dotted (red); the background, light solid line (green); and total, solid line (blue).

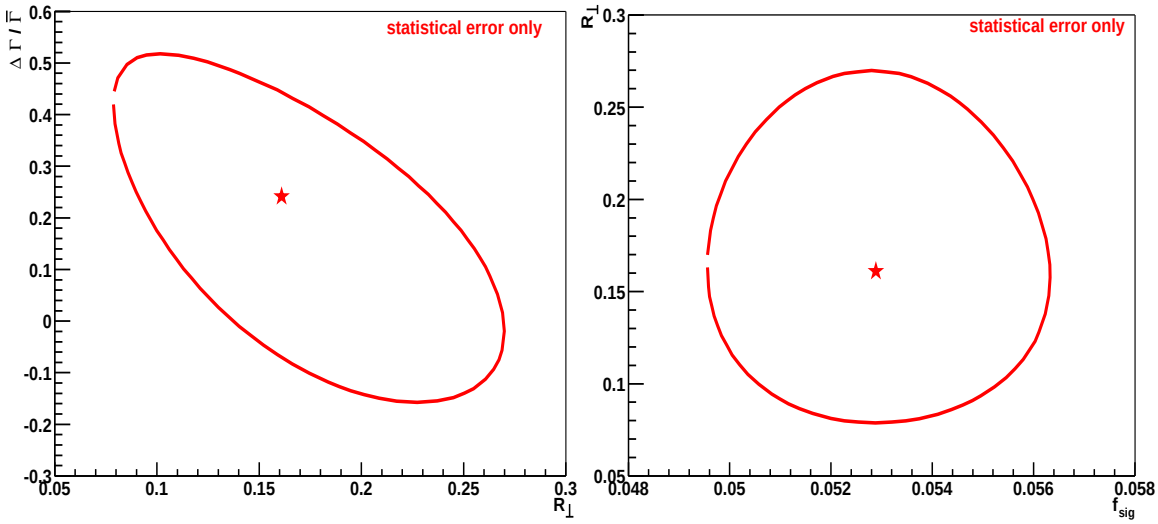

Figure 5.14: The 1-σ contours for "3D free $\Delta\Gamma/\overline{\Gamma}$" fit. Left: $\Delta\Gamma/\overline{\Gamma}$ vs. $R_\perp$; Right: $R_\perp$ vs. f_{sig}.

Fig. 5.15 shows one standard deviation (1-σ) contour for $c\overline{\tau}$ versus $\Delta\Gamma/\overline{\Gamma}$. It demonstrates the uncertainty range for these correlated parameters. Our best fit returns $\Delta\Gamma/\overline{\Gamma} = 0.24^{+0.28}_{-0.38}$ and $\overline{\tau}(B_s^0) = 1.39^{+0.13}_{-0.16}$ ps. For comparison CDF result [70] is also overlaid in Fig. 5.15, both results overlap within 1-σ uncertainty.

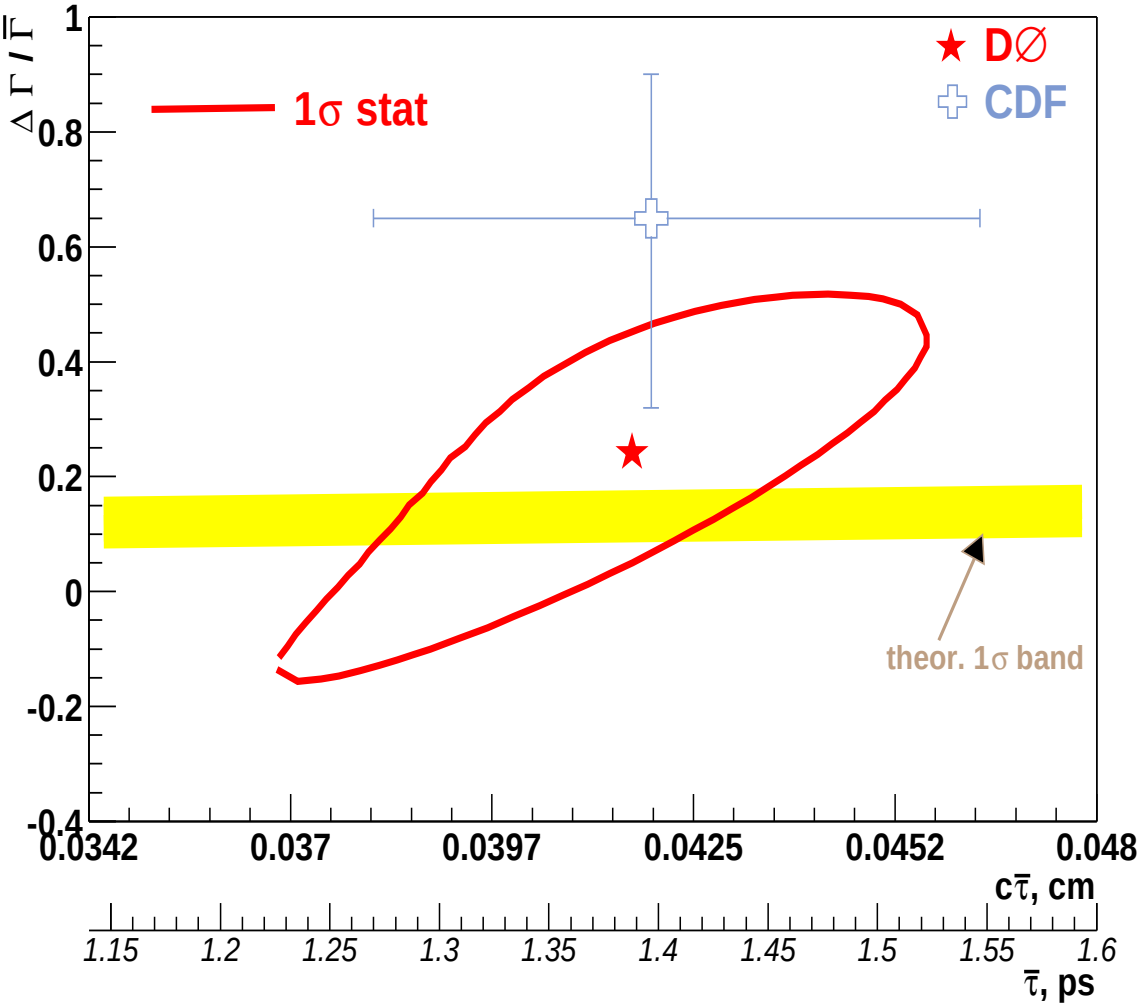

Figure 5.15: The 1-σ contour for the fitted parameters $c\overline{\tau}$(cm) and $\Delta\Gamma/\overline{\Gamma}$ from "3D free $\Delta\Gamma/\overline{\Gamma}$" fit.

Due to dominance of CP-even state, the lifetime associated with this state (τ_L) is measured more precisely as compared to CP-odd state lifetime (τ_H). Hence we expect parameters $c\overline{\tau}$ and $\Delta\Gamma/\overline{\Gamma}$ to be highly correlated, which can be seen in Fig. 5.15. In other words, among two CP state lifetimes[5], our data constrains τ_L to a higher precision (in the extreme case of $R_\perp = 0$, we would be able to measure τ_L, while τ_H would be totally inaccessible). The 1-σ contour of $c\tau_L$ versus $c\tau_H$ is shown in Fig. 5.16. Our results for the proper times of the two B_s^0 mass eigenstates are $c\tau_L = 372^{+37}_{-32}$ μm and $c\tau_H = 473^{+131}_{-130}$ μm.

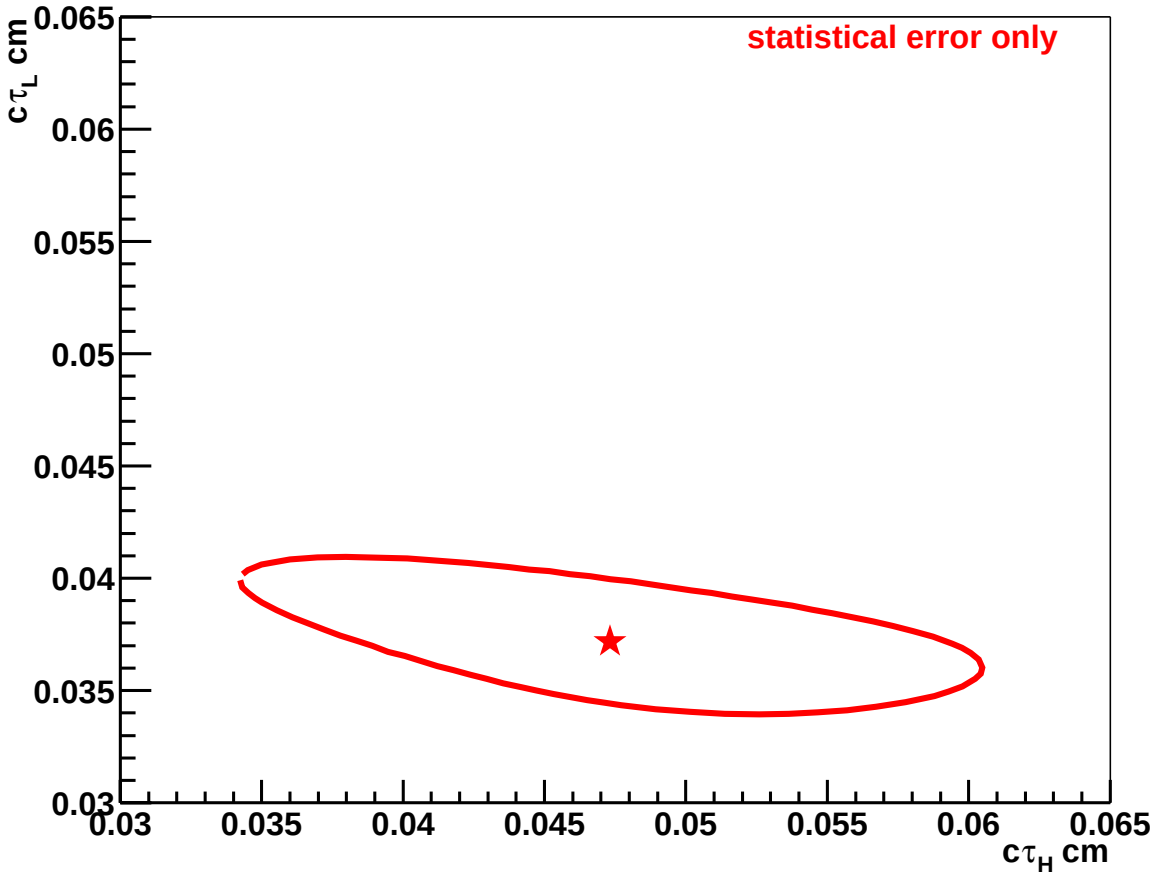

Figure 5.16: The 1-σ contour for $c\tau_L$(cm) and $c\tau_H$(cm).

[5]one can use $\Delta\Gamma/\overline{\Gamma} = (\Gamma^L - \Gamma^H)/\overline{\Gamma}$ and $\overline{\Gamma} = (\Gamma^L + \Gamma^H)/2 = 1/\overline{\tau}$ to get τ_L and τ_H, which then comes out to be $\tau_L = \overline{\tau}/\left(1 + \frac{1}{2}(\frac{\Delta\Gamma}{\overline{\Gamma}})\right)$ and $\tau_H = \overline{\tau}/\left(1 - \frac{1}{2}(\frac{\Delta\Gamma}{\overline{\Gamma}})\right)$

B_s^0 lifetime measurements from semileptonic (flavor-specific) data provide an independent constraint on the average lifetime and lifetime difference in the $(B_s^0,\ \overline{B}_s^0)$ system. The world average [23] B_s^0 lifetime from flavor-specific decay channels is $\tau_{fs} = 1/\Gamma_{fs} = 1.442 \pm 0.066$ ps, based on single-exponential fits, and determines the following relation [71] (shown with curved blue lines in Fig. 5.17) of $\overline{\Gamma}$ and $\Delta\Gamma/\overline{\Gamma}$:

$$\Gamma_{fs} = \overline{\Gamma} - (\Delta\Gamma)^2/2\overline{\Gamma} + \mathcal{O}(\Delta\Gamma)^3/\overline{\Gamma}^2. \tag{5.12}$$

Applying the above constraint to our measurement, we obtain $\overline{\tau}(B_s^0) = 1.39^{+0.06}_{-0.06}$ ps (or $c\overline{\tau}(B_s^0) = 418^{+17}_{-19}$ μm), and $\Delta\Gamma/\overline{\Gamma} = 0.25^{+0.14}_{-0.15}$. This result is consistent with the SM expectation [72] of 0.12 ± 0.05. The other fitted values are listed in Table 5.5.

Index	Parameter	"3D free $\Delta\Gamma/\overline{\Gamma}$"	"3D free $\Delta\Gamma/\overline{\Gamma}$" with WA Constraint
1	f_{sig}	0.053±0.003	0.050±0.003
2	S	1.29±0.02	1.29±0.02
3	μ (GeV)	5.331±0.002	5.331±0.002
4	σ_1 (MeV)	22.5±1.5	22.4±1.5
5	$c\overline{\tau}$ (μm)	417^{+39}_{-48}	418±16
6	$\Delta\Gamma/\overline{\Gamma}$	$0.24^{+0.28}_{-0.38}$	$0.25^{+0.14}_{-0.15}$
7	$R_\perp$	0.16±0.10	0.16±0.08
8	a_1	0.12±0.09	0.12±0.09
9	a_2	-1.00±0.04	-1.00±0.04
10, 11	n_-, n_+	0.07±0.01, 0.17±0.01	0.07±0.01, 0.17±0.01
12	n_{++}	0.030±0.006	0.030±0.006
13, 14	b_-, b_+ (μm)	51±4, 89±7	51±4, 89±7
15	b_{++} (μm)	422±55	416±53
16	A_{12}	1.00±0.20	1.00±0.21
17	A_{14}	-0.67±0.22	-0.67±0.22
18	A_{22}	0.62±0.33	0.62±0.33
19	A_{24}	-0.65±0.36	-0.65±0.36

Table 5.5: Unbinned maximum likelihood fitting results; Default "3D free $\Delta\Gamma/\overline{\Gamma}$" fit and a fit with a additional constraint from the world average (WA) lifetime from semileptonic decays.

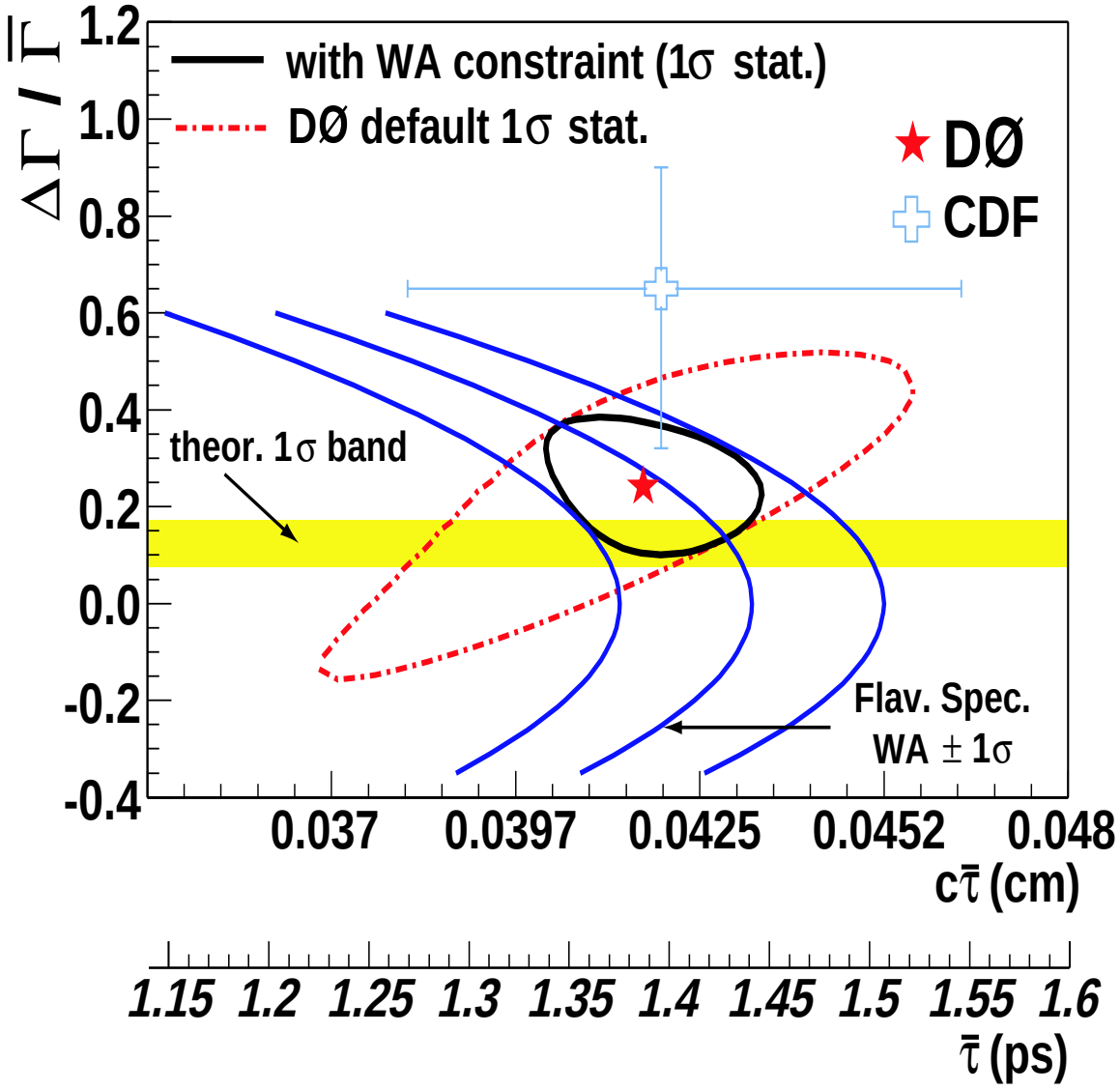

Figure 5.17: The DØ default 1-σ (stat) contour ($\delta \ln \mathcal{L} = 0.5$) compared to a 1-$\sigma$ band for the world average (WA) measurement based on flavor-specific decays, $\tau_{fs} = 1.442 \pm 0.066$ ps. The SM theoretical prediction is shown as the horizontal band.

To illustrate the asymmetric error on $\Delta\Gamma/\overline{\Gamma}$, likelihood scan plots for $\Delta\Gamma/\overline{\Gamma}$ are shown in Fig. 5.18. To calculate each point in these plots, the $\Delta\Gamma/\overline{\Gamma}$ is fixed to a value (on x-axis), the maximum likelihood "3D free $\Delta\Gamma/\overline{\Gamma}$" fit is repeated and value of -2ln($\mathcal{L}/\mathcal{L}_{min}$) is noted down, where $\mathcal{L}_{min}$ is value of likelihood function when fit is fixed to its best fitted parameters.

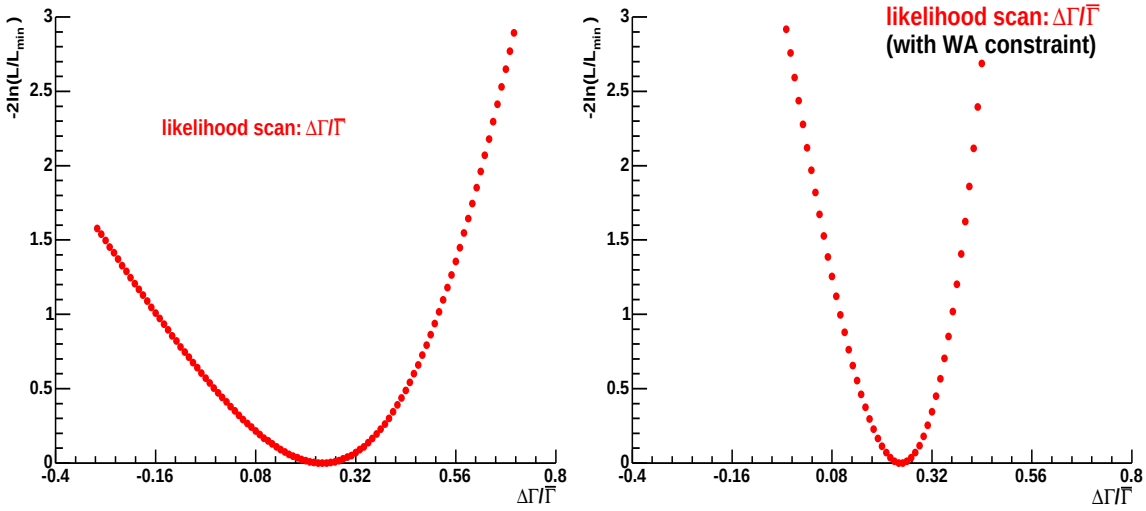

Figure 5.18: Likelihood scan plot for $\Delta\Gamma/\overline{\Gamma}$; Left: for "3D free $\Delta\Gamma/\overline{\Gamma}$" fit, Right: including WA constrain in "3D free $\Delta\Gamma/\overline{\Gamma}$" fit.

We do a series of alternative fits, at discrete values of $\overline{\tau}(B_s^0)$. The results for $\Delta\Gamma/\overline{\Gamma}$, its one standard deviation range, and the corresponding value of the likelihood, are listed in Table 5.6. The likelihood scan plot of $\Delta\Gamma/\overline{\Gamma}$ for a fixed value of $\overline{\tau}$ is shown in Fig. 5.19. For each assumed value of $\overline{\tau}(B_s^0)$, the likelihood as function of $\Delta\Gamma/\overline{\Gamma}$ is symmetric and parabolic.

$\overline{\tau}(B_s^0)$ (ps)	$\Delta\Gamma/\overline{\Gamma}$	$\Delta \ln \mathcal{L}$
1.23	-0.13 ± 0.15	0.51
1.27	-0.03 ± 0.17	0.32
1.31	0.07 ± 0.19	0.17
1.35	0.16 ± 0.21	0.04
1.39	0.24 ± 0.20	0.00
1.43	0.31 ± 0.19	0.06
1.47	0.37 ± 0.18	0.20
1.51	0.43 ± 0.18	0.42
1.55	0.48 ± 0.18	0.69

Table 5.6: Fit results for $\Delta\Gamma/\overline{\Gamma}$, while $\overline{\tau}(B_s^0)$ is fixed at the values from 1.23 ps to 1.55 ps in step of 0.04 ps.

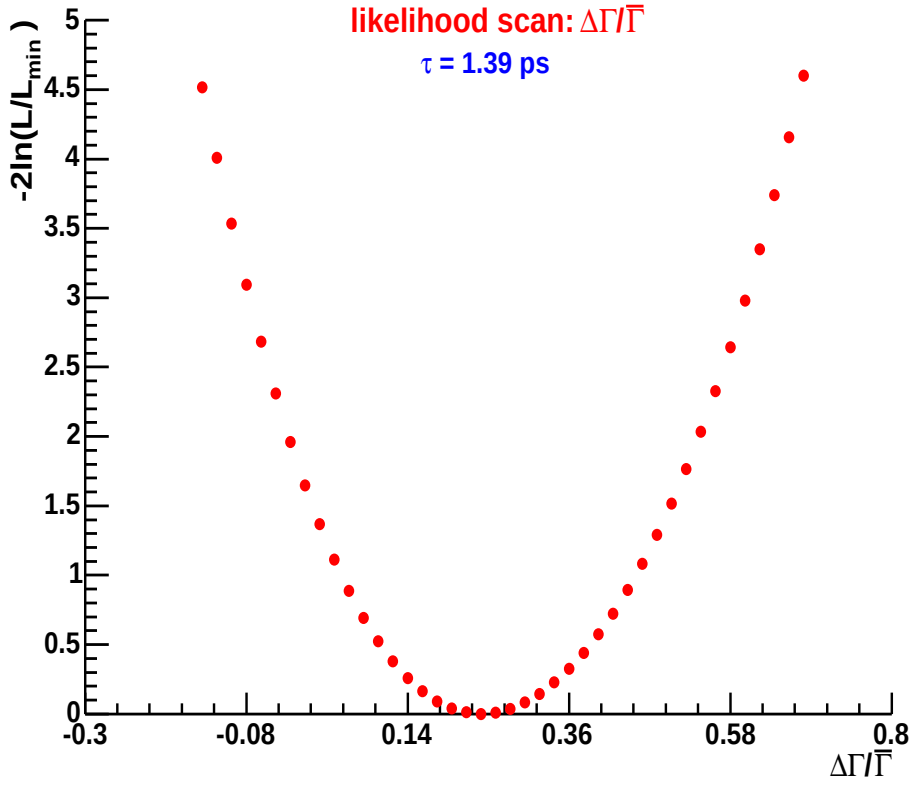

Figure 5.19: Likelihood scan plot for $\Delta\Gamma/\overline{\Gamma}$, for "3D free $\Delta\Gamma/\overline{\Gamma}$" fit, while $\overline{\tau}(B_s^0)$ is fixed to the values of 1.39 ps.

5.5 Systematic Uncertainties

Systematic uncertainties in this analysis have to be taken into account from many possible error sources. Some systematic uncertainties are unavoidable and will remain the same for the lifetime analysis carried out at DØ, while others can be reduced with improvement in event reconstruction and with more MC events. We have calculated all the systematic errors relevant for this analysis. The ones which are common for all the analysis at DØ are included with references.

5.5.1 Event Reconstruction and Fitting Procedure

We have verified the full procedure of the event reconstruction, and parameter estimation, by performing maximum likelihood fits on the sample of ≈48,000 reconstructed MC events, as presented in the previous sections.

Fig. 5.20 (upper) compares the proper decay length distribution of the B_s^0 reconstructed events with the generated input ($c\overline{\tau} = 439$ μm). We see no bias in the vertex reconstruction as the mean value of the residuals is consistent with zero to the accuracy of 0.1μm. Fig. 5.20 (lower, left) have analogous distributions for the transversity, again the mean of the residual is consistent with zero. Fig. 5.20 (lower, right) is the mass distribution for the reconstructed MC events, the mean of this distribution is same to the input B_s^0 mass. This shows that we have no bias in event reconstruction, and variables used in the maximum likelihood fits are measured with good accuracy.

The maximum likelihood "3D free $\Delta\Gamma/\overline{\Gamma}$" fit applied to the reconstructed MC events, returns $c\overline{\tau}$=437±2μm for the input of 439 μm, $R_\perp$=0.49±0.01 for the input of 0.48, and $\Delta\Gamma/\overline{\Gamma}$=0.025±0.025, for the input of 0. This verifies that the fit, allowing for a free lifetime difference, reproduces all the input correctly within statistical uncertainty. Fig. 5.21 (upper) shows the projection of the maximum likelihood fit on the proper decay length distribution.

The accuracy of the $R_\perp$ measurement has been measured as a function of input value

from 0 to 1 (see lower panel of Fig. 5.21). We observe no bias within the statistical uncertainty of 0.01. This is an important test of our signal/background models and the fitting procedure. It also justifies the final one angle distribution formula, given in Appendix A. We have made a tacit assumption that the detector acceptance in the three angles can be factorized. This test shows that this assumption does not lead to a bias exceeding ± 0.01 in $R_\perp$ and ± 0.025 in $\Delta\Gamma/\overline{\Gamma}$.

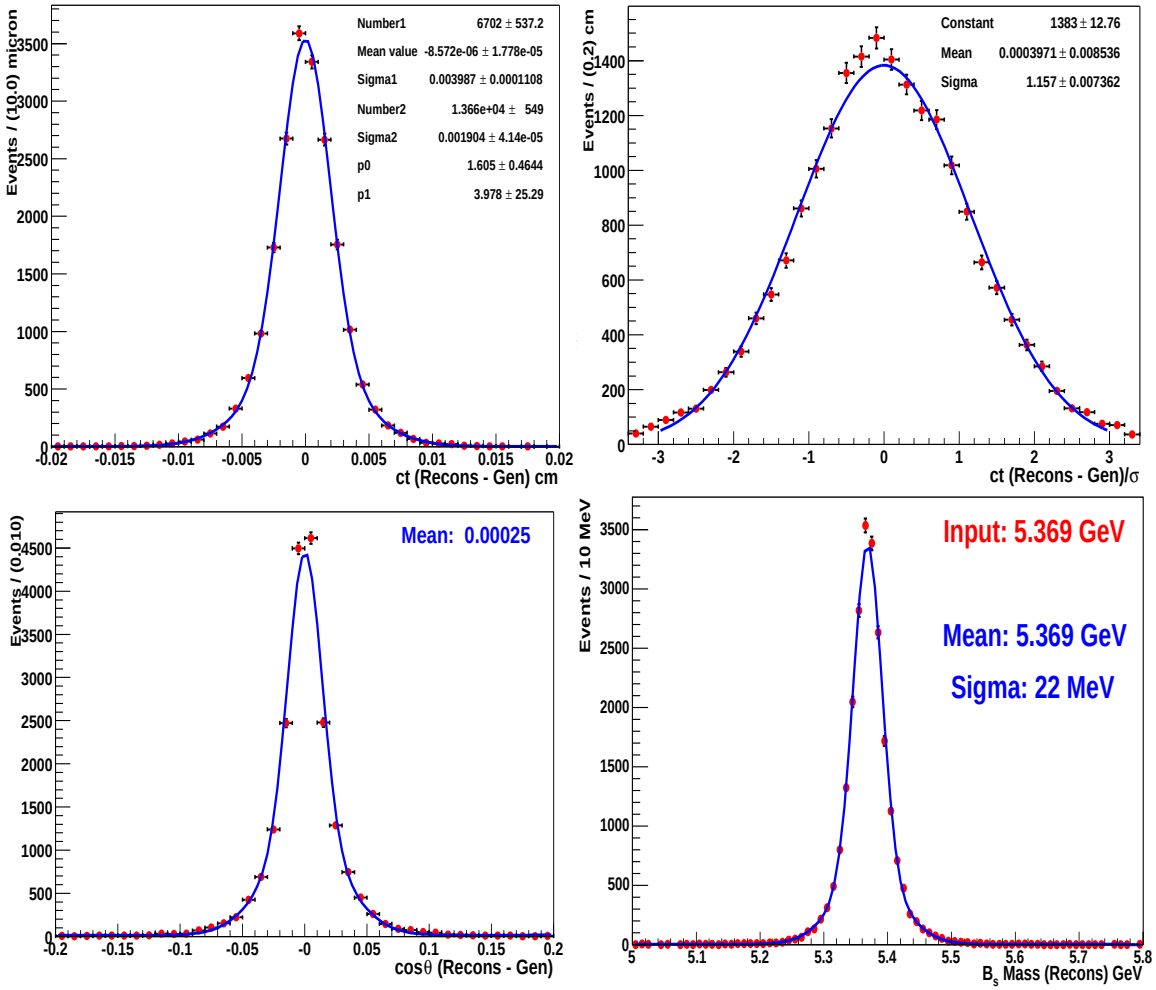

Figure 5.20: Upper: Residual distribution for proper decay length (left). Pull distribution (right). Lower: Residual distribution for transversity (left). B_s^0 mass distribution (right).

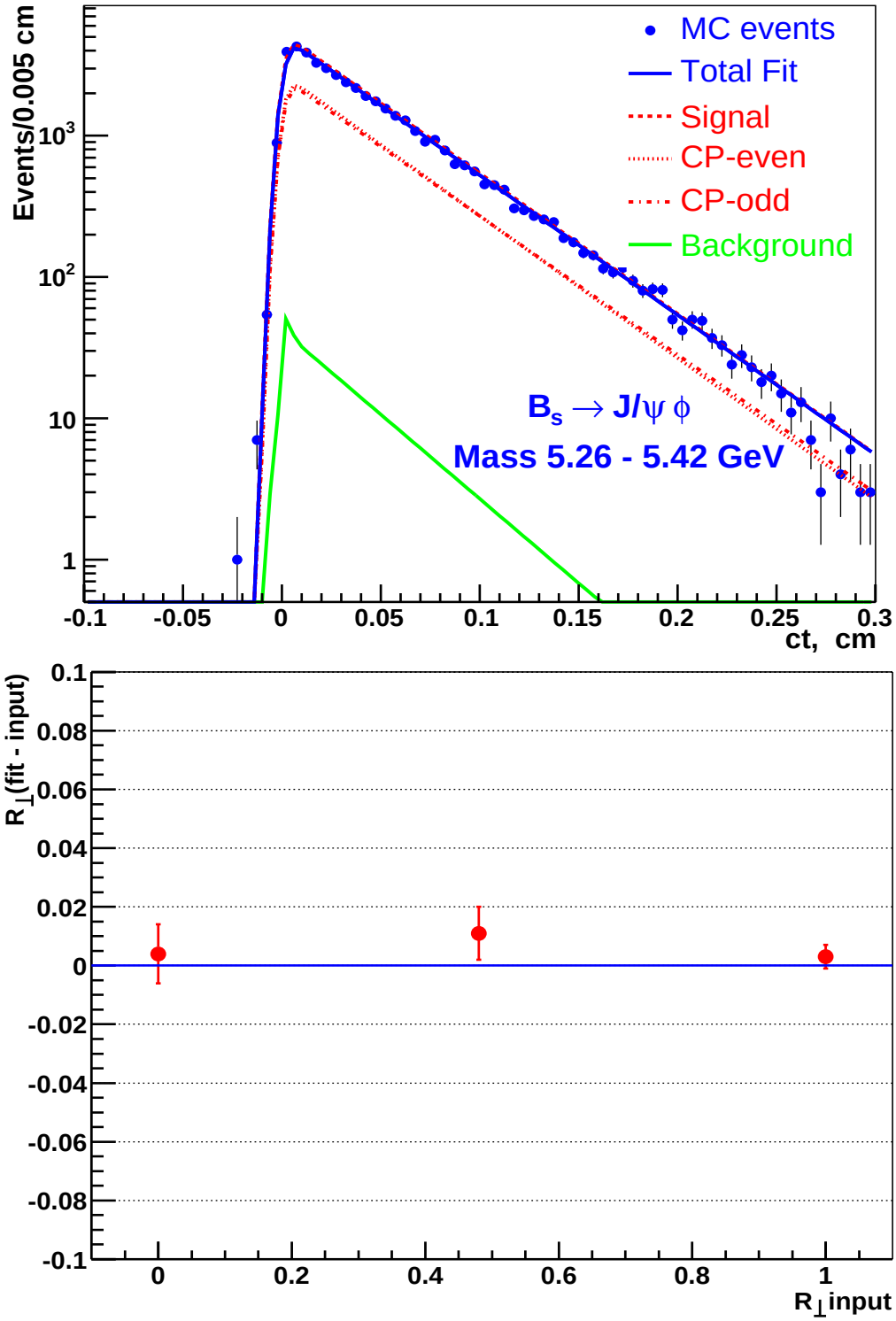

Figure 5.21: Upper: The proper decay length distribution for reconstructed MC events, with results of "3D free $\Delta\Gamma/\overline{\Gamma}$" fit overlaid. Lower: MC test of the CP-odd fraction measurement for the B_s^0 system. (Measured - Input)$R_\perp$ vs Input $R_\perp$.

5.5.2 Acceptance versus Transversity($\cos\theta$)

We have varied parameter B and C (values are given in Appendix A) in the efficiency function $(1 + B\cos^2\theta + C\cos^4\theta)$ by $\pm 1\sigma$, and repeated the maximum likelihood "3D free $\Delta\Gamma/\overline{\Gamma}$" fit, and redrawn the contour plots between $c\overline{\tau}$(cm) and $\Delta\Gamma/\overline{\Gamma}$. The variation includes the effects of the uncertainty of weight factors used for MC-data matching. The effects are shown in Fig. 5.22 and in Table 5.7.

5.5.3 Integration Over ϕ and $\cos\psi$

In the final one-angle formula used in the likelihood fit, we have varied the parameterization constants (values are given in Appendix A) of ϕ and $\cos\psi$ by $\pm 1\sigma$ and repeated the maximum likelihood fit, and redrawn the contour plot. The effects are shown in Fig. 5.22 and in Table 5.7.

5.5.4 Background Lifetime Model

We tested the sensitivity of the results to the assumption of the uniformity of the background shape across the entire mass region by repeating the fit in two alternative ranges, (5.0 – 5.65) GeV, and (5.15 – 5.8) GeV. We assign the appropriate systematic uncertainties to half of the difference in the results for $(c\overline{\tau}, R_\perp, \Delta\Gamma/\overline{\Gamma})$ (417.1 μm, 0.157, 0.268) and (415.8 μm, 0.165, 0.226).

5.5.5 Signal and Background Mass Model

We have repeated the maximum likelihood "3D free $\Delta\Gamma/\overline{\Gamma}$" fit with single-gaussian in signal mass probability distribution function, and with 2^{nd} order polynomial in background mass probability distribution function. The effects are included in Fig. 5.22 and in Table 5.7. The Fit projection of single-gaussian versus double-gaussian is shown in the upper panel of Fig. 5.23, while for 1^{st} versus 2^{nd} order polynomial is shown in the lower panel of Fig. 5.23.

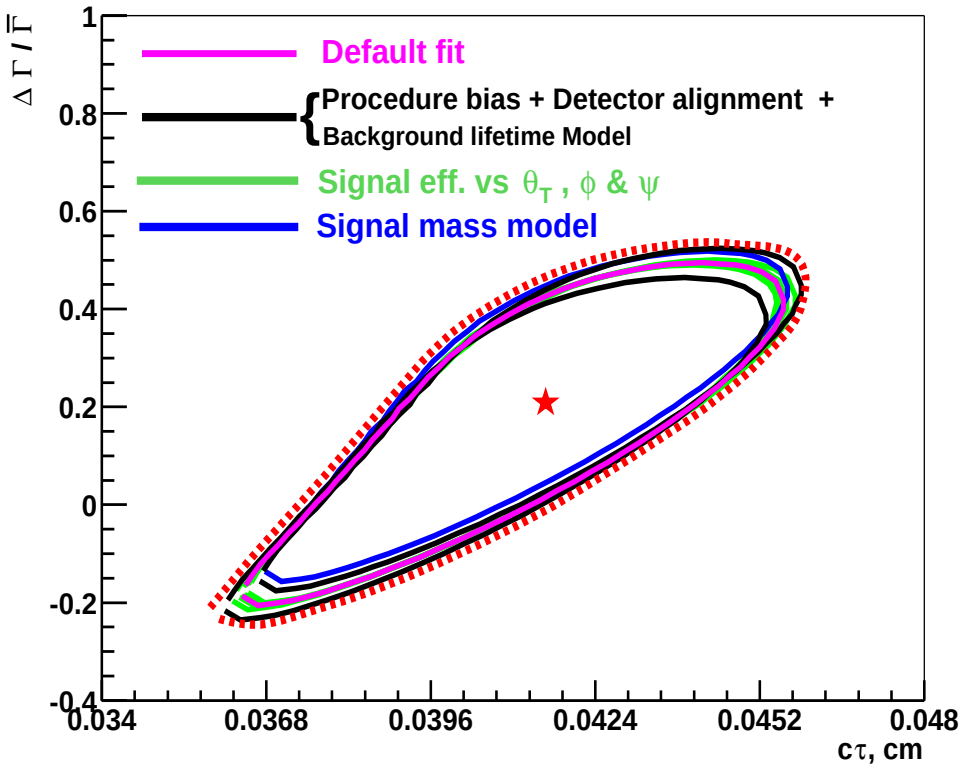

Figure 5.22: The 1-σ contour for the fitted parameters $c\overline{\tau}$(cm) and $\Delta\Gamma/\overline{\Gamma}$. An alternative diagram for all sources of the systematic uncertainty discussed in the text are drawn.

Source	$c\overline{\tau}(B_s^0)$, μm	$\Delta\Gamma/\overline{\Gamma}$	$R_\perp$	Comment
Procedure test	± 2.0	± 0.025	± 0.01	MC
Acceptance vs. $\cos\theta$	± 0.6	± 0.001	± 0.005	MC
Integration over φ, ψ	± 0.2	± 0.001	± 0.02	MC + [70]
Momentum scale	-3.0	–	–	data
Signal mass model	± 1.0	$+0.009, -0.017$	± 0.007	data
Background mass model	-3.5	$+0.02$	-0.002	data
Detector alignment	± 2.0	–	–	[73]
Background lifetime model	± 0.5	± 0.016	± 0.005	data
Total	$-5.6, +3.1$	$-0.04, +0.03$	± 0.02	

Table 5.7: The sources of systematic uncertainties are summarized in this table, at the end we have given the total systematic errors on physical quantities of interest.

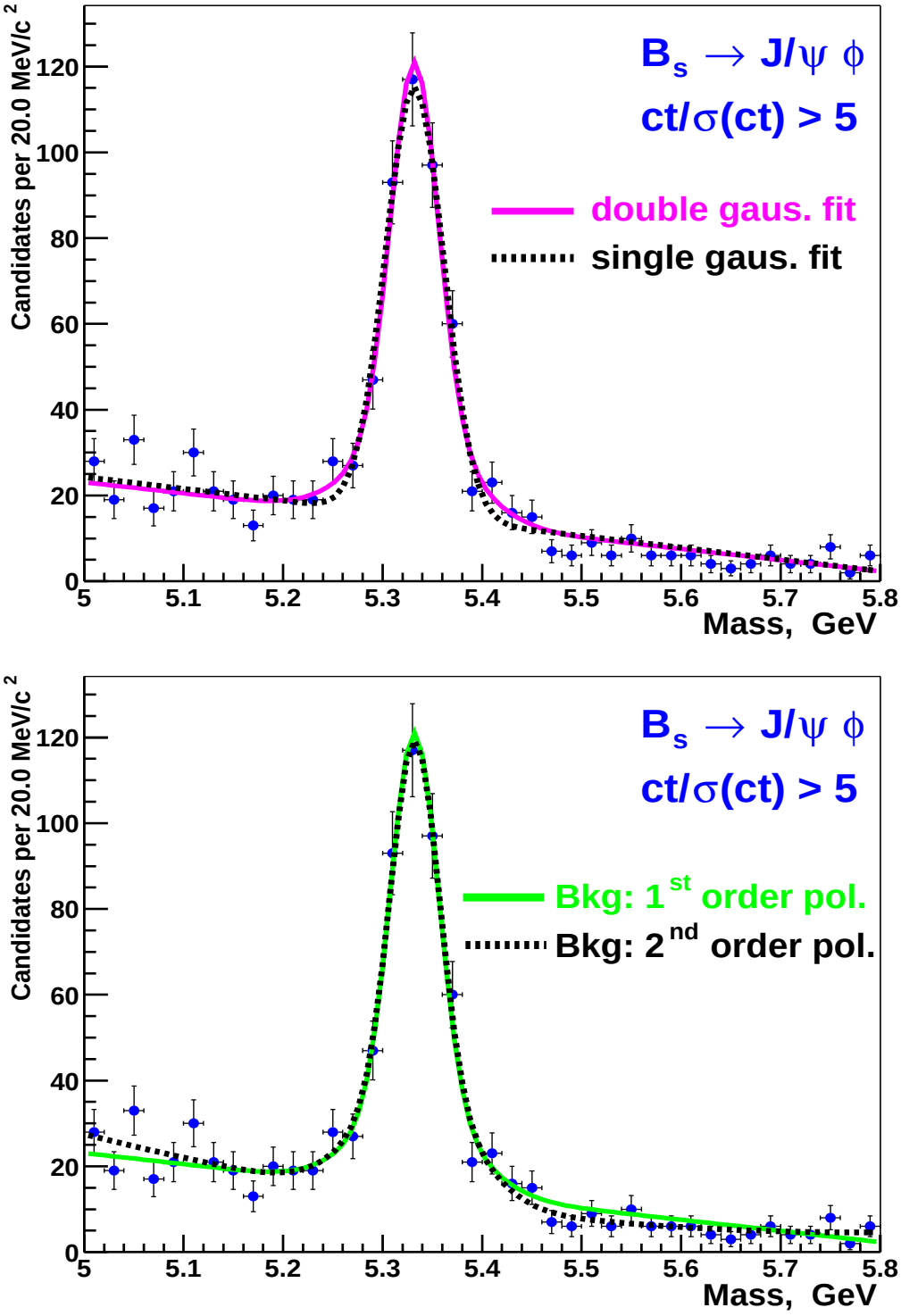

Figure 5.23: Upper: Fit projection of single-gaussian and double-gaussian with linear background. Lower: Fit projection of double-gaussian with 1^{st} order polynomial (linear background) and 2^{nd} order polynomial.

5.6 Cross Checks

The measurement of average lifetime and lifetime difference of the (B_s^0, $\overline{B}_s^0$) system carried out in this analysis is done for the first time at DØ. Being a complex analysis, we have performed several cross-checks to ensure the consistency of the results. We have found all cross-checks to be statistically consistent.

5.6.1 Cross Check with B_d^0 Data

The decay of $B_d^0 \to J/\psi(\to \mu^+\mu^-)K^*(\to K^\pm\pi^\mp)$ has a topology similar to that of $B_s^0 \to J/\psi(\to \mu^+\mu^-)\phi(\to K^+K^-)$ decay. With kinematic and quality cuts analogous to those listed in Section 5.2.2, we have 51106 B_d^0 candidates in the mass range of 4.9 – 5.7 GeV, out of which maximum likelihood fit assigns 1923±66 events due to the signal.

Due to relatively higher abundance of B_d^0 (because of higher fragmentation), measurement of equivalent physical quantities have less statistical uncertainty. These measurements on (B_d^0, $\overline{B_d^0}$) system are compared with other experimental results, which are known to a good accuracy. Similar to the (B_s^0, $\overline{B}_s^0$) system, we have also measured the lifetime and lifetime difference for (B_d^0, $\overline{B_d^0}$) system, which are described below in more detail. We find that measurement of physical quantities for (B_d^0, $\overline{B_d^0}$) system using DØ data, are in agreement with published results within statistical limit [12].

5.6.1.1 "2D" Fit

First we have performed a conventional "2D" fit to the B_d^0 candidate sample. The fit results are tabulated in Table 5.9. The B_d^0 mass distribution with the fit overlay is shown in Fig. 5.24 (left), while Fig. 5.24 (right) shows the same distribution after rejecting prompt background. The fitted average lifetime is 459 ± 13 (stat) μm[6], which is in agreement with

[6]DØ has published a result [73] 442±15 (stat)±7 (syst) μm for the B_d^0 lifetime based on a similar "2D" fit to a data sample approximately equivalent to 60% of the present data. One difference between our fit and that of [73] is the treatment of the background mass. Both analysis parametrize it as a linear shape,

world average value of 458 ± 2.7 μm. The proper decay length distribution with "2D fit" projection is shown in Fig. 5.26 (upper).

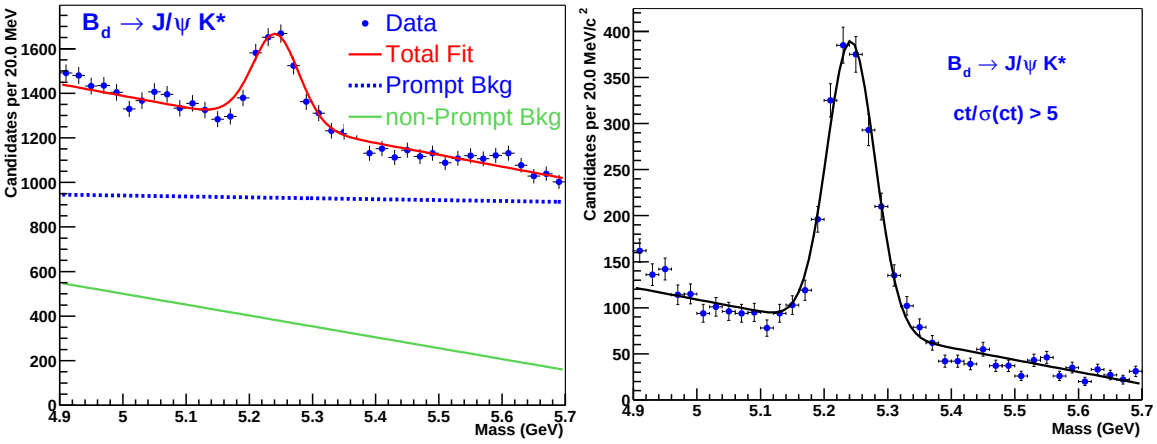

Figure 5.24: Left: The invariant mass distribution of all B_d^0 candidates, the curves are projections of the "2D" maximum likelihood fit. Right: Again the invariant mass distribution of the B_d^0 candidates with prompt background suppressed.

5.6.1.2 "3D free $\Delta\Gamma/\overline{\Gamma}$" fit

The full angular distribution of the 4-body final state for $B_d^0 \to J/\psi(\to \mu^+\mu^-)K^*(\to K^\pm\pi^\mp)$ is equivalent to the Eq. 2.21. In case of $B_s^0 \to J/\psi\phi$, the 3-angle to 1-angle (transversity) reduction with proper detector acceptance is given in Appendix A. However, for $B_d^0 \to J/\psi K^*$, due to the mass difference between the K^* decay products, the reduction of the 3-angle to 1-angle (transversity), is less straightforward.

The procedure for obtaining the angle-dependent acceptance distributions is described in Appendix A. The acceptance distributions for each angle are shown in Fig. A.2. As can be seen from these figures, detector acceptance is not uniform in the angle ψ (compare Fig. A.1-C and Fig. A.2-C), however it is reasonably flat for other two angles, which indicates in particular that response of the detector to angle θ and ψ may not be correlated. Due to

but contrary to [73], we allow for a separate slope for the prompt and non-prompt components, as they have different physical origin and behave differently.

this, as an approximation, we integrate 3-angle equation over angle ϕ and ψ, which result in following simple form (by neglecting non-uniform response of the detector to angle ψ):

$$\frac{d^2\Gamma[B_d^0(t) \to J/\psi K^*]}{d\cos\theta\ dt} \propto \Big[(1 - R_\perp(t))(1 + \cos^2\theta) + 2R_\perp(t)\sin^2\theta\Big]. \tag{5.13}$$

First, we have checked the effect of above approximation on pure CP-odd MC B_d^0 sample by subjecting reconstructed candidates events (11385) in this sample to the "3D free $\Delta\Gamma/\overline{\Gamma}$" fit. The fit assigns 10362(±37) signal events and other fit parameters are tabulated in Table 5.8. The fit returns $R_\perp$ = 0.994±0.006, which is in good agreement for the input value of 1. For this MC data sample, the mass distribution and transversity distribution plots with fit overlay are shown in Fig. 5.25.

The "3D free $\Delta\Gamma/\overline{\Gamma}$" fit results for experimental data sample of B_d^0 are shown in Table 5.9, and the fit projection on transversity distribution is shown in Fig. 5.26 (lower). Allowing for the (unphysical) difference in the time evolution of the CP-even and CP-odd terms, we obtain "$\Delta\Gamma/\overline{\Gamma}$" = -0.06±0.17, consistent with zero, as expected, and the CP-odd fraction ($R_\perp$) = 0.18±0.06, consistent with the CDF result of 0.215±0.032. In Fig. 5.26 (lower), we also show the fit projection of 1-angle formula (Eq. 5.13), on transversity distribution, with different values of $R_\perp$.

Index	Parameter	"3D free $\Delta\Gamma/\overline{\Gamma}$" fit
1, 2	f_{sig}, S	0.910±0.003, 1.15±0.05
3, 4	μ, σ_1 (MeV)	5277.4±0.3, 30.3±0.3
5, 6	$c\overline{\tau}$ (μm), $\Delta\Gamma/\overline{\Gamma}$	470±5, not used
7	$R_\perp$	0.994±0.006
8, 9	a_1, a_2	-0.91±0.19, not used
10, 11, 12	n_-, n_+, n_{++}	0.03±0.02, 0.96 ±0.02, not used
13, 14, 15	b_-, b_+, b_{++} (μm)	16±8, 194±18, not used
16, 17, 18&19	A_{12}, A_{14}, A_{22}&A_{24}	-1.6±0.18, 0.8±0.20, not used
18, 19	A_{22}, A_{24}	not used

Table 5.8: Maximum likelihood fitting results for the CP-odd MC sample of B_d^0 decay. The left hand parameter numbers corresponds to Table 5.3.

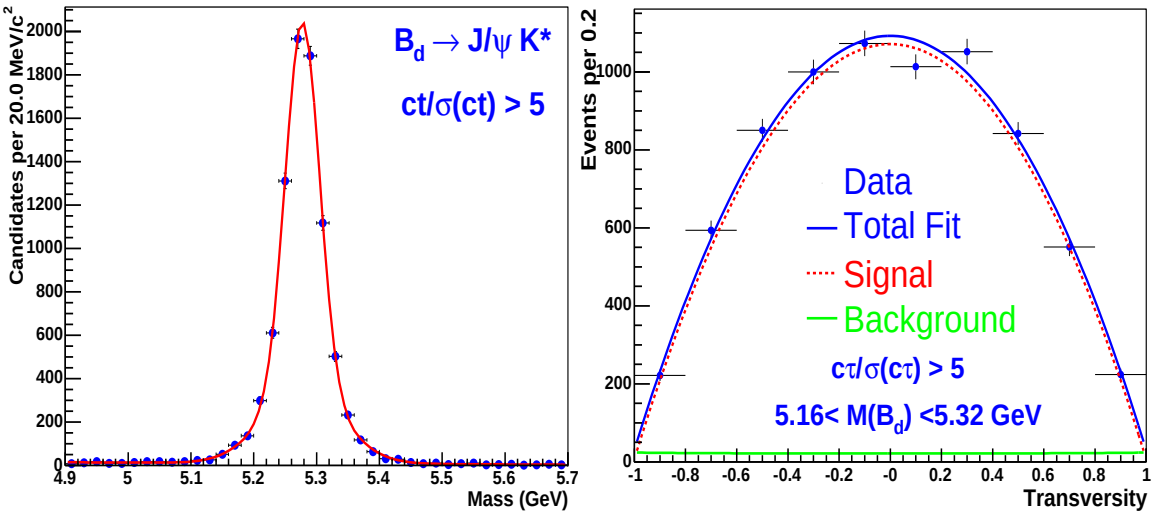

Figure 5.25: Mass and transversity distributions for CP-odd MC sample of B_d^0 decay.

Index	Parameter	"2D" fit	"3D free $\Delta\Gamma/\overline{\Gamma}$" fit
1	f_{sig}	0.0376±0.0013	0.0376±0.0013
2	S	1.32±0.01	1.32±0.01
3	μ (GeV)	5.242±0.001	5.242±0.001
4	σ_1 (MeV)	31.5±1.1	31.0±1.1
5	$c\overline{\tau}$ (μm)	459±13	457±16
6	$\Delta\Gamma/\overline{\Gamma}$	not used	-0.06±0.17
7	$R_\perp$	not used	0.18±0.06
8, 9	a_1, a_2	-0.06±0.03, -0.97±0.02	-0.04±0.03, -0.98±0.02
10, 11	n_-, n_+	0.056±0.005, 0.155±0.004	0.059±0.005, 0.157±0.004
12	n_{++}	0.032±0.002	0.032±0.002
13, 14	b_-, b_+ (μm)	50±2, 85±3	49±2, 83±3
15	b_{++} (μm)	424±21	421±21
16, 17	A_{12}, A_{14}	not used	1.16 ±0.09, -0.91 ±0.09
18, 19	A_{22}, A_{24}	not used	-0.09 ±0.13, 0.16 ±0.15

Table 5.9: Maximum likelihood fitting results for experimental data on B_d^0 decay. The left hand parameter numbers corresponds to Table 5.3.

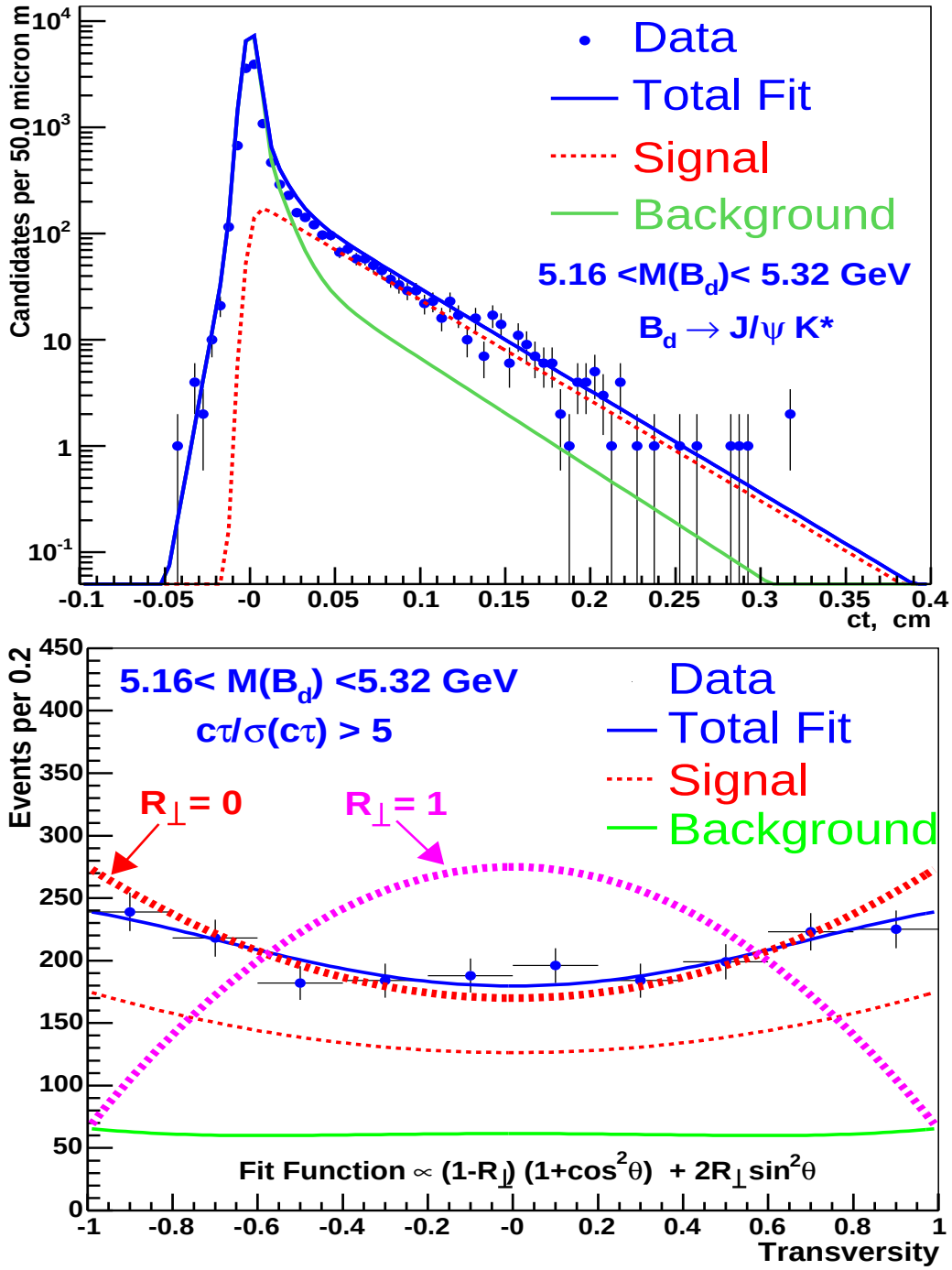

Figure 5.26: Upper: The proper decay length, ct, of the B_d^0 candidates in the signal mass region, with "2D" fit overlaid. Lower: The transversity distribution of signal-enhanced subsample (i.e. "non-prompt" and signal mass) B_d^0 candidates, with "3D free $\Delta\Gamma/\overline{\Gamma}$" fit overlaid. For illustration, fit projection of one angle formula at $R_\perp = 0$ and 1 are also shown (indicated by arrow).

5.6.2 Comparison of Results after Dividing Data in Two Half

As a test of the stability of the data, collected over long period of time, we divide the data into two sets (Round1→5 and Round6→8), each corresponding approximately to the integrated luminosity of 225 pb^{-1}. Same analysis is performed on these two sets.[7] We have compared the mass, transversity, and lifetime distributions of the B_s^0 candidates, and kinematic distributions of muons and J/ψ using Kolmogorov test. It is shown that the both data sets are compatible with each other within statistical fluctuations. Results from "3D free $\Delta\Gamma/\overline{\Gamma}$" maximum likelihood fit, performed on each data set for B_s^0 data sample, are summarized in Table 5.10. The 1-σ contour plots and the results of the likelihood scan as a function of $\Delta\Gamma/\overline{\Gamma}$ are compared in Fig. 5.27. The spread of the two contours further illustrates the correlation of the measured CP-average $c\overline{\tau}$ and $\Delta\Gamma/\overline{\Gamma}$. They are aligned approximately along a constant $c\tau_L$. The results from two halves of the data sets are statistically consistent and any difference between the central values of $\Delta\Gamma/\overline{\Gamma}$ and other physical parameters are of the order of 1-σ deviation.

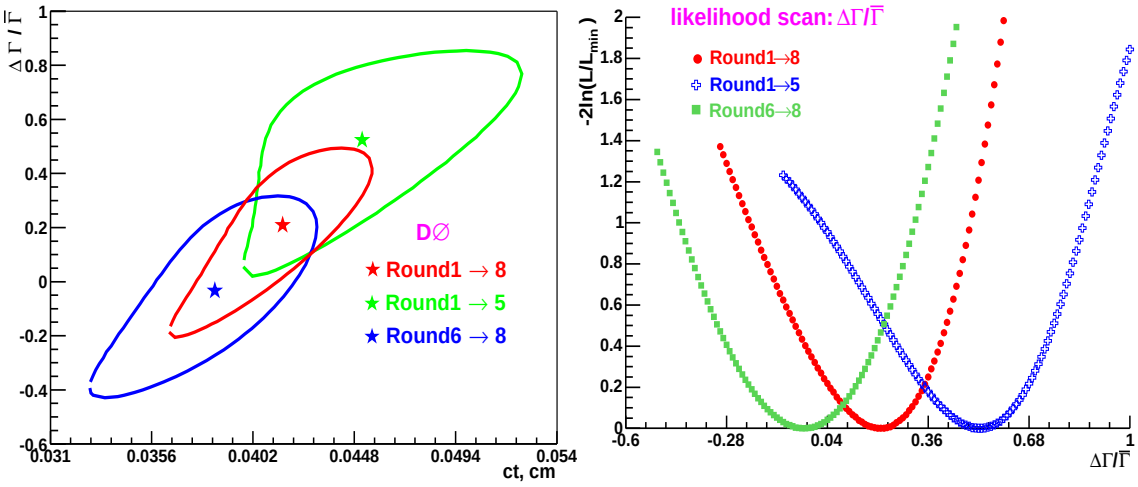

Figure 5.27: 1-σ contours and likelihood scan plots for "3D free $\Delta\Gamma/\overline{\Gamma}$" fit on B_s^0 sample of all data (Round1→8) and two half's of all data (Round1→5 and Round6→8). Left: the 1-σ contour for the fitted parameters $c\overline{\tau}$(cm) and $\Delta\Gamma/\overline{\Gamma}$. Right: likelihood scan for $\Delta\Gamma/\overline{\Gamma}$.

[7] In Appendix C we provide a detailed comparison of the results from both sets.

Index	Parameter	Rounds 1-8 (full sample)	Rounds 1-5	Rounds 6-8
1	f_{sig}	0.053±0.003	0.058±0.005	0.049±0.005
2	S	1.29±0.02	1.29±0.03	1.31±0.03
3	μ (GeV)	5.331±0.002	5.331±0.003	5.331±0.003
4	σ_1 (MeV)	22.5±1.5	22.9±2.2	22.5±2.2
5	$c\overline{\tau}$ (μm)	417^{+39}_{-48}	449±39	387±47
6	$\Delta\Gamma/\overline{\Gamma}$	$0.24^{+0.28}_{-0.38}$	0.52±0.29	0.01±0.37
7	$R_\perp$	0.16±0.10	0.09±0.07	0.28±0.16
8	a_1	0.12±0.09	0.15±0.13	0.03±0.10
9	a_2	-1.00±0.04	-0.93±0.07	-1.07±0.05
10, 11	n_-, n_+	0.07±0.01, 0.17±0.01	0.10±0.02, 0.18±0.02	0.04±0.02, 0.15±0.02
12	n_{++}	0.030±0.006	0.030±0.008	0.030±0.010
13, 14	b_-, b_+ (μm)	51±4, 89±7	44±4, 83±9	69±14, 98±11
15	b_{++} (μm)	422±55	435±79	411±74
16	A_{12}	1.00±0.20	1.30±0.43	0.98±0.30
17	A_{14}	-0.67±0.22	-0.89±0.45	-0.61±0.32
18	A_{22}	0.62±0.33	-0.07±0.55	1.36±0.76
19	A_{24}	-0.65±0.36	0.02±0.60	-1.34±0.81

Table 5.10: Results for "3D free $\Delta\Gamma/\overline{\Gamma}$" fit on B_s^0 sample of all data (Round1→8) and two half's of all data (Round1→5 and Round6→8). The left hand parameter numbers corresponds to Table 5.3.

As another test of the stability and comparison of results for average lifetime measurement, we divided all data ($R1 \rightarrow R8$) into four statistically equivalent subsets (R1→R5(1^{st} half), R1→R5(2^{nd} half), R6 and R7&R8), across the running period. We have performed "2D" maximum likelihood fit, to each subset and obtained average lifetime for B_s^0 and B_d^0 decays. These results are shown in the upper panel of Fig. 5.28, which shows the stability of data over the entire period.

5.6.3 "poor man's" estimate of $c\tau_L$

As can be seen from Fig. 5.9, high transversity ($|cos\theta|$) region is dominated by CP-even state, therefore if we measure the lifetime using the events in this region they would roughly corresponds to τ_L. We have explored this feature by dividing the full sample into three

statistically equivalent and non-overlapping regions, i.e. $|\cos(\theta)| > 0.75$, $0.5 < |\cos(\theta)| < 0.75$, and $|\cos(\theta)| < 0.5$, and performed a "2D" maximum likelihood fit on each subsample. Fitted lifetime for each subsample are plotted in Fig. 5.28 (lower panel), a straight-line fit gives $c\tau$=361±40μm, which is an estimate of a pure CP-even B_s^0 lifetime. This result can be interpreted as a "poor man's" estimate of $c\tau_L$, to be compared with 372^{+37}_{-32} μm we obtain from "3D free $\Delta\Gamma/\overline{\Gamma}$" maximum likelihood fit.

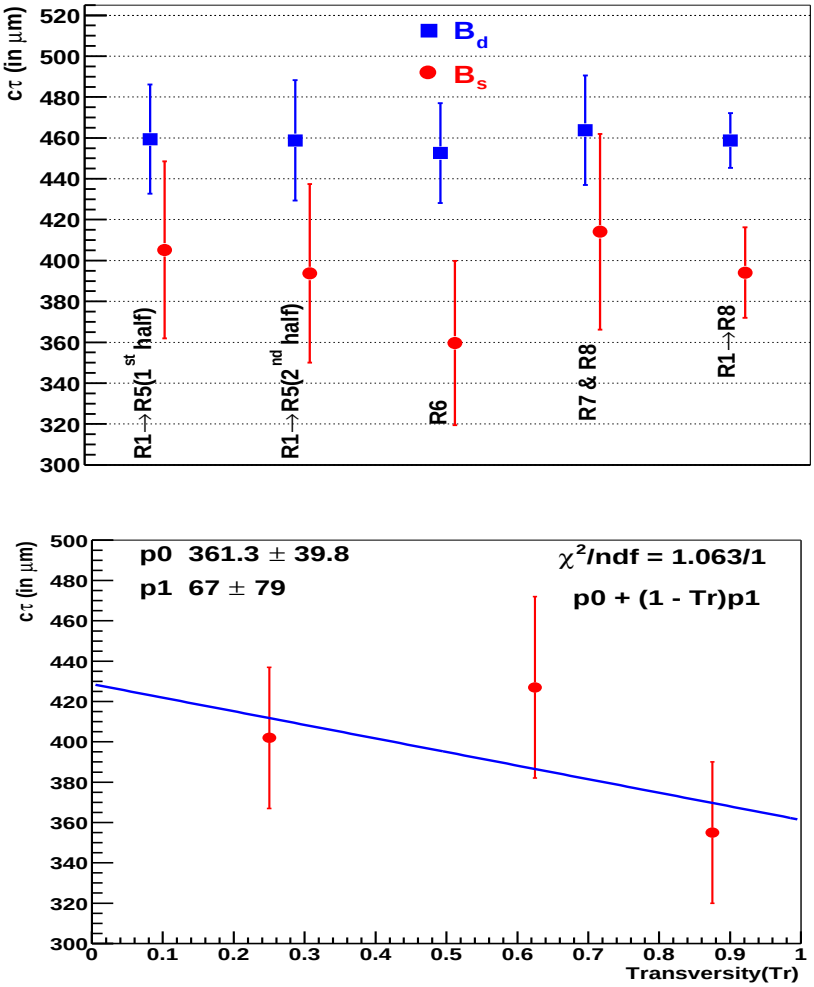

Figure 5.28: Upper: Average lifetime of the B_s^0 and B_d^0 decays for four subsets of data, obtained by performing "2D" maximum likelihood fit. Lower: Maximum likelihood "2D" fit results for three transversity bins.

5.6.4 Ensemble Test

We have conducted a test with an ensemble of 1000 pseudo-experiments with similar statistical sensitivity, tossed with the same parameters as obtained in this analysis, i.e. with the parameters listed in the first column of Table 5.4. Fig. 5.29 shows the scatter plot of the fitted values of $\Delta\Gamma/\overline{\Gamma}$ and $c\overline{\tau}$, along with the 1-σ contour and the central point obtained in this analysis. In about 11% of experiments $\Delta\Gamma/\overline{\Gamma}$ fell below -0.4. About 5% of experiments return $\Delta\Gamma/\overline{\Gamma} > 0.65$, above the CDF value.

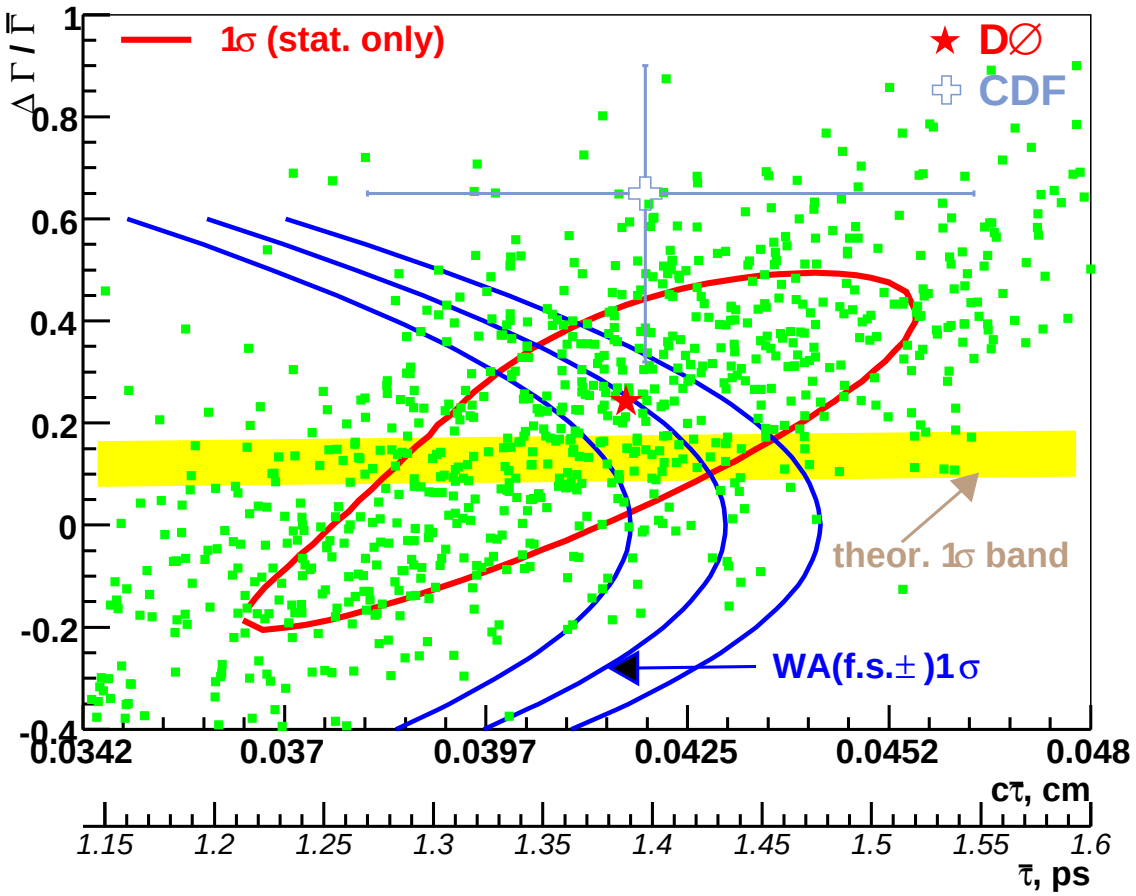

Figure 5.29: The scatter plot of the fitted values of $\Delta\Gamma/\overline{\Gamma}$ and $c\overline{\tau}$(cm) for an ensemble of 1000 simulated experiments.

Fig. 5.30 shows the distribution of fitted values and their errors for $R_\perp$, $c\overline{\tau}$, and $\Delta\Gamma/\overline{\Gamma}$. We find these distributions to be consistent with the input. The observed skewness of the distributions is consistent with the parameter correlation and the associated asymmetry of their errors.

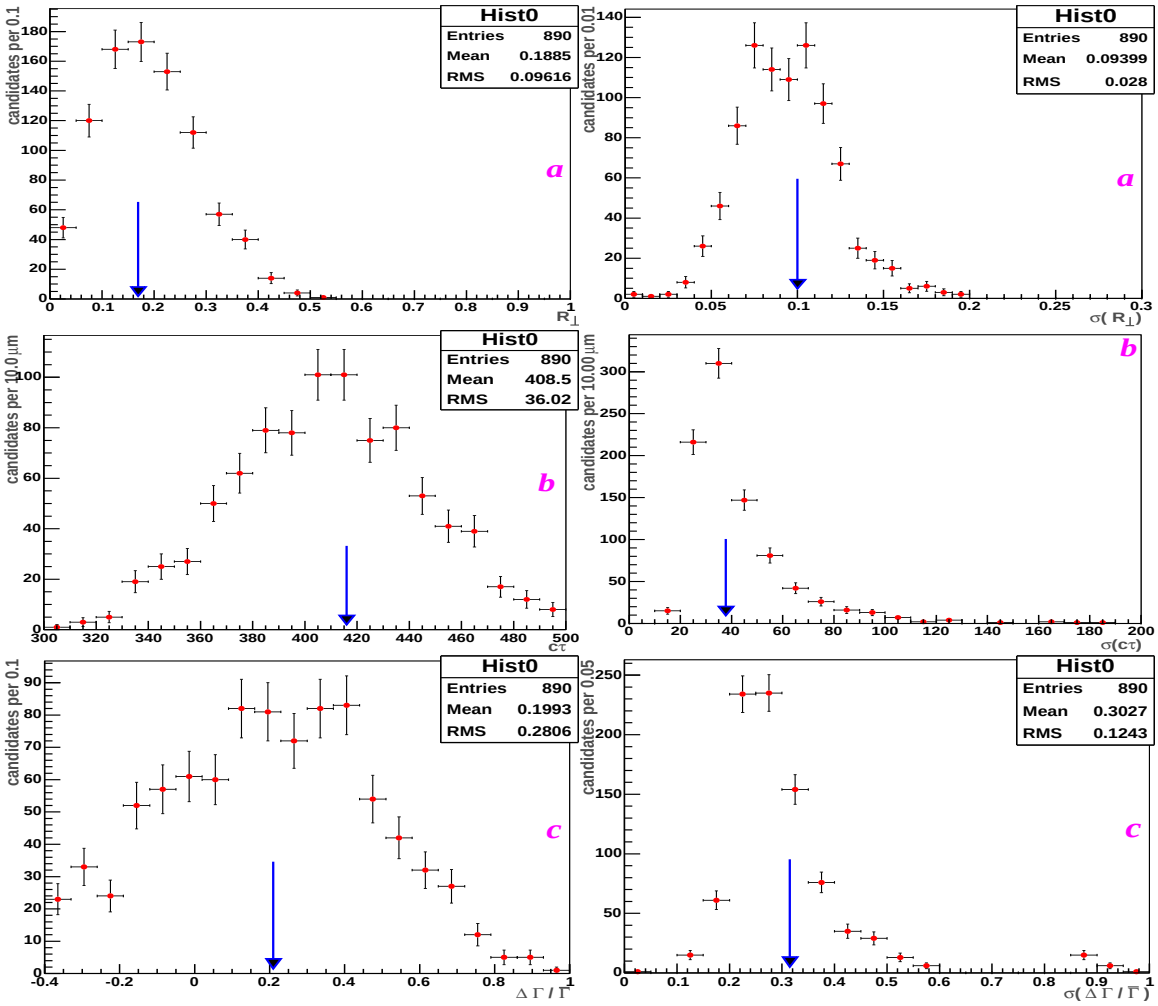

Figure 5.30: Distribution of fit parameters (left Figures) and error on fit parameters (right Figures) for (a) $R_\perp$, (b) $c\tau$ and (c) $\Delta\Gamma/\overline{\Gamma}$. The arrow indicates the fitted value we obtain from data by "3D free $\Delta\Gamma/\overline{\Gamma}$" fit.

Chapter 6

Summary

In this chapter, we summarize the main results we obtain in this analysis. Measurements of the lifetime difference and other parameters of the (B_s^0, $\overline{B}_s^0$) system provide a good test of standard model (SM) predictions and a probe of new physics. In the SM, the two physical eigenstates of known (B_s^0, $\overline{B}_s^0$) system, known as "light" and "heavy" mass eigenstates, to a good approximation coincide with CP states, such that the "light" corresponds to CP-even and "heavy" corresponds to the CP-odd. Time dependent angular analysis of $B_s^0 \to J/\psi(\to \mu^+\mu^-)\phi(\to K^+K^-)$ provides an elegant and independent way of separating these two states. The decay amplitude of $B_s^0 \to J/\psi\phi$ can be written in terms of time dependent linear polarization states of the vector mesons (J/ψ and ϕ). In the so called "transversity basis" decay amplitude depends on three polar angles, out of which, the crucial variable that separates the two mass eigenstates is called "transversity". Its use allows for simultaneous measurements of the decay width ($1/\tau$) of the "heavy" and the "light" mass eigenstates.

The upgraded DØ detector with its new tracking system and wide muon coverage, has served as an excellent facility to do $B-$physics. Analysis of 450 pb^{-1} of data has resulted in 9699 B_s^0 candidates with final event selection cuts described in section 5.2.2. Unbinned maximum likelihood fit using mass, lifetime and transversity of B_s^0 candidates, has been performed, which assigns 513$\pm$33 B_s^0 signal events in the data. A summary of the final results of this analysis is given below:

6.1 Results without External Constraints

We began with lifetime measurements of the $B_s^0(\rightarrow J/\psi\phi)$ decay with single exponential fit (without separating CP-even and CP-odd states or "2D fit"). We have measured lifetime for the fully exclusive $B_s^0(\rightarrow J/\psi\phi)$ decays to be:

$$\tau(B_s^0)_{J/\psi\phi} = 1.307 \pm 0.07 \text{ (stat)} \pm 0.02 \text{ (syst) ps.}$$

A comparison plot of lifetime of B_s^0 for its decays to the $J/\psi\phi$ final state is shown in Fig. 6.1. Compilation by Heavy Flavor Averaging Group (HFAG) and values of B_s^0 lifetime as measured by other experiments are taken from the Ref. [12].

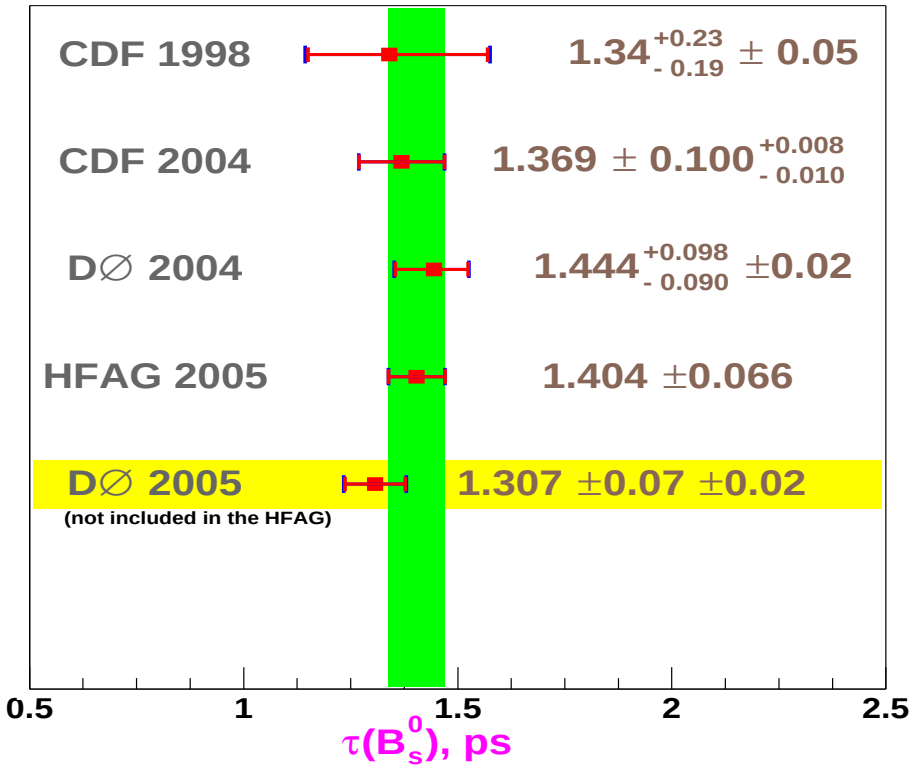

Figure 6.1: Comparison of B_s^0 lifetime from exclusive $B_s^0 \rightarrow J/\psi\phi$ decays, measured by single exponential fit ("2D fit") to the data, for more details, see [12].

This analysis was followed by a time dependent angular analysis of $B_s^0 \to J/\psi\phi$ which separates the CP-even and CP-odd states using the "transversity" variable. We have measured the CP-odd fraction for the $B_s^0(\to J/\psi\phi)$ decays, and the correlated parameters of the average lifetime of the $(B_s^0,\ \overline{B}_s^0)$ system (i.e. $\overline{\tau}(B_s^0) = 1/\overline{\Gamma}$)[1], and the relative width difference (i.e. $\Delta\Gamma/\overline{\Gamma}$) or, equivalently, the mean lifetimes of the "light" and "heavy" eigenstates (i.e. τ_L and τ_H) of $(B_s^0,\ \overline{B}_s^0)$ system. For the default fit (referred as "3D free $\Delta\Gamma/\overline{\Gamma}$") we obtain:

$$R_\perp = 0.16 \pm 0.10\ (\text{stat}) \pm 0.02\ (\text{syst}),$$

$$\Delta\Gamma/\overline{\Gamma} = 0.24^{+0.28}_{-0.38}\ (\text{stat})\ ^{+0.03}_{-0.04}\ (\text{syst}),$$

$$\overline{\tau}(B_s^0) = 1.39^{+0.13}_{-0.16}\ (\text{stat})\ ^{+0.01}_{-0.02}\ (\text{syst})\ \text{ps},$$

$$\tau_L = 1.24^{+0.14}_{-0.11}\ (\text{stat})\ ^{+0.01}_{-0.02}\ (\text{syst})\ \text{ps},$$

$$\tau_H = 1.58^{+0.39}_{-0.42}\ (\text{stat})\ ^{+0.01}_{-0.02}\ (\text{syst})\ \text{ps}.$$

Our results are consistent with previously published results [12]. Comparisons with other measurements are presented in Table 6.1. Comparison plot of the measurement of $\Delta\Gamma/\overline{\Gamma}$ from various experiments is shown in Fig. 6.2, while that for average lifetime is shown in Fig. 6.3.

Experiment	$R_\perp$	$\Delta\Gamma/\overline{\Gamma}$	$\overline{\tau}(ps)$	τ_L (ps)	τ_H (ps)
Aleph				1.27 ± 0.34	
CDF Run II	0.125 ± 0.08	$0.65^{+0.25}_{-0.33} \pm 0.01$	$1.40^{+0.15}_{-0.13}$	$1.05^{+0.16}_{-0.13}$	$2.07^{+0.58}_{-0.46}$
DØ RunII	0.16 ± 0.10	$0.24^{+0.28}_{-0.38}$	$1.39^{+0.13}_{-0.16}$	$1.24^{+0.14}_{-0.11}$	$1.58^{+0.39}_{-0.42}$

Table 6.1: Comparison of the existing direct measurements of various physical quantities characterizing $B_s^0 \to J/\psi\phi$ decay.

We have also measured the mean lifetime of the B^0 (or B_d^0) meson using its $B_d^0 \to J/\psi K^*$

[1]Note that, this average lifetime ($\overline{\tau}(B_s^0)$) is different from lifetime ($\tau(B_s^0)$) which we get from single exponential fit.

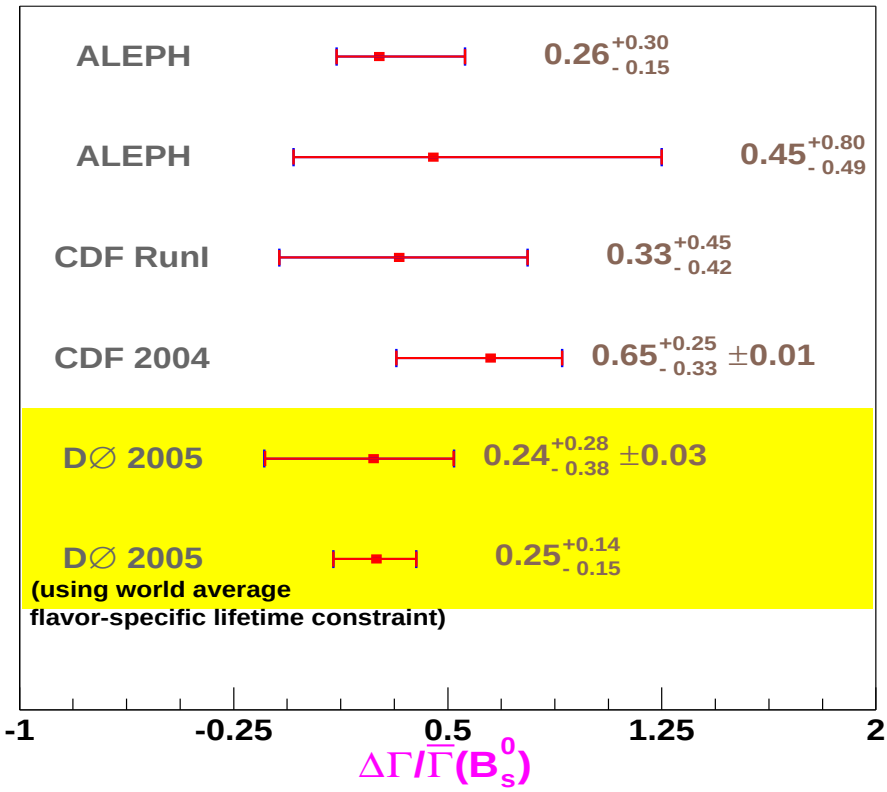

Figure 6.2: Comparison of $\Delta\Gamma/\overline{\Gamma}$ measurement from various experiments (ALEPH [74] and CDF RunI [75] results are indirect measurements).

decay mode, with double the statistics as compared to the DØ data published in 2004 [73]. When corresponding event selection criteria are used, we have 51106 B_d^0 candidates in total, out of which maximum likelihood fit assigns 1923±66 events as being due to the signal. The updated measurement of the mean lifetime is:

$$\tau(B^0) = 1.530 \pm 0.043 \text{ (stat)} \pm 0.023 \text{ (syst) ps.}$$

Comparison plot of B^0 lifetimes as measured by different experiments is shown in Fig. 6.4. For the ratio of the average B_s^0 lifetime to the B^0 lifetime, we obtain:

$$\frac{\overline{\tau}(B_s^0)}{\tau(B^0)} = 0.91 \pm 0.09 \text{ (stat)} \pm 0.003 \text{ (syst).}$$

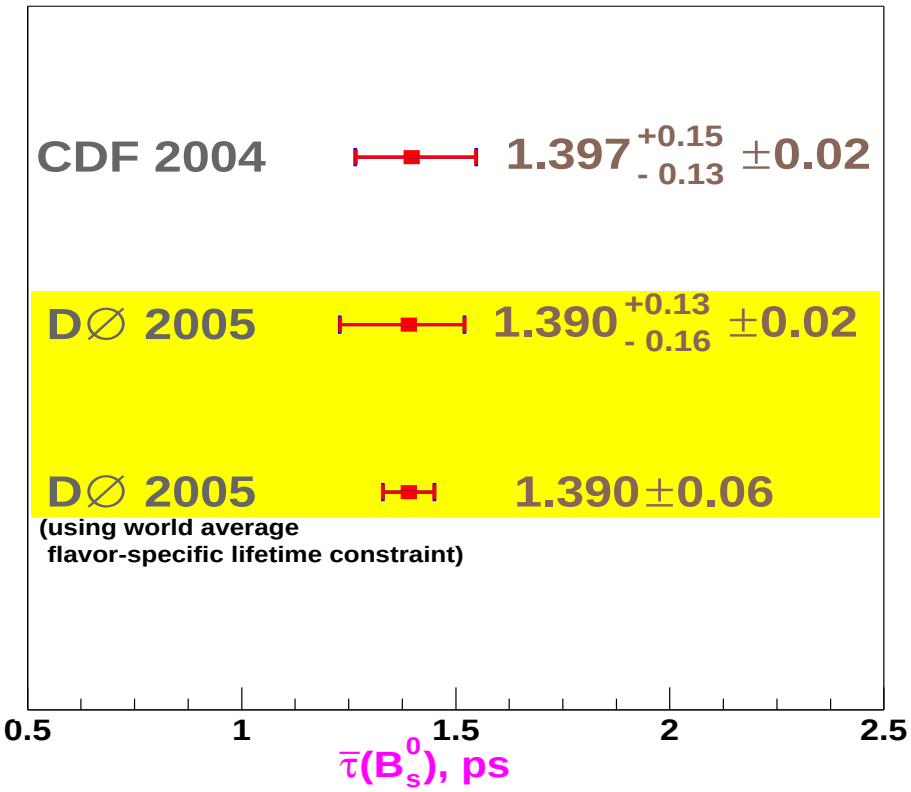

Figure 6.3: Comparison of measured average lifetime of $B_s^0 \to J/\psi\phi$ (i.e. $\overline{\tau}(B_s^0)_{J/\psi\phi}$). So far only DØ and CDF experiments have made the direct measurement.

6.2 Results Constrained by Semileptonic Measurements

Using our results for $\Delta\Gamma/\overline{\Gamma}$ and $\overline{\tau}(B_s^0)$, and applying a constraint on this pair of parameters from the existing semileptonic (i.e. flavor-specific) measurements [23], we obtain:

$$\overline{\tau} = 1.39 \pm 0.06 \ \text{ps},$$

$$\Delta\Gamma/\overline{\Gamma} = 0.25^{+0.14}_{-0.15}.$$

Comparison with other measurements is shown in Fig. 6.2 and in Fig. 6.3.

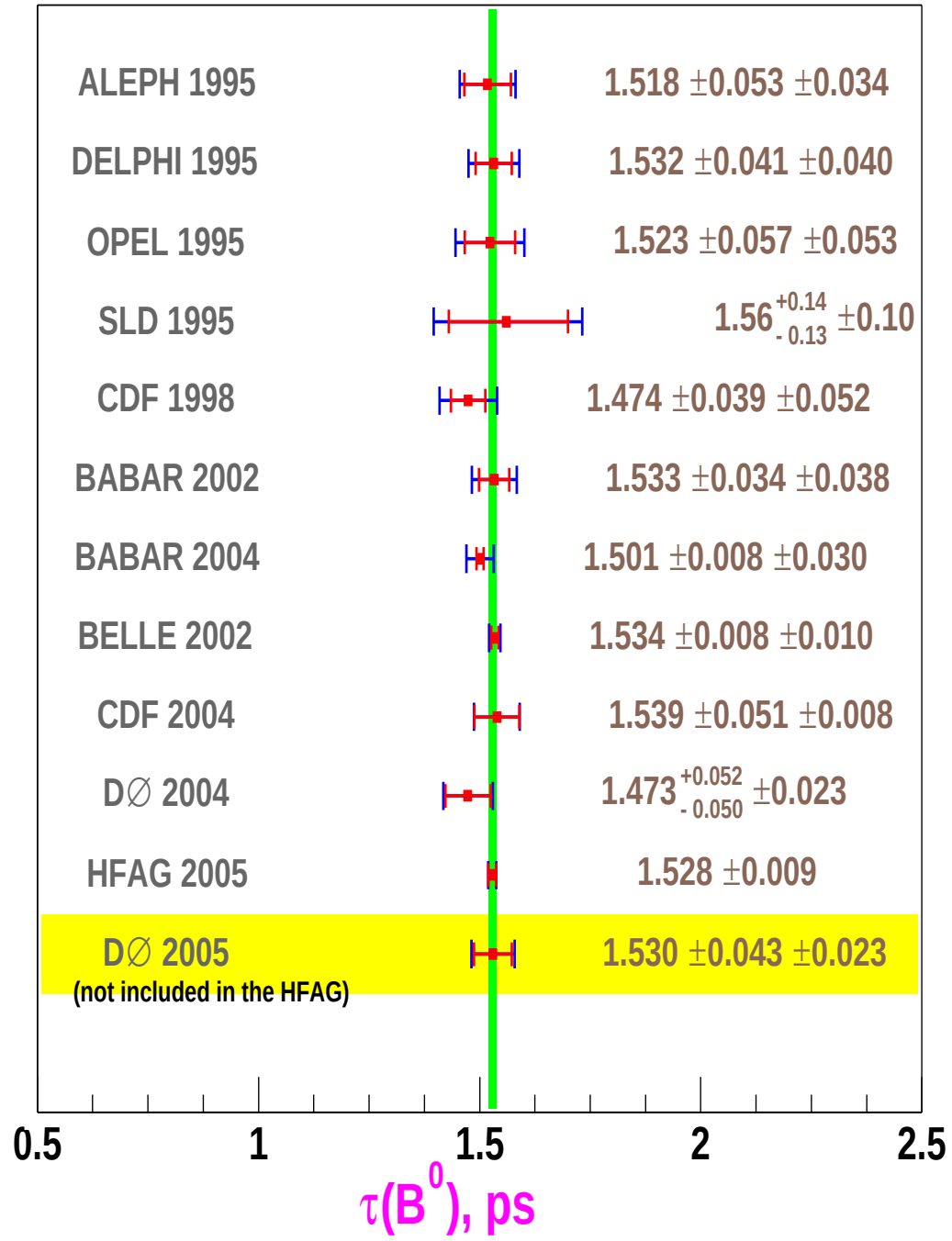

Figure 6.4: Comparison of B^0 lifetime from various experiments. See [12] for HFAG average.

6.3 Conclusion and Future Prospects

All the results presented above are obtained under a tacit assumption that the CP-violating phase is negligible, as predicted by the SM ($\delta\phi = \phi_{\rm CKM} = -0.03$). Although above measurements contribute to an understanding of the (B_s^0, $\overline{B}_s^0$) system, current sensitivity is not enough to reach any final conclusion. This warrants further improvements on the measurement of $\Delta\Gamma/\overline{\Gamma}$ in future, which may exclude models predicting large deviations of $\delta\phi$ from the SM value.

In the current analysis we have 513±33 signal events in 450 pb^{-1} of data. We have carried out Monte Carlo studies of prospects for the B_s^0 lifetime difference measurement with more data, and generated approximately 9000 fully simulated signal events, (with fixed $\Delta\Gamma/\overline{\Gamma}$ of 0.22) passing the final event selection cuts. Maximum likelihood fits have been performed on them. We have done projections of $\sigma(\Delta\Gamma/\overline{\Gamma})$ as a function of the integrated luminosity. The projected accuracy for 8 fb^{-1} is ±0.04 (see Fig. 6.5). This is comparable to the theoretical accuracy. The $\Delta\Gamma/\overline{\Gamma}$ measurement with such an accuracy would be an important input to the study of the CP-violating effects and new phenomenon contributions to the $B_s^0 - \overline{B_s^0}$ mixing.

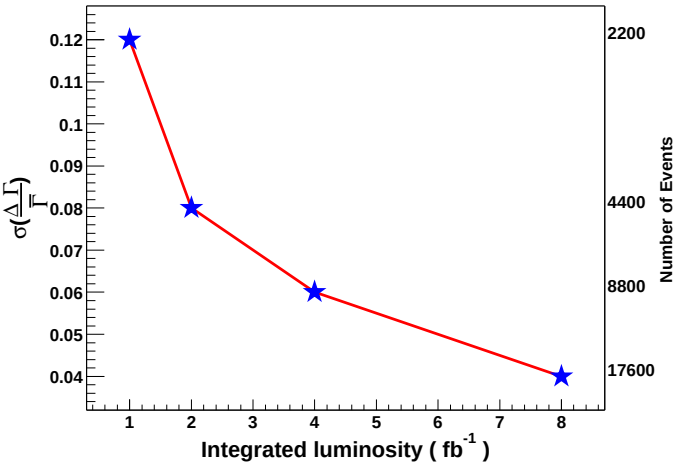

Figure 6.5: Projected measurement uncertainty on $\Delta\Gamma/\overline{\Gamma}$ with increasing luminosity.

Appendix A

Effect of the detector acceptance on the angular distribution

Due to limited detector coverage and kinematic thresholds, the distribution of three angles in transversity basis in the reconstructed MC data sample is not same as seen at the generator level, which indicates that there is an angle-dependent acceptance of the detector. To find this acceptance, we have used the CP-even MC data sample, which is passed though the complete simulation cycle upto the reconstruction level. The angle-dependent acceptance for a given angle is then obtained by taking the ratio of the associated angle distribution at reconstruction level and generator level. The distribution of the relative acceptance for each angle is shown in Fig. A.1.

To account for the angle-dependent acceptance, we parametrized each acceptance distribution with an empirical function (called $F(\phi)$, $G(\theta)$, and $H(\Psi)$), which are multiplied to the right hand side of the 3-angle distribution given by Eq. 2.21, and this 3-angle distribution is integrated over two angles (Ψ and ϕ), to get final 1-angle distribution. The empirical functions fitted to the curves in Figs. A.1 are of the form:

$$\begin{aligned} \mathrm{F}(\phi) &= 1 + \mathrm{J}\ \cos(2\phi) + \mathrm{K}\ \cos^2(2\phi), \\ \mathrm{G}(\cos\theta) &= 1 + \mathrm{B}\ \cos^2\theta + \mathrm{C}\ \cos^4\theta, \qquad \text{and} \\ \mathrm{H}(cos\Psi) &= 1. \end{aligned}$$

The fitted values of the acceptance parameters are: $B = 0.41 \pm 0.10$, $C = -0.27 \pm 0.14$, $J = -0.100 \pm 0.008$, and $K = -0.156 \pm 0.016$. As we have $H(cos\Psi) = 1$, the acceptance is independent of the angle Ψ. Integration of the three-angle Eq. 2.21 (with acceptance functions), over Ψ leads to the following two-angle distribution:

$$\frac{d^3\mathcal{A}}{d\cos\theta\ d\varphi\ dt} = N\Big[|A_0(t)|^2(1-\sin^2\theta\cos^2\varphi)$$

$$+ |A_{\parallel}(t)|^2(1-\sin^2\theta\sin^2\varphi) \; + |A_{\perp}(t)|^2\sin^2\theta \; - \; \mathrm{Im}\;(A^*_{\parallel}(t)A_{\perp}(t))\sin 2\theta\sin\varphi\Big]F(\phi)\; G(cos\theta)$$

Inserting $F(\phi)$, and integration over ϕ leads to[1]:

$$\begin{aligned}\frac{d^2\mathcal{A}}{d\cos\theta\; dt} &= N\pi\Big[(|A_0(t)|^2+|A_{\parallel}(t)|^2)(1+cos^2\theta)\\ &+\frac{K}{2}\Big\{(|A_0(t)|^2+|A_{\parallel}(t)|^2)(1+cos^2\theta)+2|A_{\perp}(t)|^2\sin^2\theta\Big\}\\ &-\frac{J}{2}(|A_0(t)|^2-|A_{\parallel}(t)|^2)sin^2\theta \quad +2|A_{\perp}(t)|^2\sin^2\theta \;\;\Big]G(cos\theta)\end{aligned} \tag{A.1}$$

Inserting $G(cos\theta)$ into Eq. A.1, and integration over $cos\theta$ leads to:

$$\begin{aligned}\frac{d\mathcal{A}}{dt} &= 8N\pi\Big[(|A_0(t)|^2+|A_{\parallel}(t)|^2)\Big(\frac{1}{3}+\frac{2B}{15}+\frac{3C}{35}\Big)\\ &+\frac{K}{2}\Big\{(|A_0(t)|^2+|A_{\parallel}(t)|^2)\Big(\frac{1}{3}+\frac{2B}{15}+\frac{3C}{35}\Big)+|A_{\perp}(t)|^2\Big(\frac{1}{3}+\frac{B}{15}+\frac{C}{35}\Big)\Big\}\\ &-\frac{J}{4}\Big\{(|A_0(t)|^2-|A_{\parallel}(t)|^2)\Big(\frac{1}{3}+\frac{B}{15}+\frac{C}{35}\Big)\Big\} \quad +|A_{\perp}(t)|^2\Big(\frac{1}{3}+\frac{B}{15}+\frac{C}{35}\Big) \;\;\Big]\end{aligned} \tag{A.2}$$

Eq. A.2 is used for finding normalization constant N, where as Eq. A.1 is used for defining, the signal proper decay length and transversity probability distribution function.

For $B^0_d \to J/\psi K^*$ the angle-dependent acceptance distributions were obtained from CP-odd MC data sample using the same procedure as describe before. These distributions are shown in Fig. A.2, and are different from what we get in case of $B^0_s \to J/\psi\phi$ (Fig. A.1), due to different final decay products. The acceptance is more or less flat for the angle θ and ϕ, where as for angle Ψ, it reduces with increasing Ψ. This makes it difficult to find out appropriate parametrization, to obtain 1-angle formula as has been done for the B^0_s decay.

[1]If we negelect detector acceptance effect, i.e. J=K=B=C=0 or F(ϕ)=G(cosθ)=1, we get back Eq. 2.25 from section 2.5 of chaper 2.

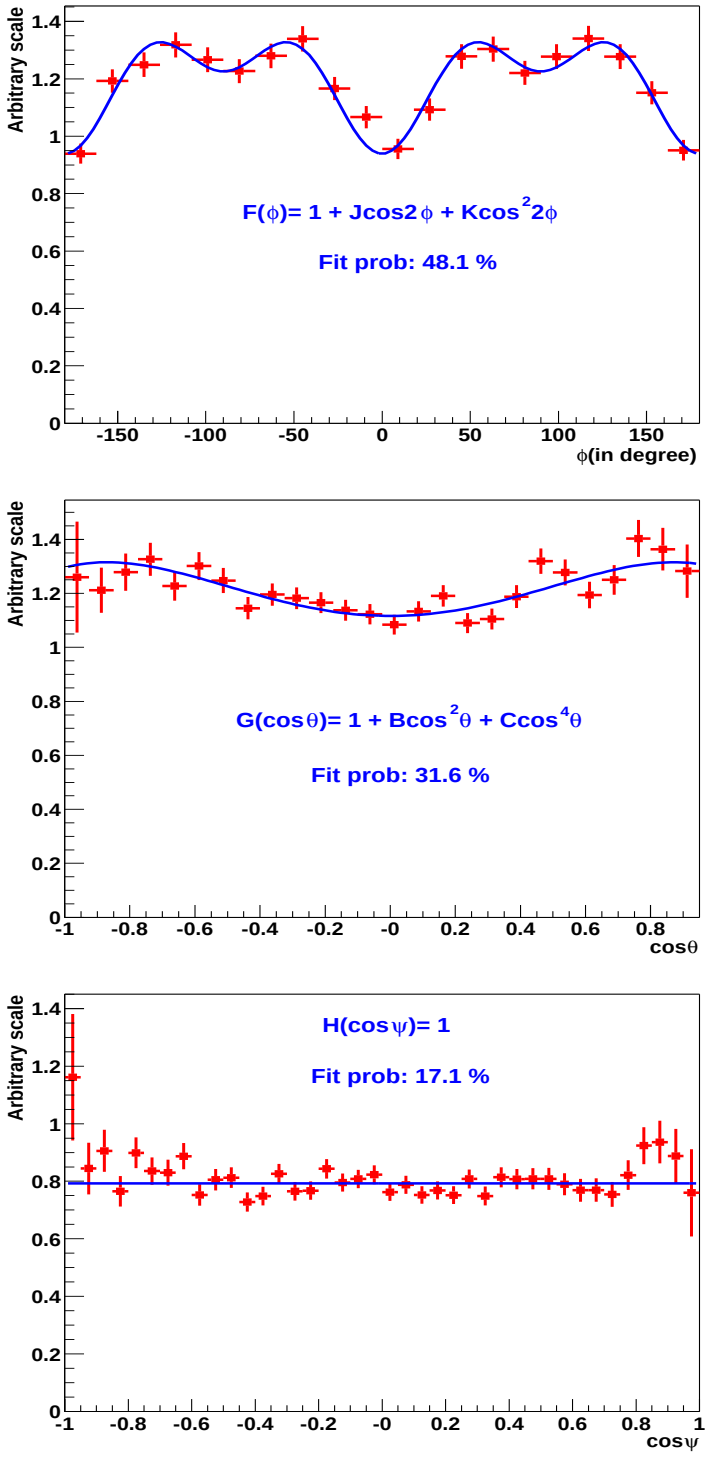

Figure A.1: The Acceptance distribution for B_s^0 MC events. A. for angle ϕ B. transversity angle cosθ and, C. for cosΨ.

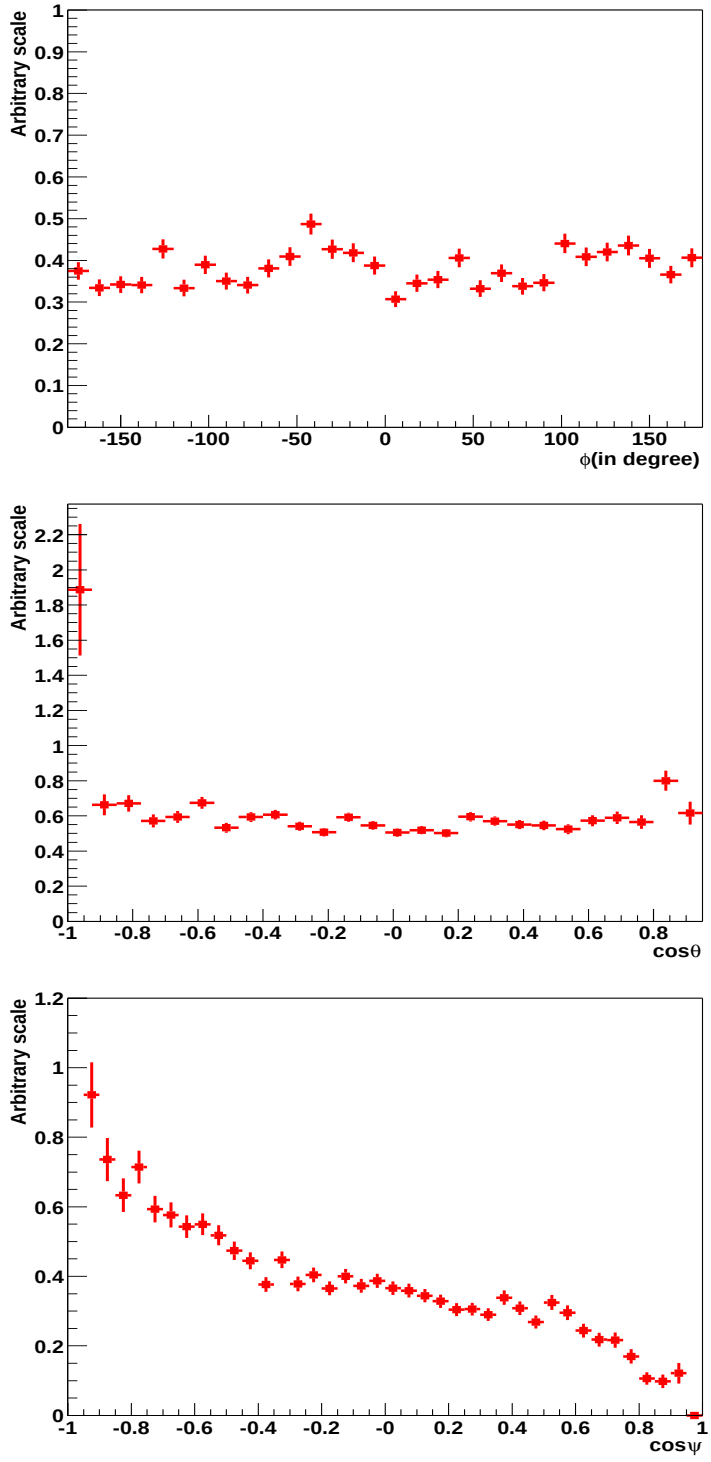

Figure A.2: The Acceptance distribution for B_d^0 MC events. A. for angle ϕ B. transversity angle cosθ and, C. for cosΨ.

Appendix B

MC Signal - data matching

Comparison of kinematic spectra of Monte Carlo (MC) and data objects (leading muons, trailing muons, J/ψ, leading kaons, trailing kaons, ϕ and B_s^0), shows that MC objects are softer. To correct this difference, kinematic spectra of the MC objects are weighted separately in the central and forward region, using weight factors, obtained by forcing the p_T spectra of MC J/ψ particle to agree with the data. The same weight factors are then used for weighting the rest of the MC objects the in central and forward region respectively. Following 14 figures show the p_T distributions of the objects in the central and forward regions, before and after applying the weight factor. From the right hand side figures it is clear that the weighted MC distributions are in a good agreement with experimental data.

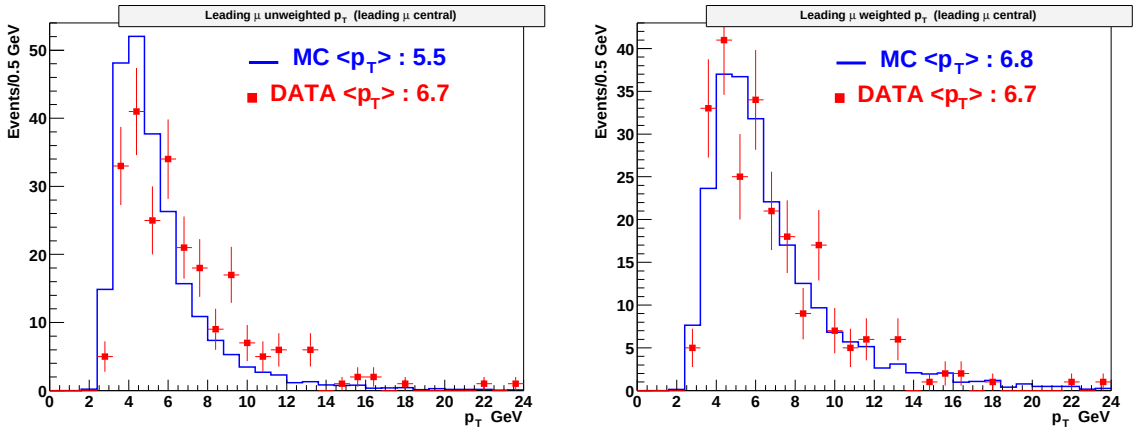

Figure B.1: p_T distribution of the leading muon in the central rapidity region, in data (points) and MC (solid histogram) uncorrected (left); corrected(right).

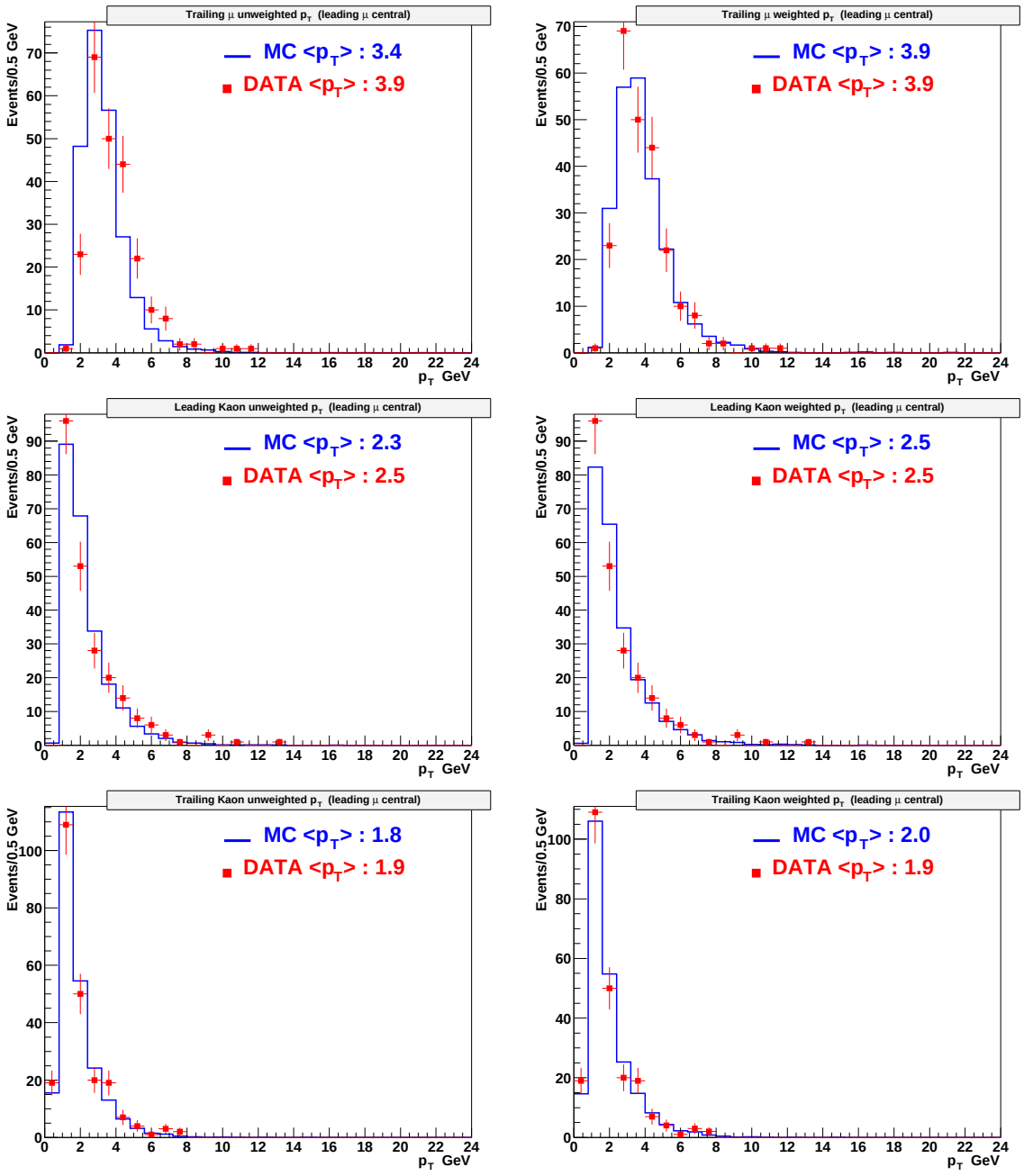

Figure B.2: p_T distribution of the trailing muon (top) leading kaon (middle) and the trailing kaon (bottom) in the central rapidity region, in data (points) and MC (solid histogram) uncorrected (left); corrected(right).

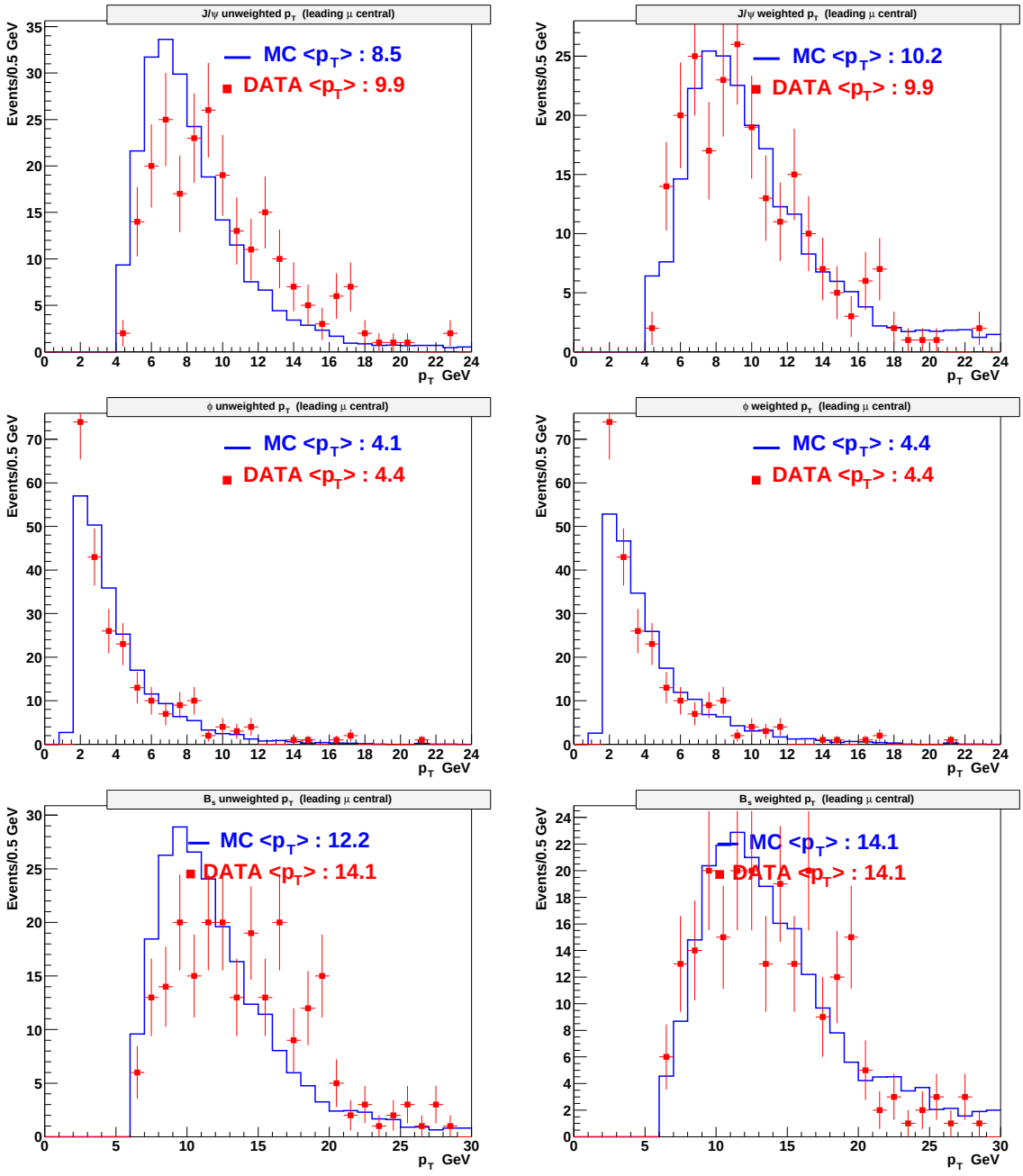

Figure B.3: p_T distribution of J/ψ (top), ϕ (middle), and B_s (bottom), in the central rapidity region, in data (points) and MC (solid histogram) uncorrected (left); corrected(right)

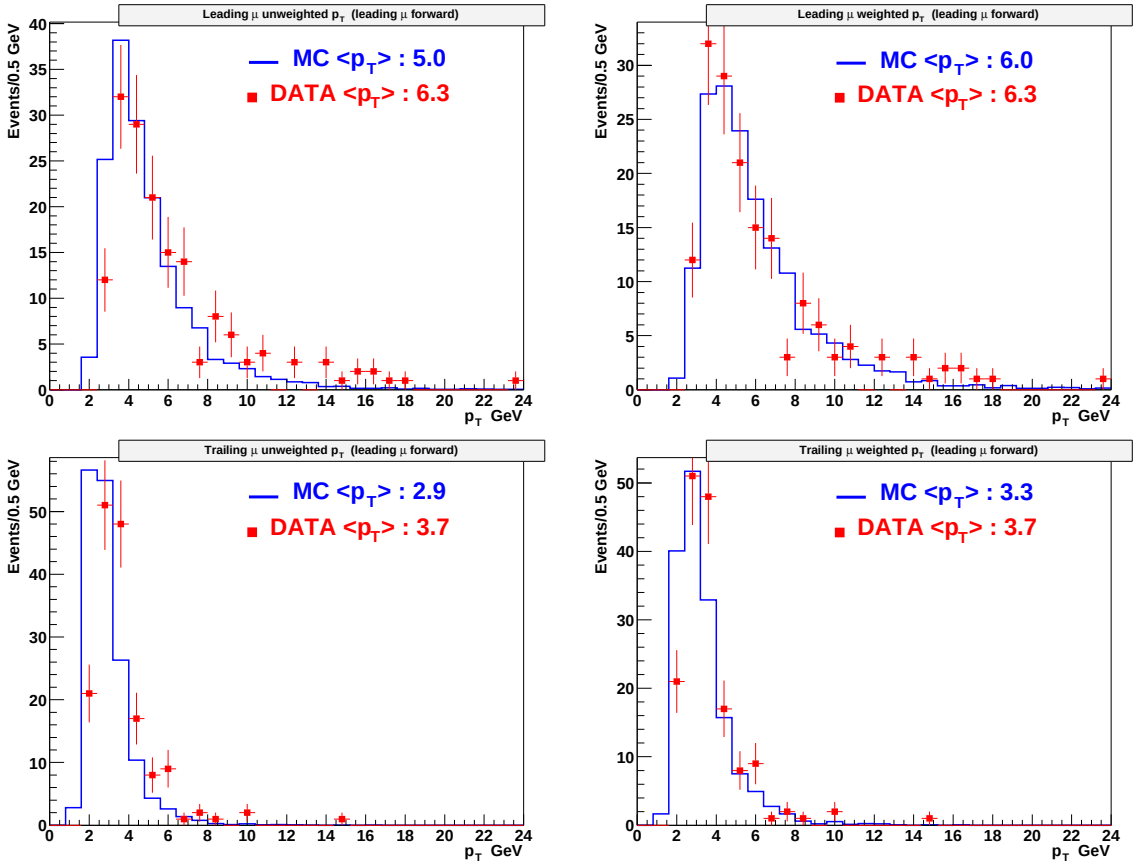

Figure B.4: p_T distribution of the leading muon (top) and the trailing muon (bottom), in the forward rapidity region, in data (points) and MC (solid histogram) uncorrected (left); corrected(right).

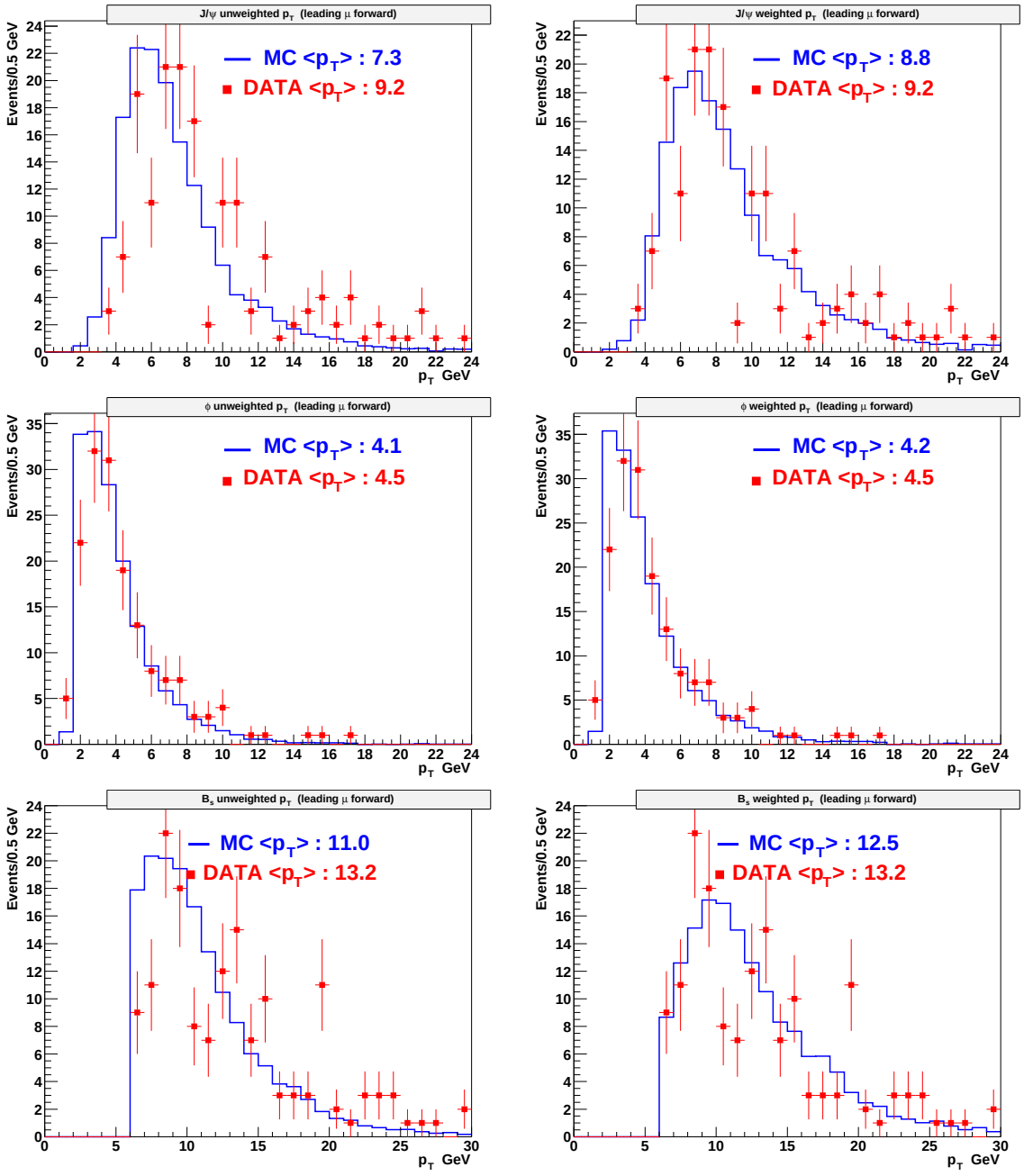

Figure B.5: p_T distribution of J/ψ (top), ϕ (middle), and B_s (bottom), in the forward rapidity region, in data (points) and MC (solid histogram) uncorrected (left); corrected(right)

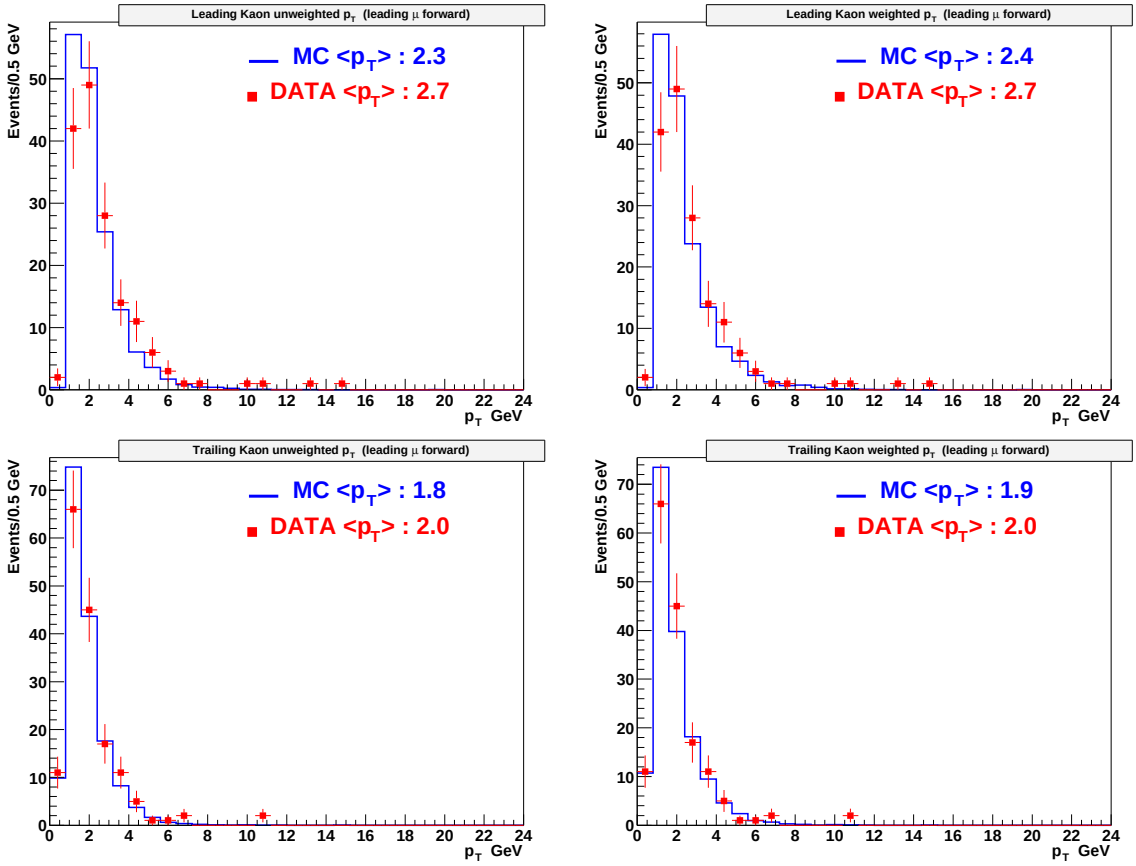

Figure B.6: p_T distribution of the leading kaon (top) and the trailing kaon (bottom), in the forward rapidity region, in data (points) and MC (solid histogram) uncorrected (left); corrected(right).

Appendix C

Comparison of two halfs of the data sample

To test the stability of the analyzed data, we divided data into two sets (Round1→5 and Round6→8), each corresponding approximately half the integrated luminosity (225 pb^{-1}). In the following figures we show the comparison of B_s^0 mass (signal), proper decay length and transversity distributions. We have also compared p_T and pseudorapidity distributions of the leading muon, trailing muon and J/ψ. The Kolmogorov probability is indicated for each pair of distributions. These comparisons establish the compatibility of the two half's of the data sample and hence demonstrate the stability of the data during entire period of running.

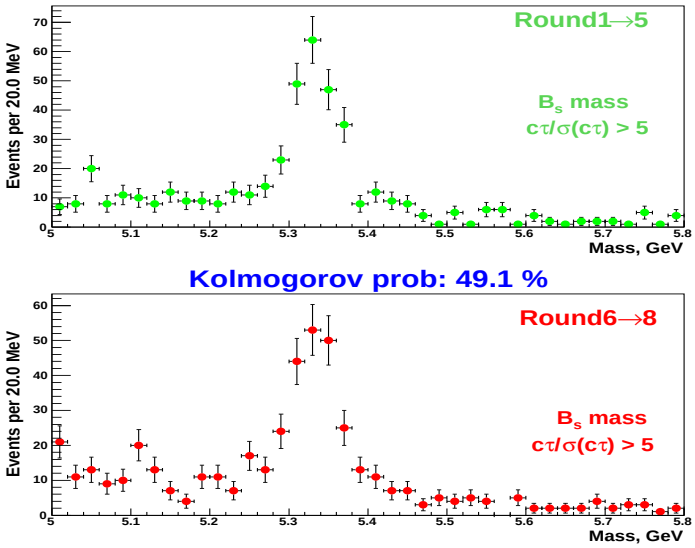

Figure C.1: B_s^0 mass signal for events with $ct/\sigma(ct) > 5$, for Round1→5 (top) and Round6→8 (bottom).

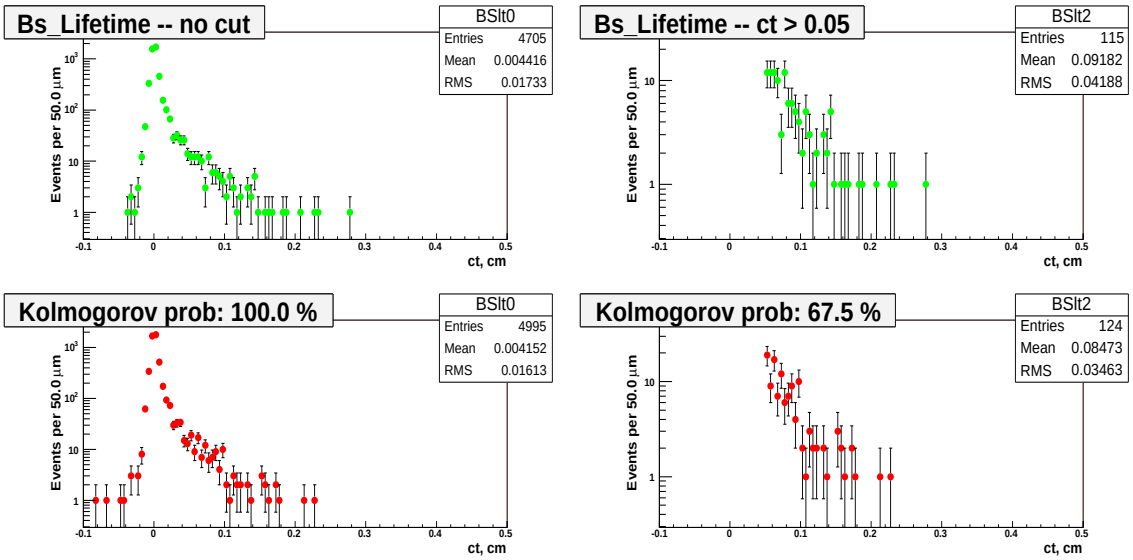

Figure C.2: Proper decay length distribution for all candidates (left) and for events with $ct/\sigma(ct) > 5$ (right), for Round1→5 (top) and Round6→8 (bottom).

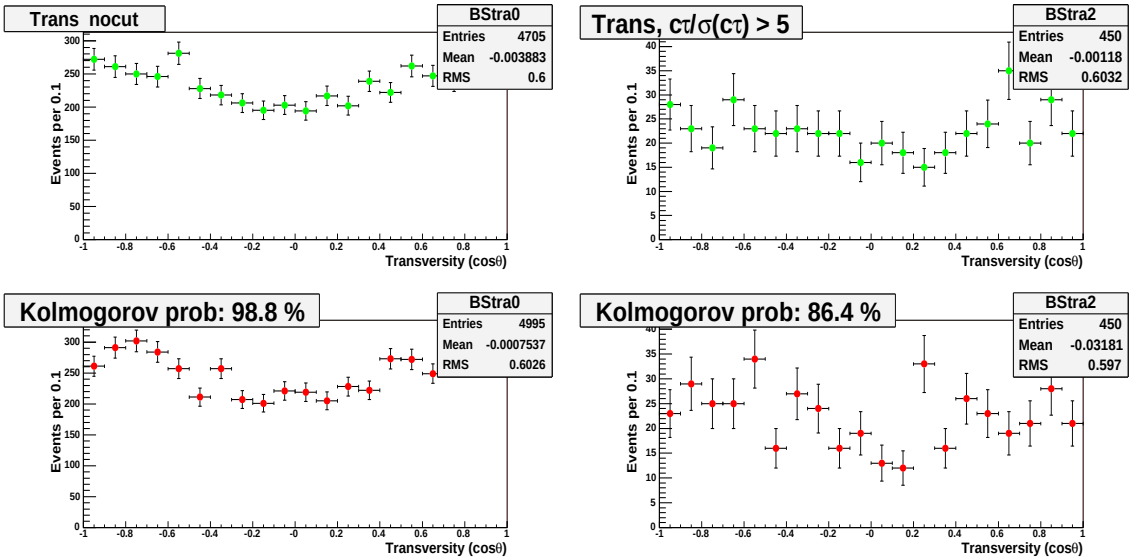

Figure C.3: Transversity distribution for all candidates (left) and for events with $ct/\sigma(ct) > 5$ (right), for Round1→5 (top) and Round6→8 (bottom) .

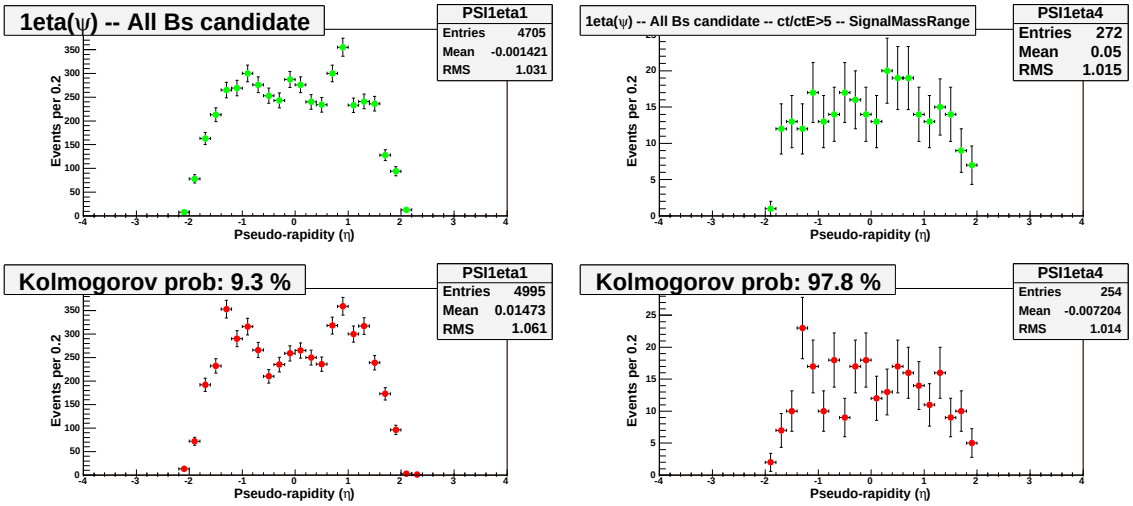

Figure C.4: Pseudorapidity distribution of the leading muon for all candidates (left) and for events with $ct/\sigma(ct) > 5$ and $5.26 < M(B_s < 5.42$ GeV (right), for Round1→5 (top) and Round6→8 (bottom) .

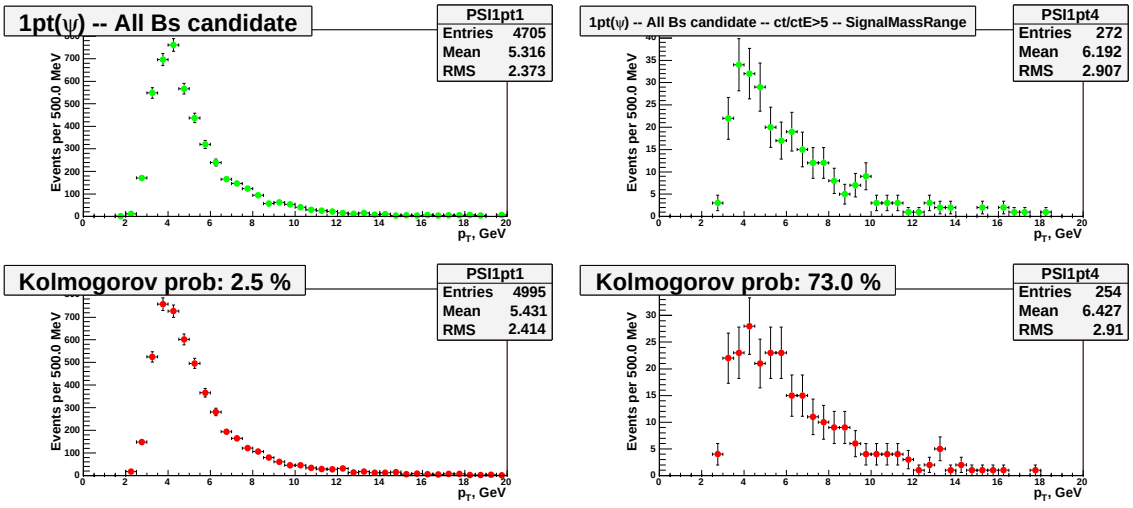

Figure C.5: p_T distribution of the leading muon for all candidates (left) and for events with $ct/\sigma(ct) > 5$ and $5.26 < M(B_s < 5.42$ GeV (right), for Round1→5 (top) and Round6→8 (bottom) .

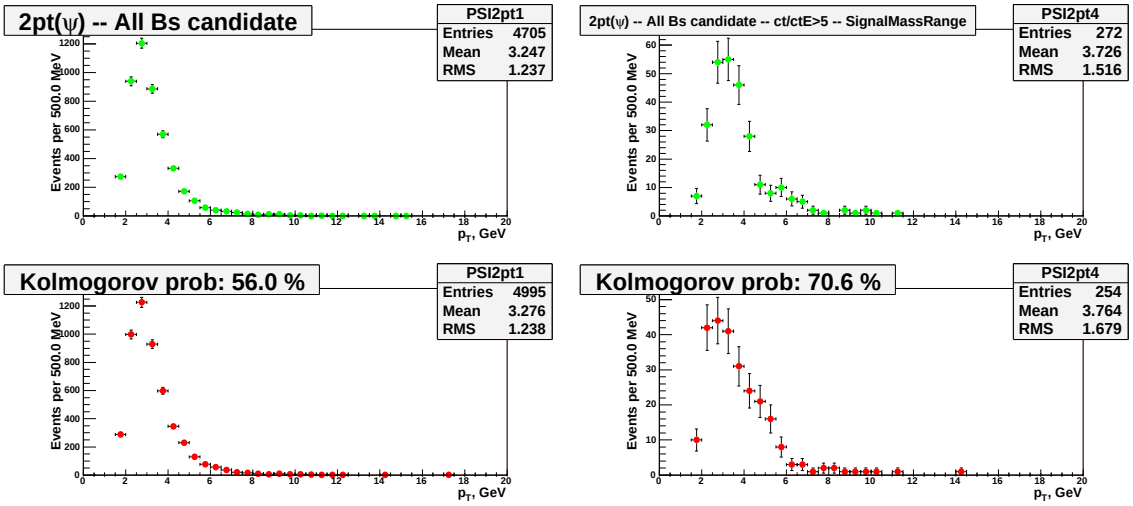

Figure C.6: p_T distribution of the trailing muon for all candidates (left) and for events with $ct/\sigma(ct) > 5$ and $5.26 < M(B_s < 5.42$ GeV (right), for Round1→5 (top) and Round6→8 (bottom) .

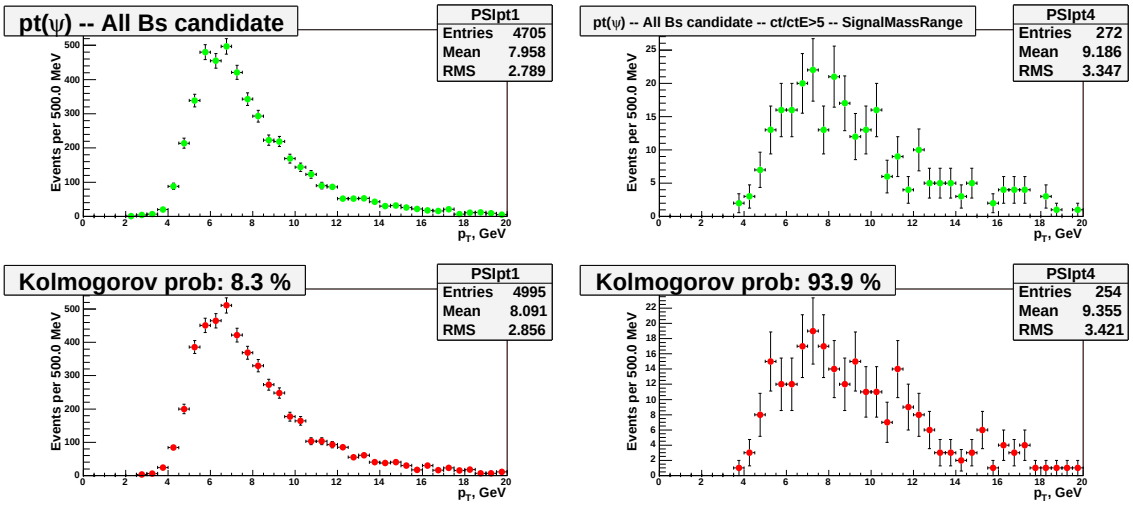

Figure C.7: p_T distribution of the J/ψ candidates for all candidates (left) and for events with $ct/\sigma(ct) > 5$ and $5.26 < M(B_s < 5.42$ GeV (right), for Round1→5 (top) and Round6→8 (bottom) .

References

[1] "B Physics at the Tevatron: Run II and Beyond", Fermilab-Pub-01/197 (2001).

[2] "The CKM Matrix and the Unitarity Triangle", Proceedings of the First Workshop on the CKM Unitarity Triangle, CERN, February 2002.

[3] A. Pich, "The Standard Model of Electroweak Interactions", hep–ph/0502010.

[4] Guido Altarelli, Martin W. Grunewald, "Precision Electroweak Tests of the Standard Model", hep–ph/0404165.

[5] W. Marciano and H. Pagels, Phys. Rep. C **36** (1954) 137.

[6] S. Glashow, Nucl. Phys. **22** (1961) 22; S. Weinberg, Phys. Lett. **12** (1967) 132; A. Salam, "Elementary Particle Physics".

[7] J. Goldstone and S. Weinberg, Phys. Rev. **127** (1962) 965.

[8] P. W. Higgs, Phys. Lett. **12** (1964) 132; Phys. Rev. Lett. **13** (1964) 508.

[9] Stefan W. Bosch, "CKM Overview and Determinations from B Decays", hep–ph/0506153.

[10] L. Wolfenstein, preprint No. NSF-ITP-90-29; Phys. Rev. D **43** (1991) 151.

[11] R. Aleksan, B. Kayser and D. London, Phys. Rev. Lett.73181994.

[12] Heavy Flavor Averaging Group (HFAG), "Averages of b-hadron Properties as of Winter 2005" [hep-ex/0505100].

[13] A. G. Grozin, "Introduction to the Heavy Quark Effective Theory", hep-ph/9908366.

[14] B. Grinstein, "An Introduction to Heavy Mesons", hep-ph/9508227.

[15] The Belle Collaboration: K. Abe, et al, "Improved measurement of $CP-violation$ parameters $sin2\phi_1$ and λ, B meson lifetimes, and $B^0-\overline{B}^0$ mixing parameter ΔM_d", hep-ex/0408111.

[16] Isard Dunietz, "Bs-Bs.bar Mixing, CP Violation and Extraction of CKM Phases from Untagged Bs Data Samples", hep-ph/9501287.

[17] Y. Nir and D. Silverman, Nucl. Phys. **B345**, 301 (1990).

[18] I. Dunietz, R. Fleischer, U. Nierste, "In Pursuit of New Physics with B_s Decays", [hep–ph/0012219]

[19] M.Jacob, G.C. Wick, Annals of Physics 7 (1959), p. 404-428.

[20] A. Dighe, I. Dunietz, H. Lipkin, J. Rosner, Phys. Lett. **B369**, 1996 (p. 144-150).

[21] Polarization of Decays of B Mesons to Two Vector Mesons, Thesis of Stephen Peter Pappas (1999) http://www.hep.caltech.edu/ pappas/Thesis/thesis.html.

[22] A. S. Dighe, I. Dunietz, and R. Fleischer, "Extracting CKM Phases and $B_s-\bar{B}_s$ Mixing Parameters from Angular Distributions of Non-Leptonic B Decays", hep-ph/9804253.

[23] Particle Data Group (see webpage http://pdg.lbl.gov).

[24] P. Ball and R. Fleischer, "An Analysis of B_s Decays in the Left-Right-Symmetric Model with Spontaneous CP", Phys. Lett. **B475**, 111 (2000) [hep–ph/9912319].

[25] Fermi National Accelerator Laboratory (see webpage http://www.fnal.gov/).

[26] V. Shiltsev, Status of Tevatron Collider Run II and Novel Technologies for Luminosity Upgrades, in: Proc. 2004 European Particle Accelerator Conference, Lucern, Switzerland, Vol. 1, 2004, p. 239.

[27] S. Abachi, et al., Nucl. Instrum. Methods Phys. Res. A 338 (1994) 185.

[28] S. D. Holmes, "Design Criteria and Performance Goals for the Fermilab Main Injector", Part. Accel. **58**, 39 (1997); Fermilab-Conf-97/038.

[29] G. P. Jackson, "The Fermilab Recycler Ring Technical Design Report", Fermilab-TM-1991 (1996).

[30] DØ Collaboration, "The Upgraded DØ Detector", physics/0507191.

[31] R. Yarema, et al., Fermilab-TM-1892 (1994, revised 1996).

[32] R. Ruchti, Ann. Rev. Nucl. Part. Sci. 46 (1996) 281.

[33] J. Brzenziak, et al., Fermilab-TM-1886 (1994).

[34] B. Squires, et al., Design of the 2 Tesla Superconducting Solenoid for the Fermilab DØ Detector Upgrade, in: P. Kittel, et al. (Eds.), Advances in Cryogenic Engineering, Plenum Press, New York, New York, 1994, p. 301.

[35] P. Baringer, et al., Nucl. Instrum. Methods Phys. Res. A 469 (2001) 295.

[36] A. M. Patwa, The Forward Preshower System and a Study of the J/ψ Trigger with the DØ Detector, Ph.D. thesis, SUNY at Stony Brook (2002).
URL `www-d0.fnal.gov/results/publications_talks/thesis/patwa/thesis.ps`

[37] Abatron Inc., 33 Center Dr., Gilberts, IL 60136.

[38] The DØ Muon Group: V.M. Abazov, et al, "The Muon System of the Run II DØ Detector", physics/0503151.

[39] B. Acharya, et al., Nucl. Instrum. Methods Phys. Res. A 401 (1997) 45.

[40] J. Butler, et al., Fermilab-FN-629 (1995).

[41] A. Brandt, et al., Fermilab-Pub-97/377 (1997).

[42] U. Amaldi, et al., Phys. Lett. B43 (1973) 231.

[43] T. Edwards, et al., Fermilab-TM-2278-E (2004).

[44] Cisco Systems, Inc.
URL www.cisco.com.

[45] Douglas C. Schmidt, et al.
URL www.cs.wustl.edu/~schmidt/ACE.html.

[46] "MC_Runjob Webpage" see, http://www-clued0.fnal.gov/runjob/.

[47] H. U. Bengtsson and T. Sjostrand, Comp. Phys. Comm. **46**, 43 (1987).

[48] A. Ryd and D. Lange (BarBar and CLEO Collaboration), see the webpage:
http://www.slac.stanford.edu/~lange/EvtGen/.

[49] "Alpgen" see,
http://www-d0.fnal.gov/computing/MonteCarlo/generators/alpgen.html.

[50] "DØ Run 2 Monte Carlo Production" see,
http://www-d0.fnal.gov/computing/mcprod/mcc.html.

[51] "DØ Remote Analysis Coordination Effort Group" see,
http://www-d0.fnal.gov/computing/D0Race/.

[52] F. Paige and S. Protopopescu, Brookhaven National Laboratory Report BNL-37066 (1985) (unpublished).

[53] QQ - the CLEO event generator, see the webpage:
http://www.lns.cornell.edu/public/CLEO/soft/QQ .

[54] "Pythia 6.2: Physics and Manual", hep-ph/0108264.

[55] see http://hepwww.rl.ac.uk/theory/seymour/herwig/hw65_manual.htm.

[56] CERN Application Software and Database Division, "Dector Description and Simulation Tool", see http://wwwasd.web.cern.ch/wwwasd/geant/.

[57] DØ Collaboration, S. Abachi *et al.*, Nucl. Instr. & Meth. paper, in preparation, see http://www-d0.fnal.gov/computing/MonteCarlo/simulation/d0gstar.html.

[58] DØ Collaboration, S. Abachi *et al.*, Nucl. Instr. & Meth. paper, in preparation, see http://www-d0.fnal.gov/computing/MonteCarlo/simulation/d0sim.html.

[59] DØ Collaboration, S. Abachi *et al.*, Nucl. Instr. & Meth. paper, in preparation, see http://www-d0.fnal.gov/computing/algorithms/#intro.

[60] "ThumbNail: a compact data format", Serban Protopopescu, Stephanie Baffioni, Elemer Nagy, see http://www-d0.fnal.gov/d0pub/d0_private/3979/m_tmb_note.ps.

[61] "Central Track Extrapolation Through the DØ Detector", G. Hesketh, see http://www-d0.fnal.gov/d0pub/d0_private/4079/m_extrap.ps.

[62] "Kalman Filter Track Fits and Track Breakpoint Analysis", P.Astier, et al; physics/9912034.

[63] Measurement of the $B^{\pm}$ Lifetime and Top Quark Identification using Secondary Vertex b-tagging, Thesis of Ariel Schwartzman (2004), see http://www-d0.fnal.gov/results/publications_talks/thesis/schwartzman/thesis.pdf.

[64] FNAL database group, "SAM: Sequential data Access via Meta-data", see webpage: http://d0db.fnal.gov/sam/.

[65] Data Files on Disk for B Physics, see http://www-d0.fnal.gov/Run2Physics/ckm/.

[66] Vertex fitting and finding in ROOT, see http://www-d0.fnal.gov/~sch/d0_private/d0root/rootVertex.html.

[67] "Notes on Statistics for Physicists", J. Orear see www.tau.ac.il/~lab3/PARTICLES/stat.pdf.

[68] "ROOT, An Object Oriented Data Analysis Framework" see http://root.cern.ch/.

[69] "MINUIT, Function Minimization and Error Analysis" see `http://wwwasdoc.web.cern.ch/wwwasdoc/minuit/minmain.html`.

[70] D. Acosta et al. (CDF Collaboration), "Measurement of the Lifetime Difference Between B_s Mass Eigenstates", hep-ex/0412057.

[71] K. Anikeev *et al.*, FERMILAB-Pub-01/197, hep-ph/0201071, p. 360.

[72] A. Lenz, "Decay Rate Difference in the Neutral B-System: $\Delta\Gamma$ B_s and $\Delta\Gamma$ B_d", hep-ph/0412007.

[73] DØ Collaboration, V. M. Abazov *et al.*, Phys. Rev. Lett. **94**, 042001 (2005).

[74] R. Barate *et al.* (ALEPH Collaboration), *Phys. Lett.* **486**, 286 (2000).

[75] F. Abe *et al.* (CDF Collaboration), *Phys. Rev.* **57**, 5382 (1998).